Numerical Investigation on CO Emissions in Lean Premixed Combustion

Keita Yunoki

2022

Numerical Investigation on CO Emissions in Lean Premixed Combustion

Keita Yunoki

A thesis submitted to Kyoto University for the degree of Doctor of Philosophy in Engineering

2022

Contents

Acknowledgments

The research described in this thesis was carried out in the Department of Mechanical Engineering and Science at Kyoto University's Graduate School of Engineering.

I would like to express my deep and sincere gratitude to my supervisor, Professor Ryoichi Kurose, for his invaluable guidance, support and encouragements throughout the completion of this work. Because he has given me the opportunity of various new attempts, I could spend a fruitful research period. I am fortunate to meet him through the collaborative research of Mitsubishi Heavy Industries, Ltd..

I would like to thank the review committee of this thesis, Professor Hiroshi Iwai and Professor Kazuyoshi Nakabe for their valuable comments and discussion. I am appreciating their effort and patience to complete the review of the dissertation.

I would like to thank Drs. Teruyuki Okazaki, Kenji Yamamoto, and Masato Handa in my company for allowing me to enter Kyoto University. I would also like to thank Group Manager Kei Inoue for allowing me to attend the doctoral course. I would also like to thank my team members. Thanks to everyone, I was able to concentrate on my research.

I would like to thank Mr. Takayuki Nishiie for his valuable discussion. His extensive knowledge of CFD enabled me to proceed with my research smoothly.

I thank to everyone who belongs to Thermal Science and Engineering Laboratory. In particular, I express my special thanks to Mr. Reo Kai, Mr. Kento Konishi and Mr. Shinpei Inoue for their earnest help.

Lastly, I owe my loving thanks to my parents Hiromi and Katsumi, my grandmothers and grandfathers, and my brother Ryosuke for their caring. I am indebted to my wife Maimi, my daughter Mio and my son Iori for their love, support, and patience during the years of the thesis preparation.

Chapter 1: Introduction

1.1 Background and motivation

In Japan, the target of reducing the rate of greenhouse gas emission, such as carbon dioxide (CO_2) has been set at 80% by 2050. Renewable energy power generation, such as solar power and wind power generation, is expected to increase to achieve this target. According to the long-term energy supply and demand outlook released in July 2015, solar power and wind power generation will account for 7% and 1.7%, respectively, of the total power generation in fiscal year 2030 [1]. However, the output of solar power and wind power generation, which are expected to increase, will be significantly affected by weather. Therefore, it is difficult for solar power and wind power generation to supply stability and environmental compatibility, and the best mix with thermal power generation, which utilizes fossil fuels such as coal, liquefied natural gas and oil, is considered necessary. For thermal power generation, the production of liquefied natural gas (LNG) and shale gas is on track because of the increase in the reserves to production rate. Hence, power supply using gas turbine systems is garnering more attention [2].

Therefore, it is necessary to develop a new thermal power generation system using gas turbines to absorb the fluctuation in the amount of power generated by via renewable energy resources. When the operating load is changed at a high speed, the air–fuel ratio in the combustor changes. This may cause combustion instability. Additionally, it is known that carbon monoxide (CO) emissions, which decreases combustion efficiency, increases not only at low loads [3] but also at high loads because CO is generated by the interference between the flame and cooling air provided to prevent overheating of the combustor walls [4]. Recently, Mitsubishi Heavy Industries, Ltd. developed a gas turbine combustor that can absorb high-speed fluctuation in operating loads with relatively low CO emissions [5]. To develop gas turbine combustors to realize the combination of renewable energy and gas turbine systems, it is important to predict CO emissions and evaluate the CO formation mechanism. Additionally, CO and nitrogen oxides (NOx) emissions standards for gas turbines are becoming stricter every year [6]. Therefore, it is necessary for gas turbine combustors to control CO and NOx emissions simultaneously.

To reduce greenhouse gas emissions, such as CO_2, effectively from such thermal power generations methods, the use of hydrogen (H_2) instead of LNG is promising. To achieve robustness in terms of combustion stability and low environmental loads for a fuel composition of H_2 and LNG, a gas turbine combustor employing a coaxial jet cluster burner, which generates a lean premixed flame, has been developed by Mitsubishi Heavy Industries, Ltd. [7-9]. The coaxial jet cluster burner comprises a plate having a plurality of air holes and a fuel nozzle arranged coaxially with each air hole. This can rapidly mix fuel and air as an oxidizer within a short distance of approximately several tens of millimeters in a hole to form a lean premixed combustion field to reduce NOx emissions [7-9]. However, in this lean premixed combustion field, CO emissions increases and combustion efficiency decreases. Therefore, the reduction of CO emissions is strongly required. Although it is necessary to examine the CO formation mechanism in the combustor for the CO reduction, it is difficult to measure the distribution of temperature, gas composition and velocities in the combustor, because the actual combustor is operated in the high-temperature and high-pressure conditions.

Computational fluid dynamics (CFD) is a powerful tool for investigating the detailed combustion conditions, such as gas composition and temperature in detail. Therefore, it is effective in the development of gas turbine combustors [9-14]. It is expected that by using CFD, the number of prototypes cost, and development period can be reduced. Recently, owing to the remarkable progress in computer technology, turbulent combustion numerical simulations using a large eddy simulation (LES) for lean premixed combustion fields have been reported by many researchers [9, 15-18]. However, most of these researchers did not study the effects of heat loss from cooled walls or interference between cooling air and flames on CO formation.

Therefore, the purpose of this study is to develop numerical simulation methods to precisely predict CO emissions and elucidate the CO formation mechanism in a lean premixed combustion field in combustors with cooled walls and cooling air. The concerns of this study is to analyze the flame propagation phenomena near cooled walls, lean premixed combustion field in a model combustor with a lab-scale jet burner, and combustion field where non-premixed and premixed flames coexist in an actual combustor with a coaxial jet cluster burner. For this concern, direct numerical simulation

(DNS) without any turbulence model and LES with a turbulence model are used. Dynamic models [19, 20] and flamelet approaches [21-25] are employed as turbulence and combustion models for LES. Here, flamelet approaches are employed to eliminate the need for detailed transport calculations of the chemical reaction mechanism and to reduce the calculation costs. Regarding the flamelet approaches, the flamelet generated manifolds (FGM) approach [22] and flamelet progress variable (FPV) approach [23] are chosen for modeling the premixed and non-premixed flames, respectively, and their hybrid approach, i.e., the hybrid turbulent combustion (HTC) approach [24] is also tested. For the FGM approach, to take into account the change in the chemical reaction rate owing to the heat loss through the cooled walls, the non-adiabatic FGM (NA-FGM) approach [25] is mainly used. This treatment is expected to increase the prediction accuracy of CO emissions, because CO is highly dependent on temperature change. The flamelet libraries needed for flamelet approaches are generated by solving the one-dimensional (1D) flame transport equations by considering the detailed chemical reaction mechanism beforehand [21-25].

1.2 Thesis outline

Figure 1.1 shows the structure of this thesis. Chapter 1, the present chapter, is an introduction, which describes the research background, motivation, and outline of this study. When classified according to the numerical approach used, that used in Chapter 2 is the one- and two-dimensional (1D and 2D) DNSs with the detailed reaction mechanism approach or the NA-FGM approach. The approach used in Chapter 3 is LES with FGM or NA-FGM approaches, whereas that used in Chapter 4 is LES with the HTC approach.

In Chapter 2, the premixed combustion fields close to the cooled walls with flame propagation for the 1D and 2D fields are discussed. For the 1D combustion fields, detailed chemical reaction calculations are used to evaluate the effect of heat loss from the cooling walls on the rates of CO formation and consumption. For the 2D combustion fields, the accuracy of CO formation and consumption rates by the NA-FGM approach is validated by comparing the calculation results of the detailed chemical reaction mechanism approach with those of the NA-FGM approach.

In Chapter 3, the CH_4-air super lean premixed combustion fields in a model combustor under pressurized conditions with heat loss through the cooled walls are discussed. The validity of predicting the CO emissions by the LESs using the FGM or NA-FGM approaches based on a comparison with the experimental results is examined. Moreover, the effects of heat loss and equivalence ratios on the CO emissions are investigated in detail.

In Chapter 4, the complicated combustion fields in an actual combustor with a coaxial jet cluster burner in which non-premixed and premixed flames coexist are discussed. We validate the LESs with the HTC approach by comparing the results with the measured gas temperature and gas concentration distributions obtained by a coaxial jet cluster burner test rig under atmospheric pressure and analyze the CO formation mechanism, which is an important performance factor for gas turbine combustors.

In Chapter 5, the conclusions are summarized for the entire thesis.

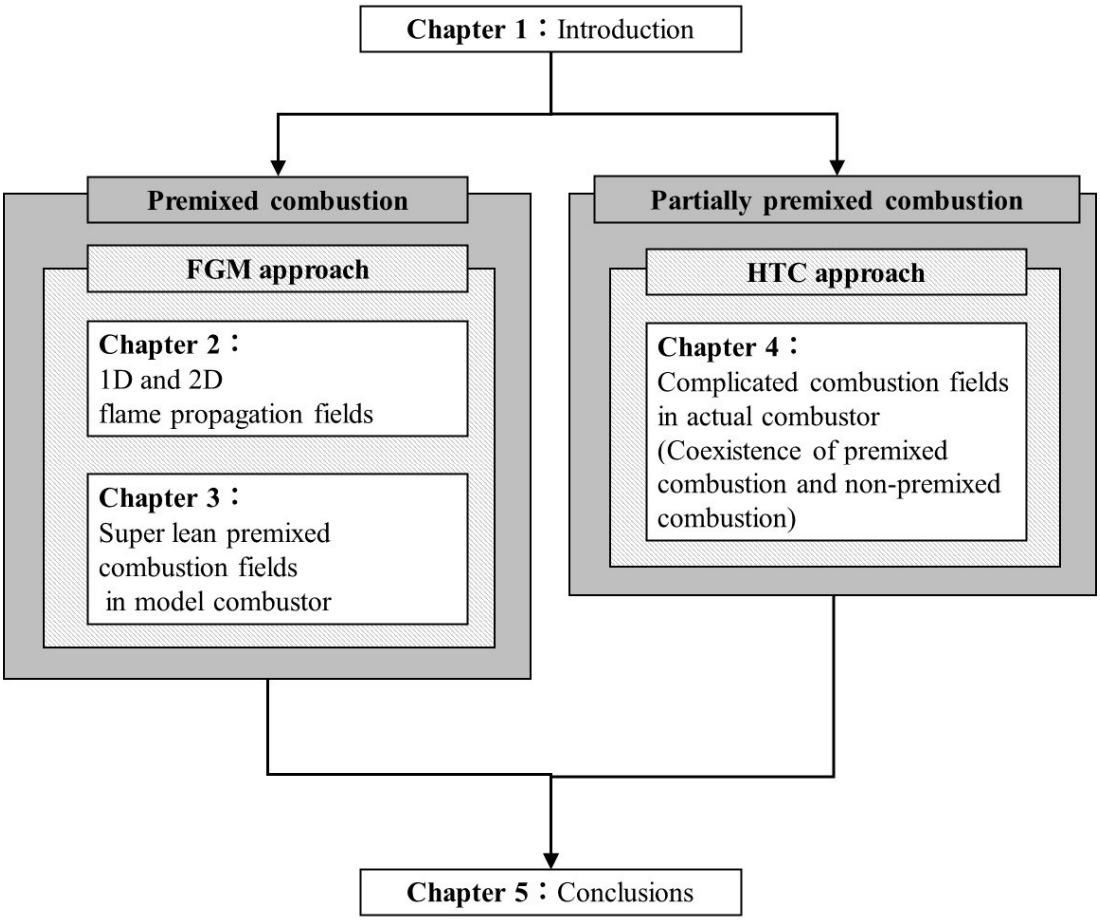

Figure 1.1 Structure of this thesis

References

[1] Ministry of Economy, Trade and Industry, “Long term prospect of electricity outlook”, (2015).
[Online]. Available:
https://www.enecho.meti.go.jp/committee/council/basic_policy_subcommittee/mitoshi/pdf/report_01.pdf.

[2] Ministry of Economy, Trade and Industry, “Annual report on energy”, (2018).
[Online]. Available:
https://www.enecho.meti.go.jp/about/whitepaper/2018html/2-2-2.html

[3] T., Koganezawa, K., Miura, T., Saitou, K., Abe, and H., Inoue, “Full Scale Testing of a Cluster Nozzle Burner for the Advanced Humid Air Turbine” Proceedings of ASME

Turbo Expo 2007, GT2007-27737 (2007).

[4] G., Cabot, D., Vauchelles, B., Taupin, and A., Boukhalfa, “Experimental study of lean premixed turbulent combustion in a scale gas turbine chamber” Experimental Thermal and Fluid Science, 28 pp.683–690 (2004).

[5] New Energy and Industrial Technology Development Organization, “News press”, (2018).
[Online]. Available: https://www.nedo.go.jp/news/press/AA5_100996.html

[6] Mitsubishi Research Institute, “Survey report on trends in overseas environmental regulations and environmental industries”, (2011).
[Online]. Available:
https://dl.ndl.go.jp/view/download/digidepo_11241468_po_E001477.pdf?contentNo=1&alternativeNo=

[7] T., Asai, S., Dodo, H., Koizumi, H., Takahashi, S., Yoshida, and H., Inoue, “Effects of Multiple-injection-burner Configurations on Combustion Characteristics for Dry Low-NOx Combustion of Hydrogen-rich Fuels” Proceedings of ASME Turbo Expo 2011, GT2011-45295 (2011).

[8] K., Miura, S., Dodo, K., Koyama, and S., Yoshida, “Development of Elemental Technologies of Gas Turbine Combustor for LNG” Proceedings of GTSJ, GTSJ A-18 (2009).

[9] K., Yunoki, T., Murota, T, Asai, and T., Okazaki, “Large eddy simulation of a multiple-injection dry low NOx combustor for hydrogen-rich syngas fuel at high pressure”, Proceedings of ASME Turbo EXPO 2016, GT2016-58119 (2016).

[10] T., Murota, and M., Ohtsuka, “Large-Eddy Simulations of Combustion Oscillation in Premixed Combustor”, Proceedings of ASME Turbo EXPO 1999, ASME 99-GT-274 (1999).

[11] S., Menon, and W.-H., Jou, “Large-Eddy Simulations of Combustion Instability in an Axisymmetric Ramjet Combustor”, Combustion, Science and Technology, 75, pp.53-72 (1991).

[12] S., Menon, and S., Pannala, “Subgrid Two-Phase Mixing and Combustion Modeling”, Proceedings of ASME Turbo EXPO 1998 (1998).

[13] R., Rydén, L.-E., Eriksson, and S., Olovsson, “Large Eddy Simulation of Bluff Body

Stabilized Turbulent Premixed Flames", Proceedings of ASME Turbo EXPO 1993 (1993).

[14] T., Murota, and K., Yamamoto, "Hybrid Turbulent Combustion Model for All of Diffusion, Premixed and Partially Premixed Flames", 47th Symposium (Japanese) on Combustion. (2009).

[15] S., Tachibana, K., Saito, T., Yamamoto, M., Makida, T., Kitano, and R., Kurose, "Experimental and numerical investigation of thermo-acoustic instability in a liquid-fuel aero-engine combustor at elevated pressure: Validity of large-eddy simulation of spray combustion", Combustion and Flame 162 2621-2637 (2015).

[16] T., Nishiie, M., Makida, N., Nakamura, and R., Kurose, "Large-eddy simulation of turbulent spray combustion field of full annular combustor for aircraft engine", Proceedings of International Gas Turbine Congress 2015 (2015).

[17] K., Hirano, Y., Nonaka, Y., Kinoshita, M., Muto, and R., Kurose, "Large-eddy simulation of turbulent combustion in multi combustors for l30a gas turbine engine", Proceedings of the ASME Turbo EXPO 2015 (2015).

[18] H., Moriai, R., Kurose, H., Watanabe, Y., Yano, F., Akamatsu, and S., Komori, "Large-eddy simulation of turbulent spray combustion in a subscale aircraft jet engine combustor - predictions of no and soot concentrations", Journal of Engineering for Gas Turbines and Power 135 (2013).

[19] R., Kai, K., Takenaka, and R., Kurose, "Validity of non-adiabatic FGM approach for numerical simulation of flame propagation in the vicinity of the wall", Proceedings of International Gas Turbine Congress 2019 (2019).

[20] K., Yunoki, R., Kai, S., Inoue, and R., Kurose, "Numerical Simulation of CO Concentration on Flame Propagation in the Vicinity of the Wall -Validity of Non-Adiabatic FGM Approach-", International Journal of Gas Turbine, Propulsion and Power Systems, 11 (2020).

[21] N., Peters, "Laminar flamelet concept in turbulent combustion", Proceedings of Combustion Institute, 21; 21:1231-1250 (1986).

[22] J. A. v., Oijen, and L. P. H. d., Goey, "Modeling of pre-mixed laminar flames using flamelet-generated manifolds", Combustion Science and Technology 161, 113-137 (2000).

[23] H., Pitsch and M., Ihme, "An Unsteady /Flamelet Progress Variable method for LES of Nonpremixed Turbulent Combustion", AIAA Paper 2004-557 (2004).

[24] T., Murota, and K., Yamamoto, “Hybrid Turbulent Combustion Model for All of Diffusion, Premixed and Partially Premixed Flames”, 47th Symposium (Japanese) on Combustion. (2009).

[25] B., Fiorina, R., Baron, O., Gicquel, D., Thevenin, S., Carpentier, and N., Darabiha, “Modeling non-adiabatic partially premixed flames using flame-prolongation of ILDM”, Combustion Theory and Modeling, Vol. 7, pp. 449-470 (2003).

Chapter 2: One- and two-dimensional (1D and 2D) numerical simulations of premixed flame in the vicinity of a cooled wall

2.1 Introduction

Owing to the recent increase in renewable energy power generations, the urgent establishment of new technology for industrial gas turbines capable of rapid load fluctuation is foreseen. Hence, a main challenge is to operate gas turbine combustors using liquefied natural gas (LNG) while maintaining low carbon monoxide (CO) and nitrogen oxide (NOx) emissions under a wide load range, i.e., from full load to low partial load. Such low-emission combustors have been studied by several researchers worldwide, especially in terms of NOx emissions in lean premixed combustion [1-3], whereas little research has been performed on CO emissions [4, 5]. Cabot et al. [4] performed an experimental study on a lean premixed turbulent combustion in a scale gas turbine chamber and confirmed the relationship between the cooling air and CO emissions. Mann et al. [5] conducted simultaneous measurements of temperature and CO concentration and investigated the transient interactions between the flame and wall.

Because CO emissions are known to be susceptible to temperature variation [6, 7], the elucidation of the CO formation and consumption mechanisms in the vicinity of the cooled wall in a gas turbine combustor is crucial for achieving lower CO emissions at low partial loads. However, the measurement of CO is very difficult owing to the quenching of the CO oxidation reaction not only under high-pressure gas turbine conditions but also under atmospheric pressure conditions. Moreover, for computational fluid dynamics (CFD) employing the turbulent combustion approaches [8-14], such as the G equation model [15, 16] and the flamelet generated manifolds (FGM) approach [17], it is difficult to predict the CO emissions with heat loss in the vicinity of the cooled wall with high accuracy. This is because CO is a kind of minor species whose concentration is less than 1000 ppm, and the formation and consumption rates are strongly affected by the various combustion conditions.

For the turbulent combustion approach, the heat loss must be considered to clarify the combustion phenomenon in the vicinity of the wall. Therefore, researchers have attempted to develop efficient non-adiabatic flamelet generated manifolds (NA-FGM) approaches [18–20]. Fiorina et al. [18] and Proch and Kempf [19] suggested a method to consider the heat loss effect and verified the applicability of the proposed method to a steady burner flame. Fiorina et al. [20] performed three-dimensional large eddy simulations (LESs) and demonstrated an improvement in the accuracy of the flame height. Pantangi et al. [21] also performed three-dimensional LESs and compared the steady CO distribution between the experimental results and calculation results. Honzawa et al. [22] applied the FGM approach by considering the heat loss effect to a premixed flame and showed the validity of the proposed approach for predicting CO emissions with equivalence ratios of 0.84 – 1.31. Additionally, other researchers have shown the availability of flamelet approaches for predicting CO emissions [23, 24]. Some studies have employed flamelet approaches; however, most of these studies focused on the steady turbulent flame. The applicability of the NA-FGM approach for predicting CO formation and consumption for the lean premixed flame near the cooled wall has not been investigated properly.

Therefore, the purpose of this study is to perform a one-dimensional numerical simulations employing a detailed reaction mechanism approach, and two-dimensional numerical simulations employing a detailed reaction mechanism approach or the NA-FGM approach, to analyze the CH_4–air premixed flame near the cooled wall, and to investigate the effects of the equivalence ratio (0.5, 0.7, and 1.0), pressure (0.1 and 2.0 MPa), and wall temperature (300 and 750 K) on CO emissions in detail. The results of this study are useful for the development of industrial gas turbine combustors because methane is the main component of LNG.

2.2 Numerical methods

2.2.1 Detailed reaction mechanism approach

The non-filtered and non-averaged conservation equations for mass, momentum, enthalpy, mass fractions of chemical species, and the state equation for an ideal gas are solved in the gas phase as follows:

$$\frac{\partial \rho}{\partial t} + \nabla \cdot (\rho u) = 0 \tag{1}$$

$$\frac{\partial \rho u}{\partial t} + \nabla \cdot (\rho u u) = -\nabla P + \nabla \cdot \tau \tag{2}$$

$$\begin{aligned} \frac{\partial \rho h}{\partial t} + \nabla \cdot (\rho h u) &= \frac{D\mathrm{P}}{Dt} + \tau : \nabla u \\ &+ \nabla \cdot \left[\rho D_h \left(\nabla h - \sum_k (h_k \nabla Y_k) \right) - \rho \sum_k (h_k Y_k V_k) \right] \end{aligned} \tag{3}$$

$$\frac{\partial \rho Y_k}{\partial t} + \nabla \cdot (\rho Y_k u) = -\nabla \cdot (\rho Y_k V_k) + \rho \dot{\omega}_k \tag{4}$$

$$P = \rho R T \sum_k \frac{Y_k}{W_k} \tag{5}$$

where ρ is the density, u is the velocity vector, P is the pressure, τ is the shear stress tensor, h is the enthalpy, h_k is the enthalpy of chemical species k, D_h is the thermal diffusivity, Y_k is the mass fraction of chemical species k, V_k is the diffusion velocity of chemical species k, $\dot{\omega}_k$ is the chemical reaction rate of chemical species k, T is the temperature, R is the gas constant and W_k is the molecular weight of chemical species k.

The thermodynamic properties considering temperature dependence (h_k and isobaric specific heat C_p) and transport coefficient (viscosity μ and thermal diffusivity D_h), are calculated from the databases of Kee et al. [25]. The detailed reaction mechanism applied is GRI-Mech 3.0 considering 53 species and 325 reaction steps [26], and the $\dot{\omega}_k$ is obtained by solving Arrhenius formulation of each reaction in this reaction mechanism. The results of this approach, which sets very fine grids and doesn't include any mathematical models, can be considered as exact reference without comparing with the experimental results.

2.2.2 Flamelet generated manifolds (FGM) approach

The FGM approach is one of the combustion approaches and the reaction is considered by using pre-tabulated database, which is called flamelet library, instead of solving Arrhenius formulation directly. The governing equations for the FGM approach can be written as:

$$\frac{\partial \rho}{\partial t} + \nabla \cdot (\rho u) = 0 \tag{6}$$

$$\frac{\partial \rho u}{\partial t} + \nabla \cdot (\rho u u) = -\nabla P + \nabla \cdot \tau \tag{7}$$

$$\frac{\partial \rho h}{\partial t} + \nabla \cdot (\rho h u) = \frac{DP}{Dt} + \nabla \cdot (\rho D_h \nabla h) + \tau : \nabla u \tag{8}$$

$$\frac{\partial \rho Z}{\partial t} + \nabla \cdot (\rho Z u) = \nabla \cdot (\rho D_Z \nabla Z) \tag{9}$$

$$\frac{\partial \rho C}{\partial t} + \nabla \cdot (\rho C u) = \nabla \cdot (\rho D_C \nabla C) + \rho \dot{\omega}_C \tag{10}$$

where $\dot{\omega}_C$ is the generation rate of progress variable, C is the progress variable defined as the mass fraction of burned gas (H_2O, H_2, CO_2 and CO), D_γ is the diffusion coefficient $\left(D_\gamma = \lambda/\rho C_p\right)$, λ is the thermal conductivity, and C_p is the isobaric specific heat.

This approach requires a pre-tabulated database called a flamelet library, which is generated by calculations involving a one-dimensional laminar premixed flame under various conditions, using the following governing equations:

$$\frac{\partial(\rho u)}{\partial x} = 0 \tag{11}$$

$$\rho u \frac{\partial Y_k}{\partial x} = -\frac{\partial j_k}{\partial x} + \dot{m}_k \tag{12}$$

$$\rho u C_p \frac{\partial T}{\partial x} = \frac{\partial}{\partial x}\left(\lambda \frac{dT}{dx}\right) - \sum_k C_p\, j_k \frac{\partial T}{\partial x} - \sum_k h_k\, \dot{m}_k \tag{13}$$

Thus, this library is obtained through detailed elementary reaction calculations with the FlameMaster code [27] in combination with GRI-Mech 3.0 [26]. This database provides all scalar quantities as functions of the mixture fraction Z and the progress variable C. Figure 2.1 shows an example of a flamelet library for the FGM approach.

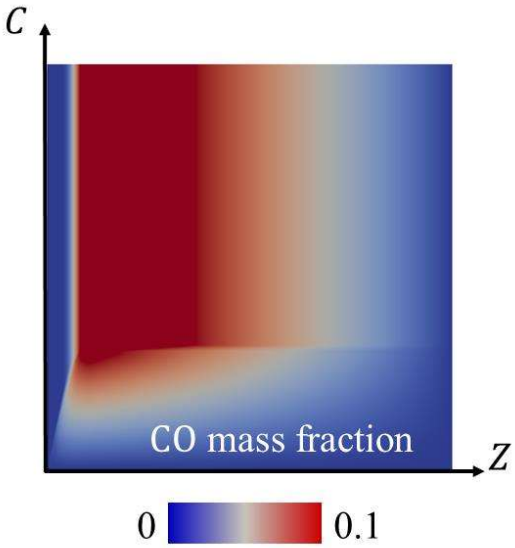

Figure 2.1 Example of flamelet library for FGM approach.

2.2.3 Non-adiabatic flamelet generated manifolds (NA-FGM) approach

In general, the flamelet library for the FGM approach does not consider heat loss. However, the premixed flame in a gas turbine combustor is generated in the vicinity of the cooling wall. Therefore, the NA-FGM approach [18-20] is employed to include the effect of the heat loss.

The flamelet library, with the effect of the heat loss considered, is calculated using eqs. (11), (12) and the following equation (14).

$$\rho u C_p \frac{\partial T}{\partial x} = \frac{\partial}{\partial x}\left(\lambda \frac{\partial T}{\partial x}\right) - \sum_k C_p j_k \frac{\partial T}{\partial x} - \sum_k h_k \dot{m}_k + \dot{q}_{loss} \tag{14}$$

$$\dot{q}_{loss} = \alpha \sum_k h_k \dot{m}_k \tag{15}$$

where $\dot{q}_{loss}$ is the source term of heat loss and α is the adjustment parameter. In this study, adjustment parameters from 0.0 to 0.4 were calculated at every 0.05 increment. The adjustment parameter is based on the maximum value of predicted heat loss [28-30].

The maximum value of predicted heat loss was calculated by the enthalpy of burnt gas at a given wall temperature. Figure 2.2 shows an example of the flamelet library for the NA-FGM approach. The flamelet library for the NA-FGM approach is defined by three variables (mixture fraction Z, progress variable C, and the difference of enthalpy Δh) in order to output some physical quantities. The difference of enthalpy Δh can be written as:

$$\Delta h = h_0 - h \tag{16}$$

where h_0 is the enthalpy without heat loss, and h is the enthalpy obtained by eq. (8).

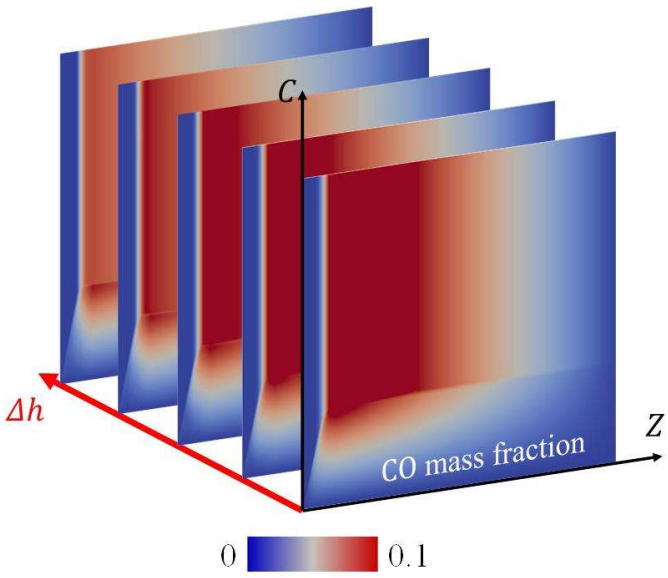

Figure 2.2 Example of flamelet library for NA-FGM approach.

2.2.4 Calculation setup

In this study, one-dimensional and two-dimensional premixed flame propagation near the cooled wall was adopted as the verification object. Figure 2.3 shows the diagram of the premixed turbulent combustion regimes [31]. According to this diagram, a combustion configuration of the gas turbine combustor mainly includes corrugated flamelets, a thin reaction zones regime, and a broken reaction zones regime. This two-

dimensional object can set the thin reaction zones regime as the calculation condition for each equivalence ratio, pressure, and wall temperature.

The schematic diagram of the calculation domain for one-dimensional numerical simulation is shown in Figure 2.4. The length of domain x is changed by equivalence ratio φ or initial pressure P. The computational grid in each case is a staggered grid, with a difference range Δx, as shown in Figure 2.4. At the outlet boundary (right side), the Dirichlet boundary condition is imposed for pressure, with free outflow conditions being imposed for the other variables. The wall boundary (left side) is set as the cooled wall. A no-slip condition was used for the wall. Table 2.1 lists the calculation conditions. Pressure P at 0.1 MPa and 2.0 MPa, premixed fuel temperature T_f at 750 K (premixed fuel) are set as the initial conditions. Wall temperature T_{wall} is set at 300 K and 750 K constant, while the fuel composition is CH_4 only. The equivalence ratio φ is changed as a parameter (to three values) to evaluate the sensitivity of the CO concentration. In this study, the lower equivalence ratio is focused on because the low emissions combustors are operated by lean premixed combustion. For ignition in case of the one-dimensional numerical simulation, 2000 K for stoichiometric ratio was set at right end of the calculation domain.

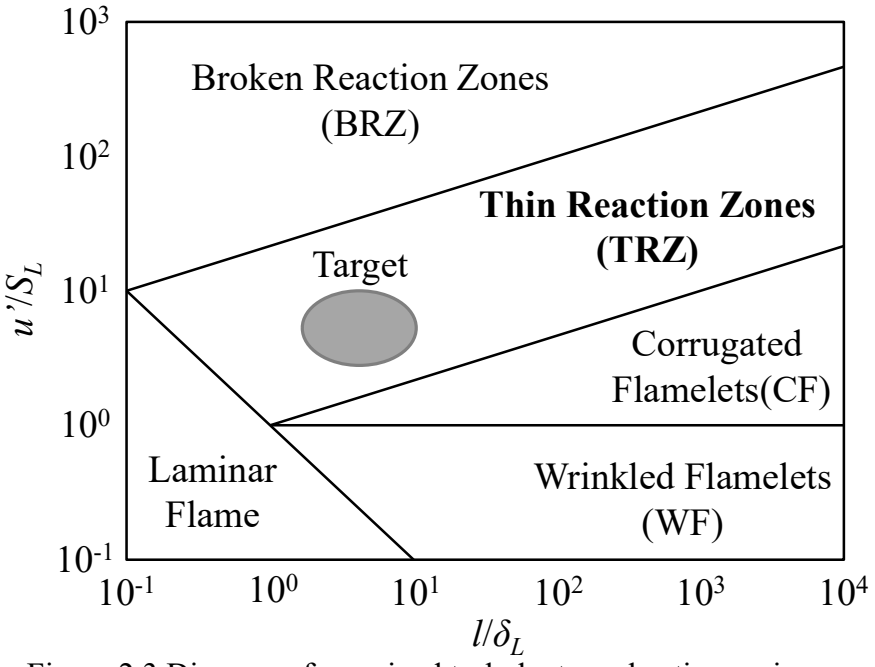

Figure 2.3 Diagram of premixed turbulent combustion regimes.

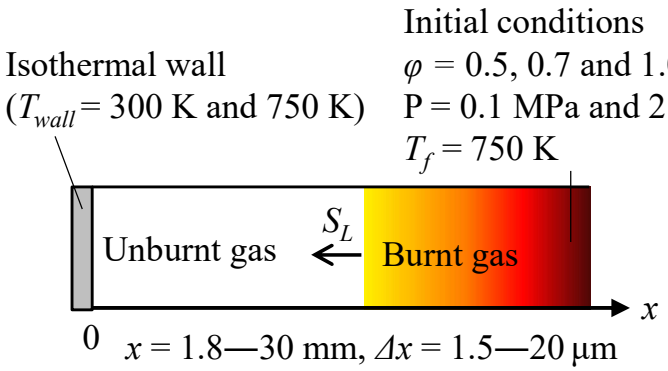

Figure 2.4 Schematic diagram of calculation domain for one-dimensional numerical simulation.

Table 2.1 Calculation conditions for one-dimensional numerical simulation.

Case	P (MPa)	φ (-)	T_f (K)	T_{wall} (K)	x (mm)	Δx (mm)
1-1	0.1	0.5	750	Adiabatic	10	1.00×10^{-2}
1-2	0.1	0.5	750	750	10	1.00×10^{-2}
1-3	0.1	0.5	750	750	30	2.00×10^{-2}
1-4	0.1	0.7	750	750	18	1.50×10^{-2}
1-5	0.1	1.0	750	750	15	1.50×10^{-2}
1-6	2.0	0.5	750	750	6.0	4.00×10^{-3}
1-7	2.0	0.7	750	750	2.5	1.50×10^{-3}
1-8	2.0	1.0	750	750	1.8	1.50×10^{-3}
1-9	0.1	0.5	750	300	30	2.00×10^{-2}
1-10	2.0	0.5	750	300	6.0	4.00×10^{-3}

The schematic diagram of the calculation domain for the two-dimensional numerical simulation is shown in Figure 2.5. The calculation domain is two-dimensional rectangular (40.96 mm × 5.12 mm) [29, 30]. The x coordinate indicates a direction parallel to the length of the wall and the y coordinate indicates a direction vertical to the length. The computational grids are staggered grids, with the uniform grid size Δ of 20 μm. 2048

grid points are set in the x direction and 256 grid points are set in the y direction. The boundary in the x direction is the outlet. At the outlet boundary, the Dirichlet boundary condition was imposed for pressure, with free outflow conditions being imposed for the other variables. The boundary in the y direction is set at the cooled wall. A no-slip condition was used for all walls. Table 2.2 lists the calculation conditions. Pressure P of 0.1 MPa and premixed fuel temperature T_f of 750 K (premixed fuel) are set as the initial conditions. Wall temperatures T_{wall} are set at constants of 300 K and 750 K. The fuel composition is CH_4, identical to the one-dimensional numerical simulation's fuel composition. Wall temperature T_{wall} is changed as a parameter to evaluate the sensitivity of the CO concentration. For ignition, in the case of the two-dimensional numerical simulation employing a detailed reaction mechanism approach, flame temperatures for each equivalence ratio were set at the central position of the calculation domain, whereas in the case using the NA-FGM approach, progress variables for ignition C_{ign} in the flamelet library were set at the central position of the calculation domain.

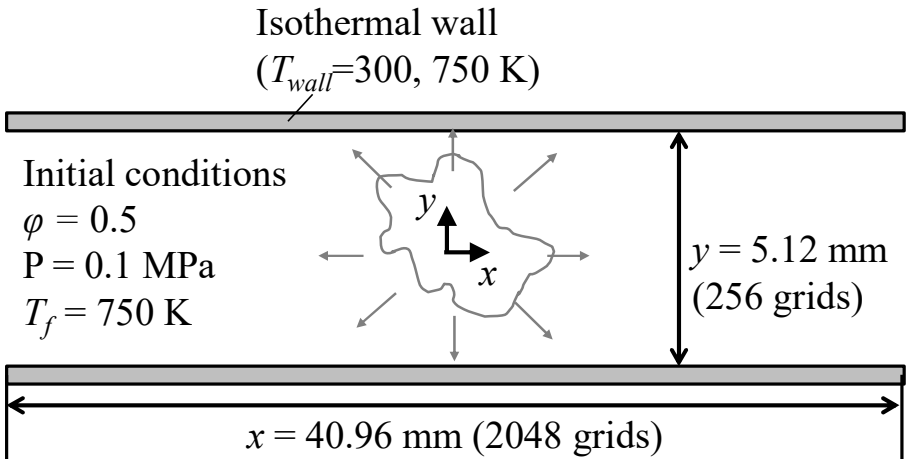

Figure 2.5 Schematic diagram of calculation domain for two-dimensional numerical simulation.

Table 2.2 Calculation conditions for two-dimensional numerical simulation.

Case	P (MPa)	φ (-)	T_f (K)	T_{wall} (K)	x (mm)	y (mm)	Δ (mm)
2-1	0.1	0.5	750	750	40.96	5.12	2.00×10^{-2}
2-2	0.1	0.5	750	300	40.96	5.12	2.00×10^{-2}

Artificial turbulence field obtained from the inverse Fourier transform of an energy spectrum is applied as the initial turbulence condition [32]. Turbulence variance intensity, laminar burning velocity, laminar flame thickness, and integral length scale are selected for the thin reaction zones regime for equivalence ration of 0.5 and pressure of 0.1 MPa.

The laminar burning velocity S_L is calculated by the detailed elementary reaction calculation with the FlameMaster code [27]. The laminar flame thickness δ_L is calculated by equation (17). These parameters are calculated at both 300 K and 750 K. The Lewis number is assumed as 1 in the case of the NA-FGM approach. The Reynolds number is approximately 50 for each equivalence ratio.

$$\delta_L = \frac{\lambda}{\rho C_p S_L} \tag{17}$$

In this study, the in-house code FK^3 is used [28-30, 33–37]. The spatial derivative of the convective term in the momentum equation is approximated with a fourth-order central difference scheme, and a weighted essentially non-oscillatory (WENO) scheme [38] is used to evaluate the scalar gradients. A third-order accurate strong-stability preserving (SSP) Runge–Kutta method [39] is adopted in time integration. Combustion behavior of one-dimensional numerical simulations is calculated for 10 ms using a CRAY: XE6 at the ACCMS, Kyoto University, with 256 cores and 6 h (the detailed reaction mechanism approach) of wall clock time. On the other hand, combustion behavior of two-dimensional numerical simulations is calculated for 100 ms using a CRAY: XE6 at the ACCMS, Kyoto University, with 1024 cores and 62.5 h (the detailed reaction mechanism approach) or 8.5 h (the NA-FGM approach) of wall clock time. Courant–Friedrichs–Lewy (CFL) number of all cases is less than 0.06, in order to guarantee time accuracy. Time-step is 0.02 μs (one-dimensional numerical simulations) and 0.1 μs (two-dimensional numerical simulations).

2.3 Results and discussions

2.3.1 One-dimensional (1D) numerical simulation

2.3.1.1 Effects of heat loss on CO emissions

Figure 2.6 shows the comparisons of instantaneous x-direction profiles of gas temperature, enthalpy and CO mass fraction in the vicinity of the wall at x = 0–2.0 mm between adiabatic (Case 1-1) and non-adiabatic (Case 1-2) cases. The vertical axis denotes temperature, enthalpy, and CO mass fraction, and the horizontal axis the x-direction distance. Flame propagates from the right side in Figure 2.4 to the left side (cooled wall) after ignition. Here, the initial time (0 ms) is defined when the peak of the CO mass fraction reaches the cooled wall. In this study, the CO mass fraction at x = 0 mm is investigated to evaluate the behavior of CO formation near the cooled wall.

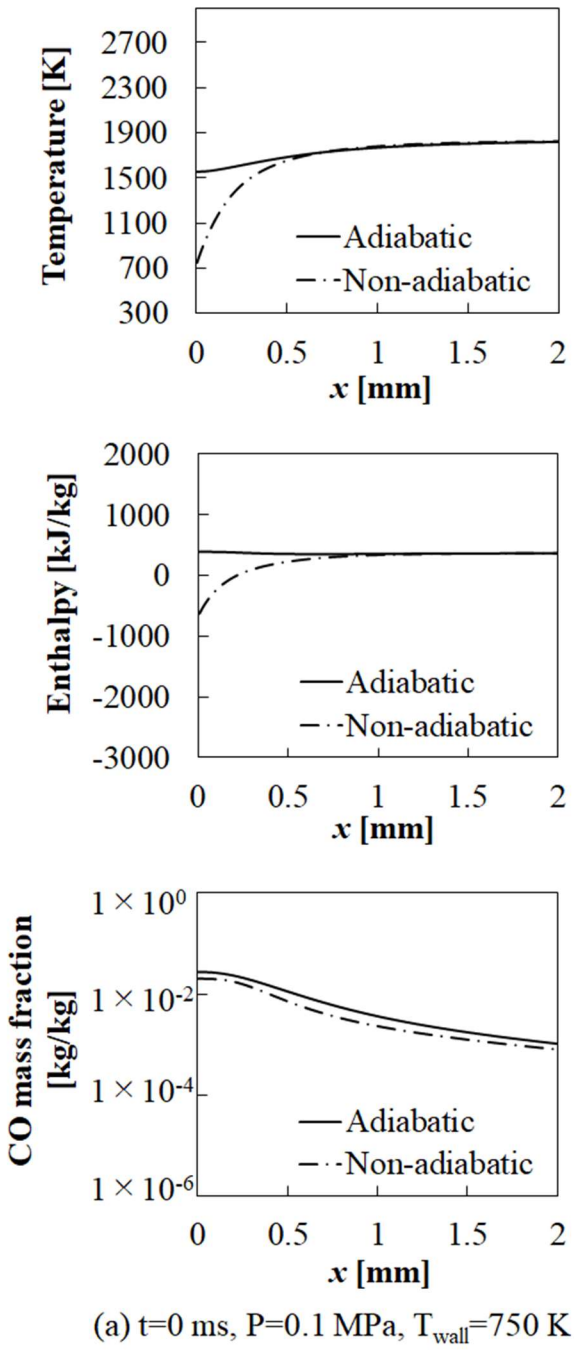

(a) t=0 ms, P=0.1 MPa, T_{wall}=750 K

Figure 2.6 Comparisons of instantaneous *x*-direction profiles of gas temperature, enthalpy, and CO mass fraction in the vicinity of the wall at *x* = 0–2.0 mm between adiabatic (Case 1-1) and non-adiabatic (Case 1-2) cases (Continues).

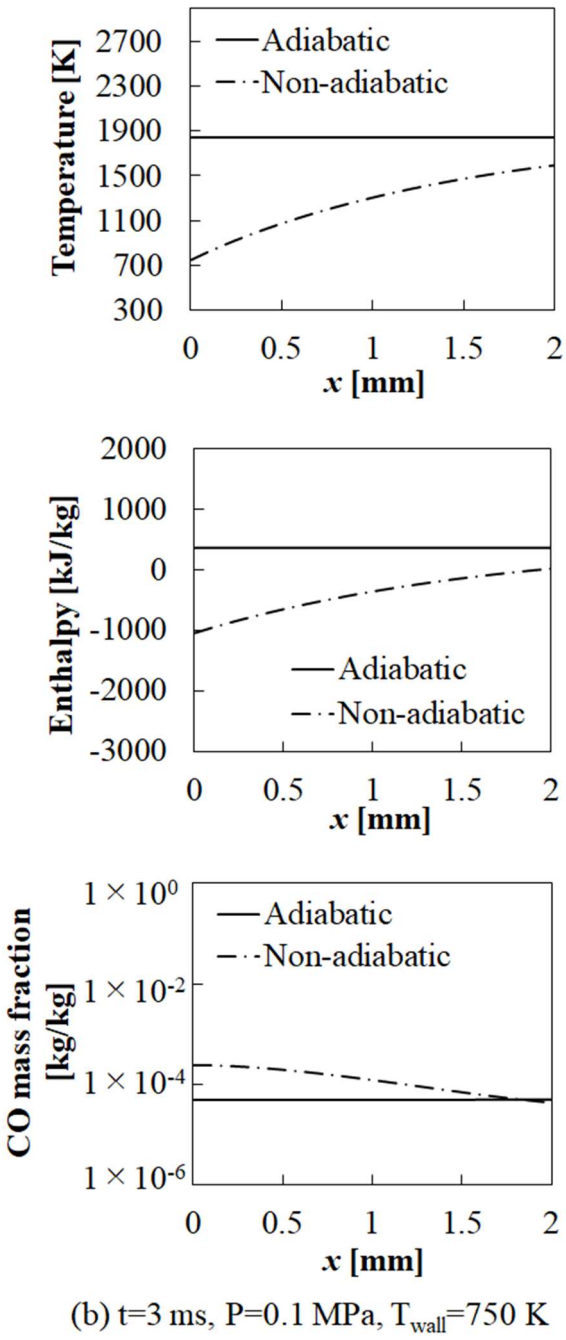

(b) t=3 ms, P=0.1 MPa, T_{wall}=750 K

Figure 2.6 Comparisons of instantaneous *x*-direction profiles of gas temperature, enthalpy and CO mass fraction in the vicinity of the wall at x = 0–2.0 mm between adiabatic (Case 1-1) and non-adiabatic (Case 1-2) cases (Continued).

For Case 1-2 (non-adiabatic wall), the temperature decreases after the flame reaches the cooled wall, with heat loss as shown in the enthalpy profiles. On the other hand, the CO mass fraction for the non-adiabatic case agrees well with that for the adiabatic case. This calculation result means that the combustion configuration before the flame reaches the cooled wall is not strongly dependent on the heat loss near the cooled wall. However, at 3 ms later, the CO mass fraction near the cooled wall shows a tendency to decrease rapidly under adiabatic condition. In contrast, under non-adiabatic condition, the CO can remain at the cooled wall (0 mm). This is because the lowering of the CO oxidation reaction rate occurs by decreasing temperature due to the heat loss at the cooled wall. These results clarify that the effect of heat loss plays an important role in predicting the CO mass fraction.

2.3.1.2 Effects of equivalence ratio and pressure on CO emissions

Figure 2.7 shows the comparisons of instantaneous x-direction profiles of gas temperature, enthalpy and the CO mass fraction in the vicinity of the wall at x = 0 – 2.0 mm under atmospheric pressure conditions with different equivalence ratios (Cases 1-3, 4 and 5). The vertical axis is for temperature, enthalpy and CO mass fraction, and the horizontal axis is for distance in the x-direction. These conditions consider the heat loss on the cooled wall. The time t is defined as 0 ms when the peak of the CO mass fraction has reached the cooled wall because the flame propagation rate is modified by changing the equivalence ratio.

It is observed that the change in the equivalence ratio strongly affects the flame temperature. Conversely, the difference in enthalpy is small compared with that of the flame temperature at 0 ms. However, at 6 ms later, temperature and enthalpy make a significant difference compared with the results at 0 ms. The CO mass fraction of a lower equivalence ratio (φ = 0.5) near the cooled wall at 0 ms is approximately 40 % lower than that at a higher equivalence ratio (φ = 1.0). At 6 ms later, the CO mass fraction under lower equivalence ratios (φ = 0.5 and 0.7) decreases rapidly (by more than 98 %). In contrast, the CO consumption rate for φ = 1.0 is lower (reducing by 93 %) than that under lower equivalence ratios because the CO oxidation reaction is not activated by decreasing enthalpy at the cooled wall.

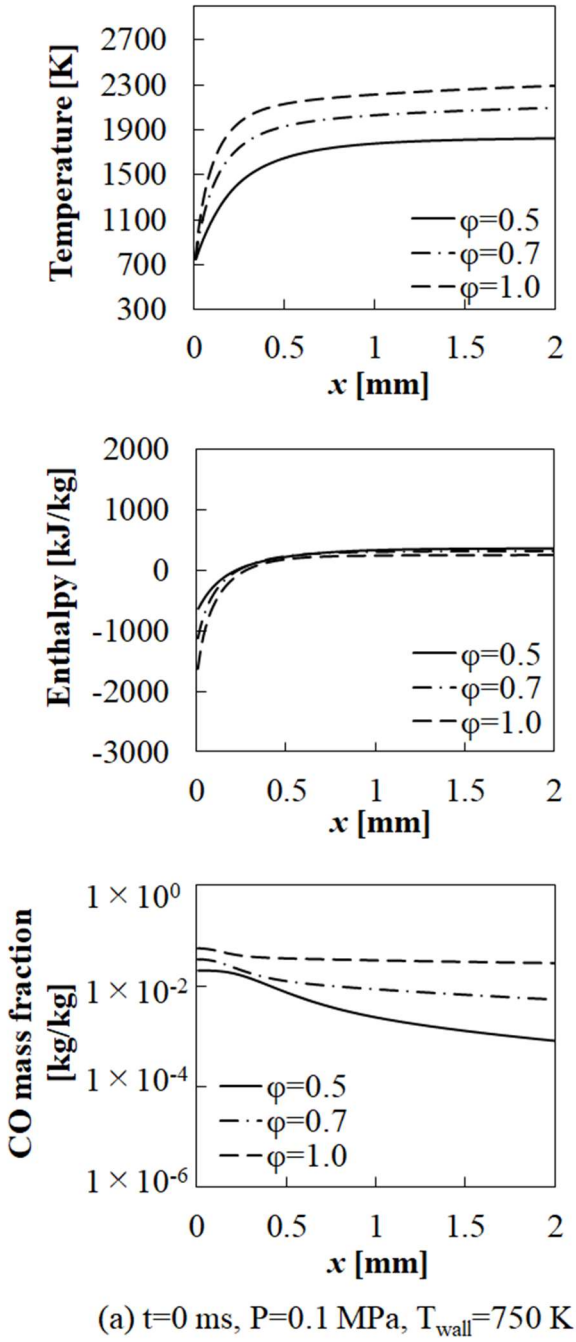

(a) t=0 ms, P=0.1 MPa, T_{wall}=750 K

Figure 2.7 Comparisons of instantaneous *x*-direction profiles of gas temperature, enthalpy and CO mass fraction in the vicinity of the wall at *x* = 0–2.0 mm under atmospheric pressure conditions with different equivalence ratios (Cases 1-3, 4 and 5) (Continues).

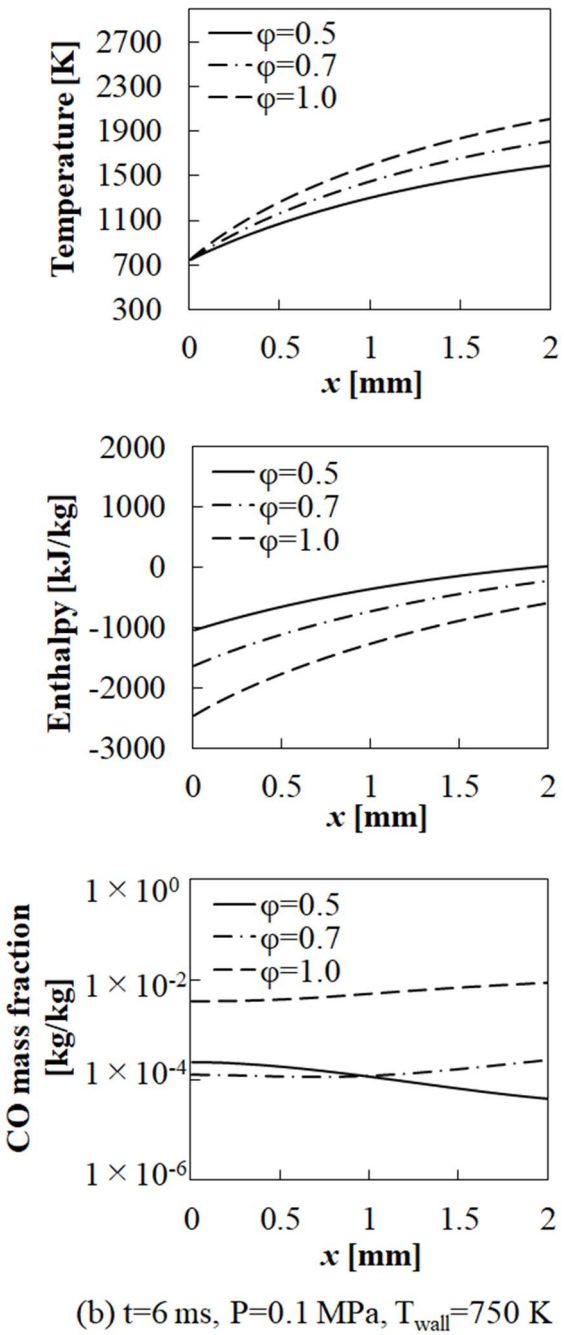

(b) t=6 ms, P=0.1 MPa, T_{wall}=750 K

Figure 2.7 Comparisons of instantaneous *x*-direction profiles of gas temperature, enthalpy and CO mass fraction in the vicinity of the wall at *x* = 0–2.0 mm under atmospheric pressure conditions with different equivalence ratios (Cases 1-3, 4 and 5) (Continued).

Figure 2.8 shows the comparisons of the instantaneous *x*-direction profiles of gas temperature, enthalpy and CO mass fraction in the vicinity of the wall at *x* = 0 – 2.0 mm

under high pressure conditions with different equivalence ratios (Cases 1-6, 7 and 8). The vertical axis denotes temperature, enthalpy and the CO mass fraction, and the horizontal axis is for distance in the *x*-direction.

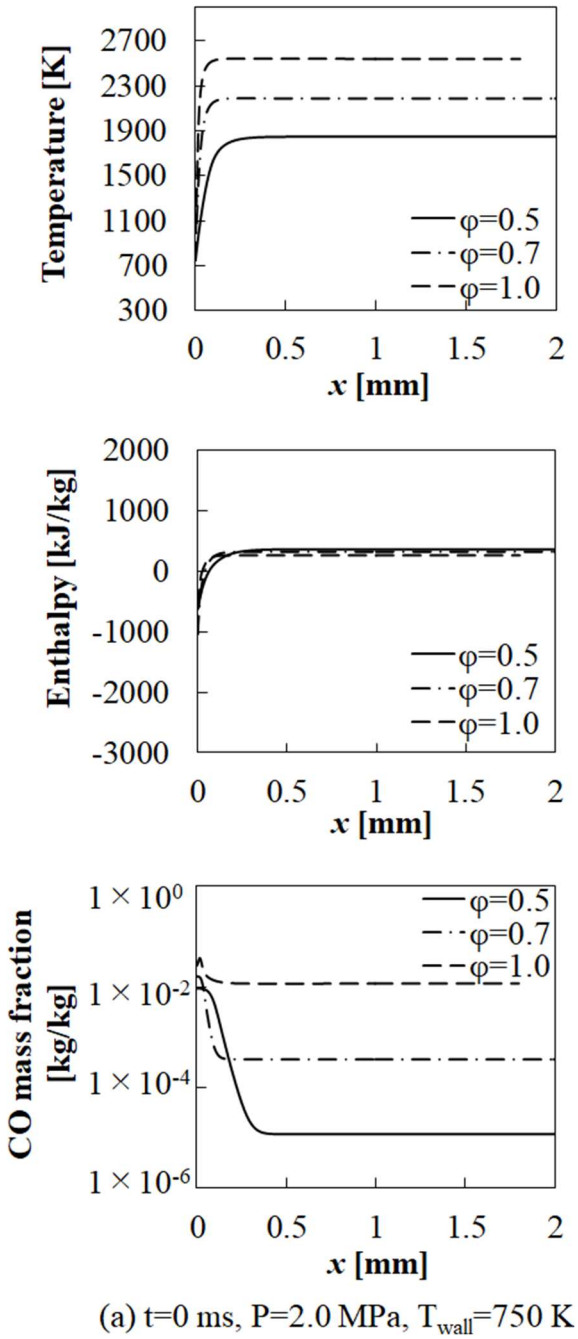

(a) t=0 ms, P=2.0 MPa, T_{wall}=750 K

Figure 2.8 Comparisons of instantaneous *x*-direction profiles of gas temperature, enthalpy and CO mass fraction in the vicinity of the wall at x = 0–2.0 mm under high pressure conditions with different equivalence ratios (Cases 1-6, 7 and 8) (Continues).

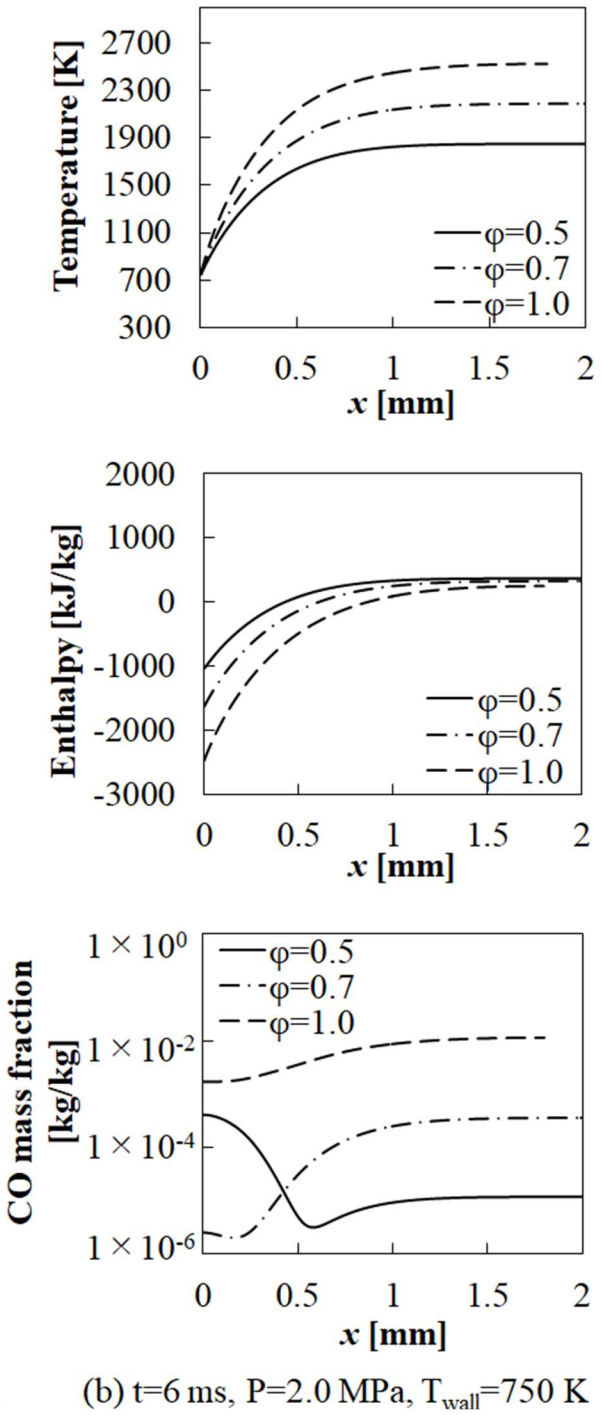

(b) t=6 ms, P=2.0 MPa, T_{wall}=750 K

Figure 2.8 Comparisons of instantaneous *x*-direction profiles of gas temperature, enthalpy and CO mass fraction in the vicinity of the wall at *x* = 0–2.0 mm under high pressure conditions with different equivalence ratios (Cases 1-6, 7 and 8) (Continued).

The width of the CO formation area under high pressure becomes narrower because the flame thickness under high pressure is smaller for lean premixed combustion than that when it is under atmospheric pressure. The CO mass fraction near the cooled wall under high pressure is lower than that under atmospheric pressure conditions for each equivalence ratio. This is because, in spite of the same equivalence ratio, the flame propagation speed becomes low at high pressure, so that the CO formation/consumption rate under high pressure is suppressed compared with that under atmospheric pressure. As shown in Figure 2.8 at 6 ms later, CO consumption ratio under high pressure condition was 95.58 % (φ = 0.5), 99.98 % (φ = 0.7) and 94.96 % (φ = 1.0). The CO consumption rate of lower equivalence ratio is higher than that of a stoichiometric ratio. However, the CO consumption rate at each equivalence ratio is adequately fast, and this trend is also observed under atmospheric pressure conditions. These results suggest that the investigation under atmospheric pressure is effective for understanding the trend of CO formation/consumption behavior; nevertheless it is necessary to evaluate CO formation/consumption under high pressure in order to predict the CO mass fraction quantitatively under actual conditions of the gas turbine combustor.

2.3.1.2 Effect of wall temperature on CO emissions

Figure 2.9 shows the comparisons of the instantaneous x-direction profiles of gas temperature and enthalpy in the vicinity of the wall at x = 0 – 2.0 mm at -3 ms between the wall temperatures T_{wall} of 750 K (Case 1-3) and 300 K (Case 1-9). The vertical axis denotes temperature and enthalpy, and the horizontal axis is for distance in the x-direction.

There is a difference of enthalpy near the cooled wall as shown in figure 2.9, and the enthalpy for Case 1-9 is much lower than Case 1-3 due to the low wall temperature. Due to this difference of enthalpy, the flame temperature, at greater than x = 3 mm for Case 1-9 is lower than Case 1-3. The unburnt gas region at 750 K is larger than that at 300 K. It is considered that flame is not supposed to propagate to the cooled wall due to significant heat loss.

Figures 2.10 and 2.11 show the comparisons of the instantaneous x-direction profiles of temperature, enthalpy and the CO mass fraction in the vicinity of the wall at x = 0 – 2.0 mm between the wall temperatures T_{wall} of 750 K (Case 1-3) and 300 K (Case 1-9) under atmospheric and high pressure conditions, respectively. The vertical axis

denotes temperature, enthalpy and CO mass fraction, and the horizontal axis is for distance in the *x*-direction.

The maximum CO concentration under T_{wall}= 750 K at 0 ms is slightly higher than that under T_{wall}= 300 K. The amount of CO formation varies depending on the heat loss near the cooled wall. However, the CO consumption rate under T_{wall}= 750 K is high in spite of high CO concentration at the initial conditions. The CO mass fraction at 6 ms later under T_{wall}= 750 K is reduced by 98.88 % under atmospheric condition and by 95.58 % under high pressure condition. In contrast, the CO mass fraction at 6 ms later under T_{wall}= 300 K is reduced by 47.20 % under atmospheric condition and by 25.72 % under high pressure condition. The CO consumption rate depends on the wall temperature, and this tendency of CO consumption rate is not changed by variance of the equivalence ratio.

These calculation results suggest that excessive cooling of the wall may increase the CO mass fraction discharged from the combustor.

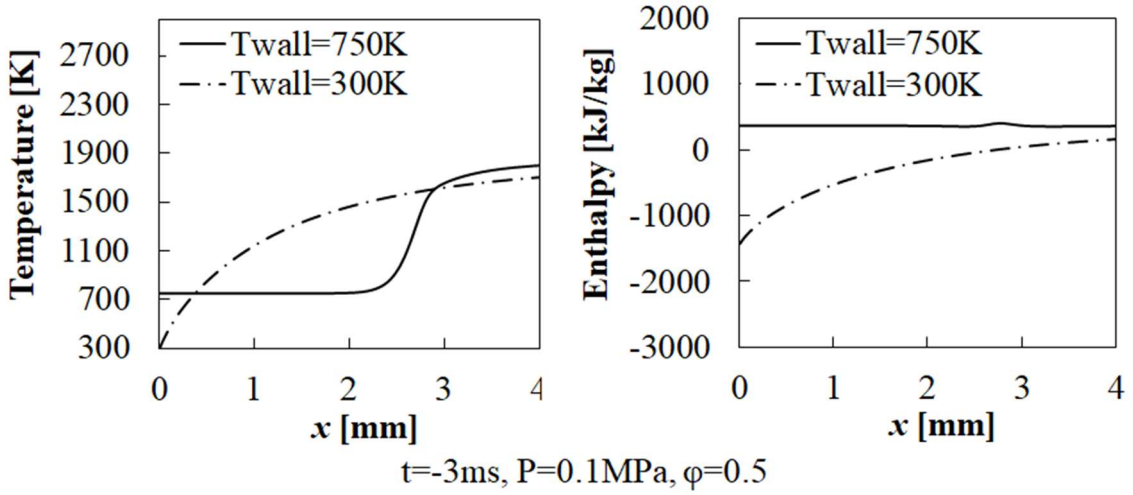

Figure 2.9 Comparisons of instantaneous *x*-direction profiles of gas temperature and enthalpy in the vicinity of the wall at *x* = 0–2.0 mm at -3 ms between the wall temperatures T_{wall} of 750 K (Case 1-3) and 300 K (Case 1-9).

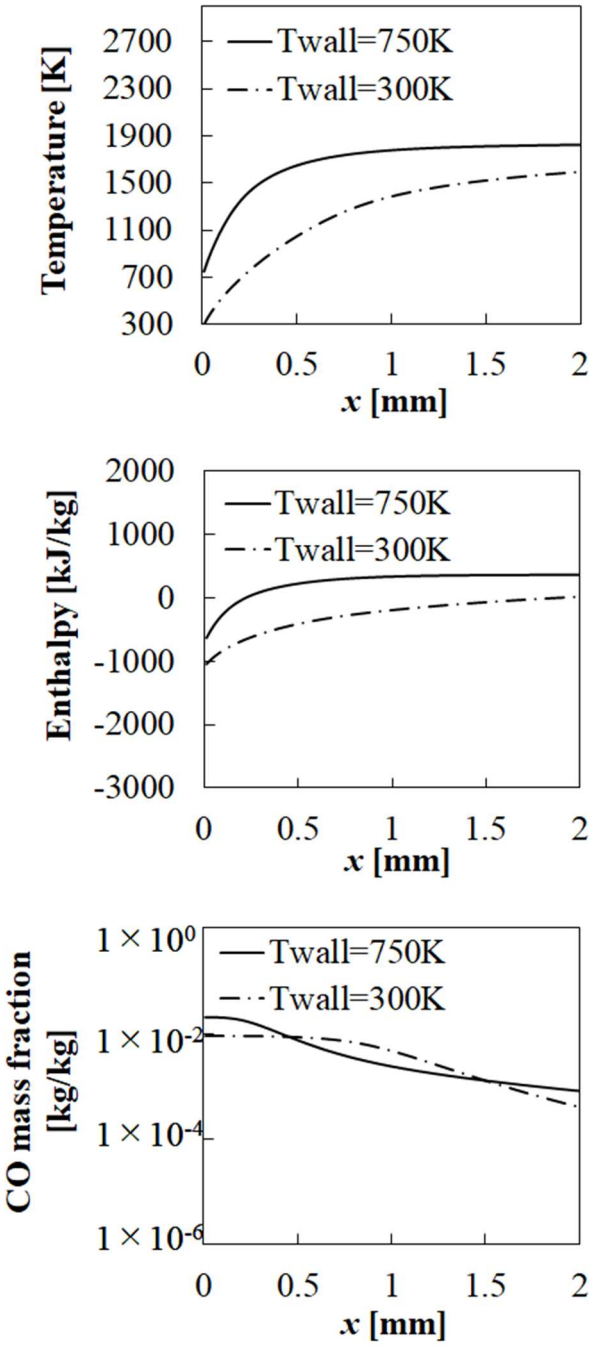

(a) t=0 ms, P=0.1 MPa, φ=0.5

Figure 2.10 Comparisons of instantaneous *x*-direction profiles of temperature, enthalpy and CO mass fraction in the vicinity of the wall at x = 0–2.0 mm under atmospheric pressure conditions between the wall temperatures T_{wall} of 750 K (Case 1-3) and 300 K (Case 1-9) (Continues).

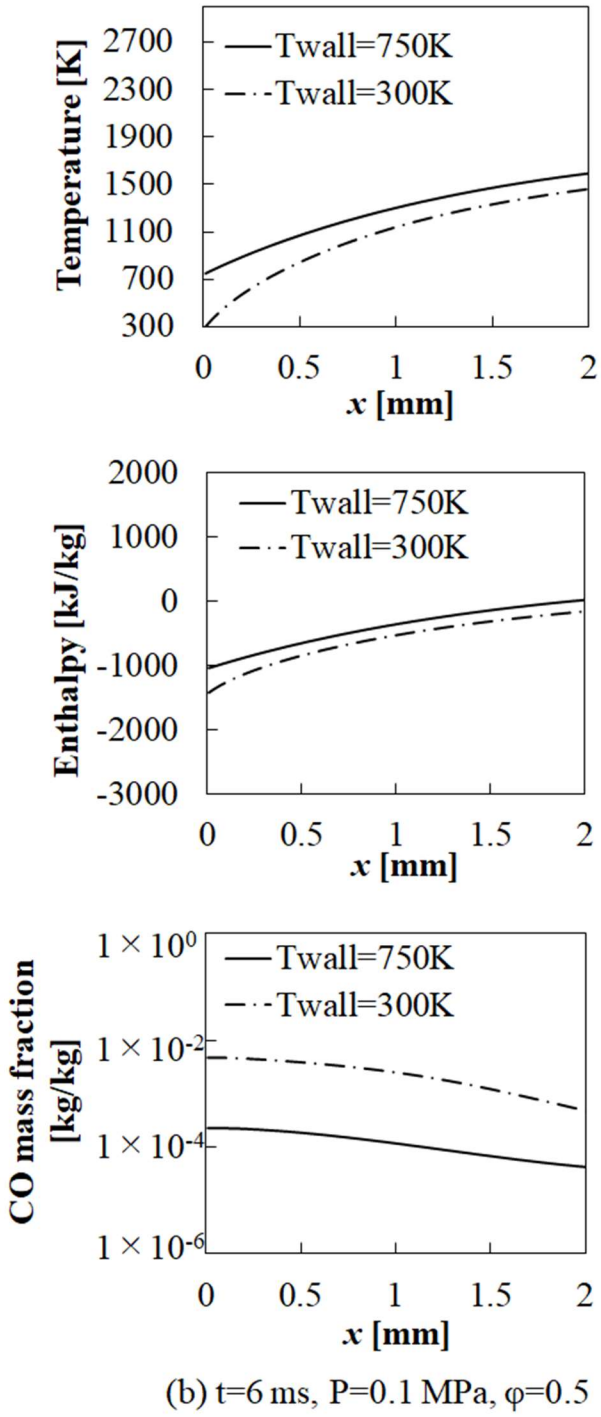

(b) t=6 ms, P=0.1 MPa, φ=0.5

Figure 2.10 Comparisons of instantaneous *x*-direction profiles of temperature, enthalpy and CO mass fraction in the vicinity of the wall at x = 0–2.0 mm under atmospheric pressure conditions between the wall temperatures T_{wall} of 750 K (Case 1-3) and 300 K (Case 1-9) (Continued).

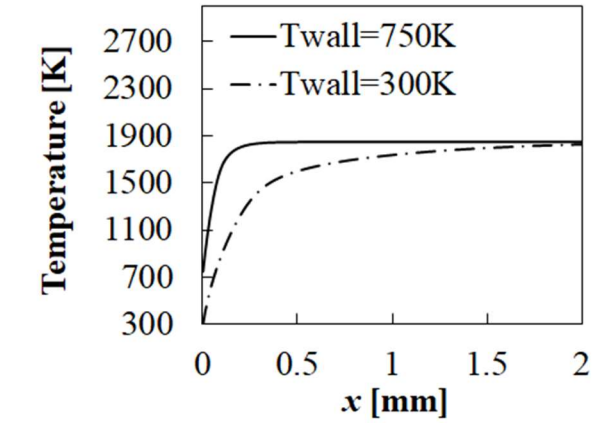

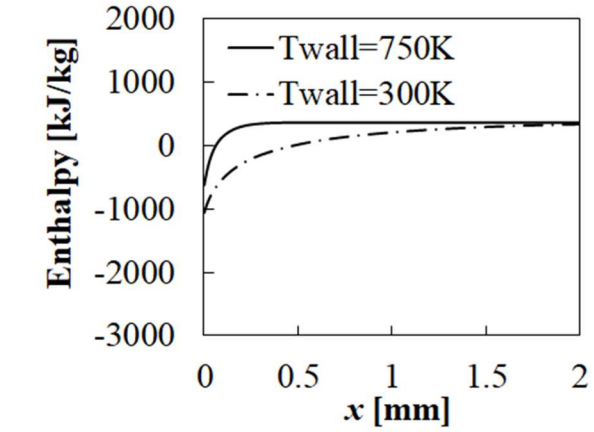

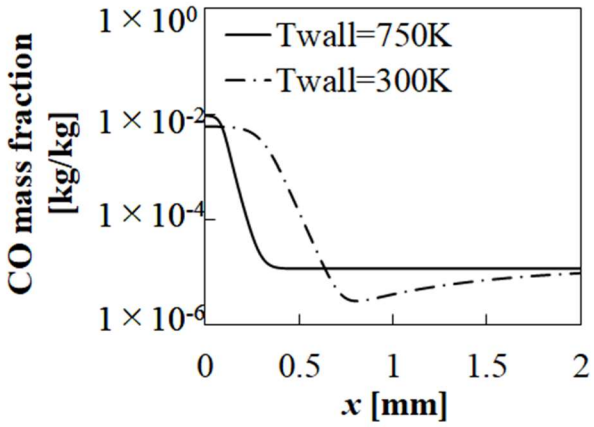

(a) t=0 ms, P=2.0 MPa, φ=0.5

Figure 2.11 Comparisons of instantaneous *x*-direction profiles of temperature, enthalpy, and CO mass fraction in the vicinity of the wall at *x* = 0–2.0 mm under high pressure conditions between the wall temperatures T_{wall} of 750 K (Case 1-6) and 300 K (Case 1-10) (Continues).

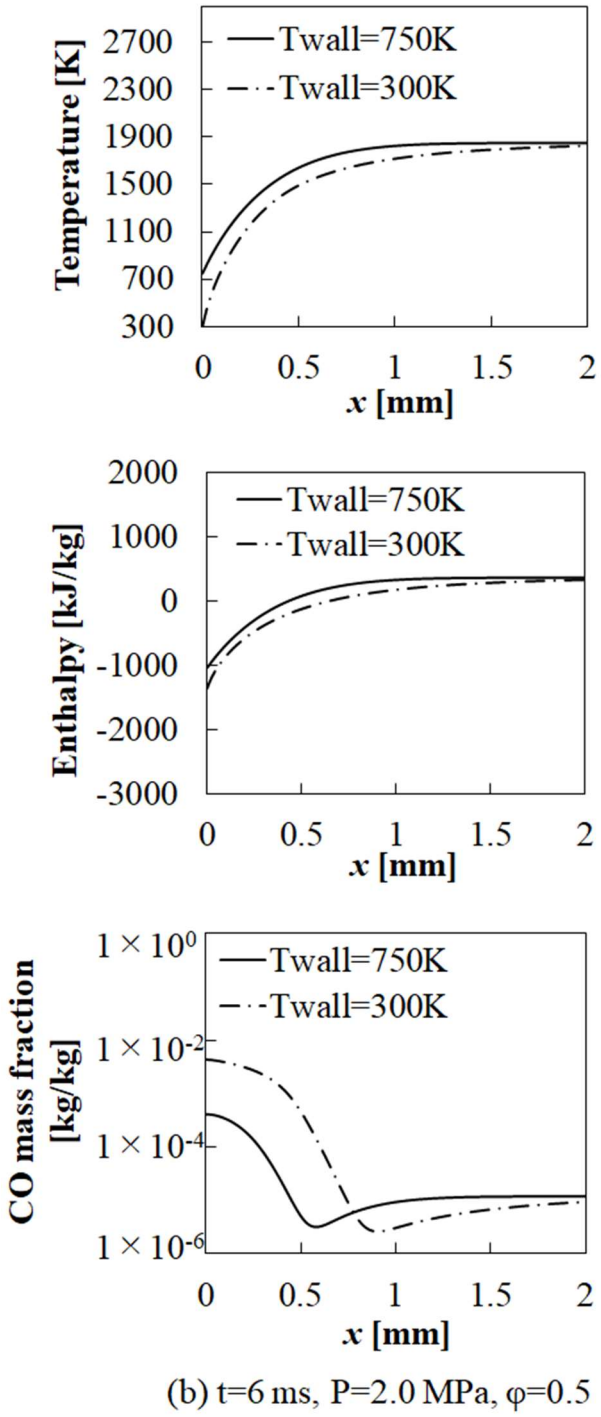

Figure 2.11 Comparisons of instantaneous *x*-direction profiles of temperature, enthalpy, and CO mass fraction in the vicinity of the wall at x = 0–2.0 mm under high pressure conditions between the wall temperatures T_{wall} of 750 K (Case 1-6) and 300 K (Case 1-10) (Continued).

2.3.2 Two-dimensional (2D) numerical simulation

2.3.2.1 Effect of wall temperature on CO emissions for detailed reaction mechanism approach

In this section, the results for the case of the detailed reaction mechanism approach are described. Figure 2.12 shows the comparisons of the time series of distributions of gas temperature, enthalpy and the CO mass fraction between the wall temperatures T_{wall} of 750 K (Case 2-1) and 300 K (Case 2-2). Output times are 0 ms, 0.9 ms and 2.1 ms, respectively. Figure 2.13 shows the comparisons of the time series of values of gas temperature, difference in enthalpy, and CO and CH_4 mass fractions at the point (a) between the wall temperatures T_{wall} of 750 K (Case 2-1) and 300 K (Case 2-2). The vertical axis denotes gas temperature, the difference in enthalpy, CO mass fraction and CH_4 mass fraction, and the horizontal axis is for time. Point (a) is set at -1.35 mm away from central position of calculation domain in the *x*-direction and at 0.35 mm away from the cooled wall in the *y*-direction. This point is just above the wall where the flame first reaches. The difference in enthalpy is defined as the difference from the initial value.

The flame structure becomes complicated by the effect of turbulent eddies set as the thin reaction zones regime. This flame reaches the cooled wall (*y*-direction) before propagating to outlet (*x*-direction). Under lower wall temperature condition, time taken for the flame to reach the cooled wall is shorter, as is apparent from the temperature and CH_4 mass fraction distributions in figure 2.13. This is because the flame under higher wall temperature condition tends to propagate equally in the *x*- and *y*-directions due to reduced heat loss of the premixed fuel. Conversely, since premixed fuel under lower wall temperature condition loses much heat, the flame is prone to propagate primarily in the *y*-direction, in this case. Although this tendency does not always occur, it is found that the direction of flame propagation changes with wall temperature despite equal initial turbulence. For both wall temperatures, the decrease in enthalpy near the cooled wall can be seen in the figure 2.12. Due to the decrease in enthalpy, gas temperature near the cooled wall is reduced. Meanwhile, CO is formed in the flame surface defined as the large temperature gradient. The maximum amount of CO formation under lower wall temperature condition at approximately 0.5 ms is smaller than that under higher wall temperature condition because flame temperature is lower. However, at 1 ms later, the

CO mass fraction at lower wall temperature becomes larger than that at higher wall temperature. This result shows that the CO consumption rate under the lower wall temperature condition is lower than that under the higher wall temperature condition. This change in CO consumption rate equates with the one-dimensional numerical simulation. It is suggested that accurate consideration of wall temperature is important in order to improve the prediction accuracy of the CO consumption rate for a gas turbine combustor.

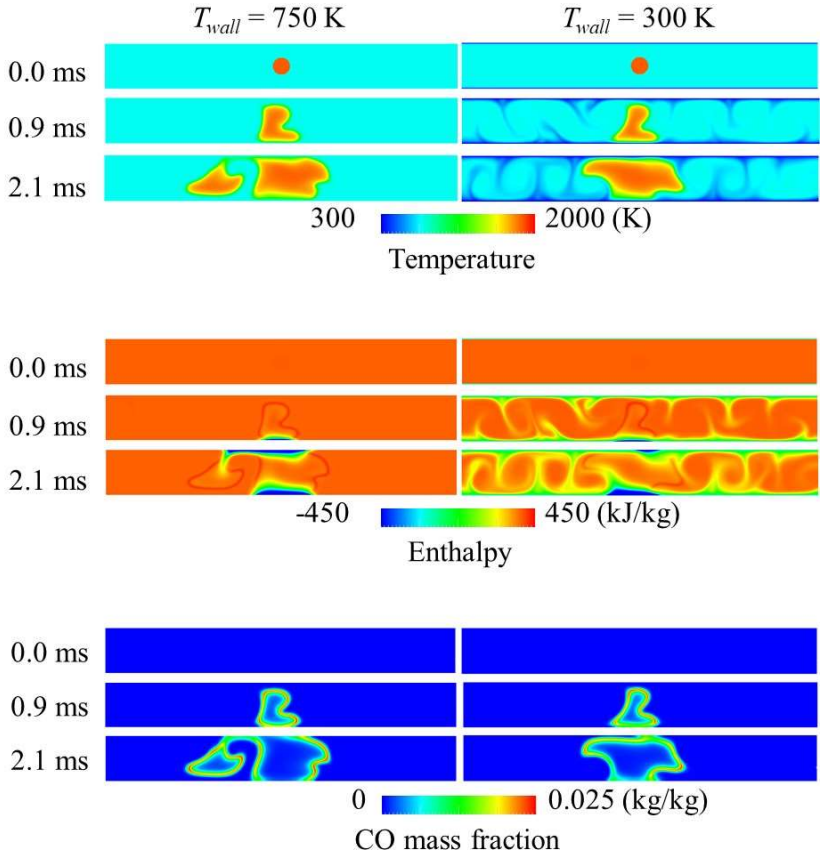

Figure 2.12 Comparisons of time series of distributions of gas temperature, enthalpy and CO mass fraction for detailed reaction mechanism approach between the wall temperatures T_{wall} of 750 K (Case 2-1) and 300 K (Case 2-2).

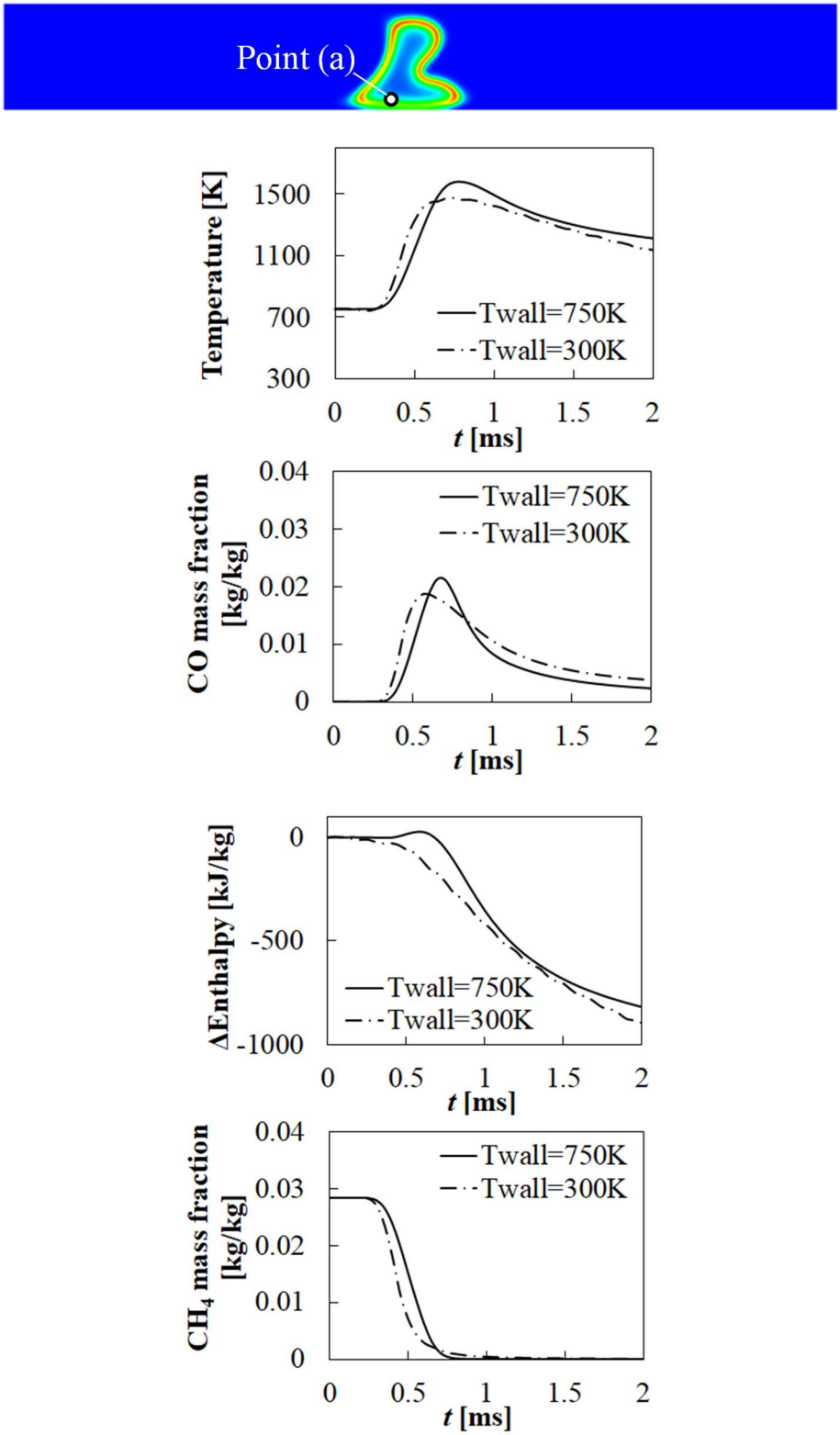

Figure 2.13 Comparisons of time series of gas temperature, difference in enthalpy, and CO and CH_4 mass fractions at the point (a) for detailed reaction mechanism approach between the wall temperatures T_{wall} of 750 K (Case 2-1) and 300 K (Case 2-2).

2.3.2.2 Flame characteristics for non-adiabatic flamelet generated manifolds approach

Figure 2.14 shows the comparisons of time series of distributions of progress variable, temperature and enthalpy for the NA-FGM approach between the wall temperatures T_{wall} of 750 K (Case 2-1) and 300 K (Case 2-2). Output times are 0 ms, 0.9 ms, and 2.1 ms, respectively. As time progresses, high progress variable propagates in the *x*- and *y*-directions. As a result, the high-temperature region expands throughout the calculation domain. When the flame reaches the cooled wall, the enthalpy rapidly decreases. The flame propagation velocity at a low wall temperature is lower than that at a high wall temperature. These trends reproduce the calculation results of the detailed reaction mechanism approach described in Section 2.3.2.1.

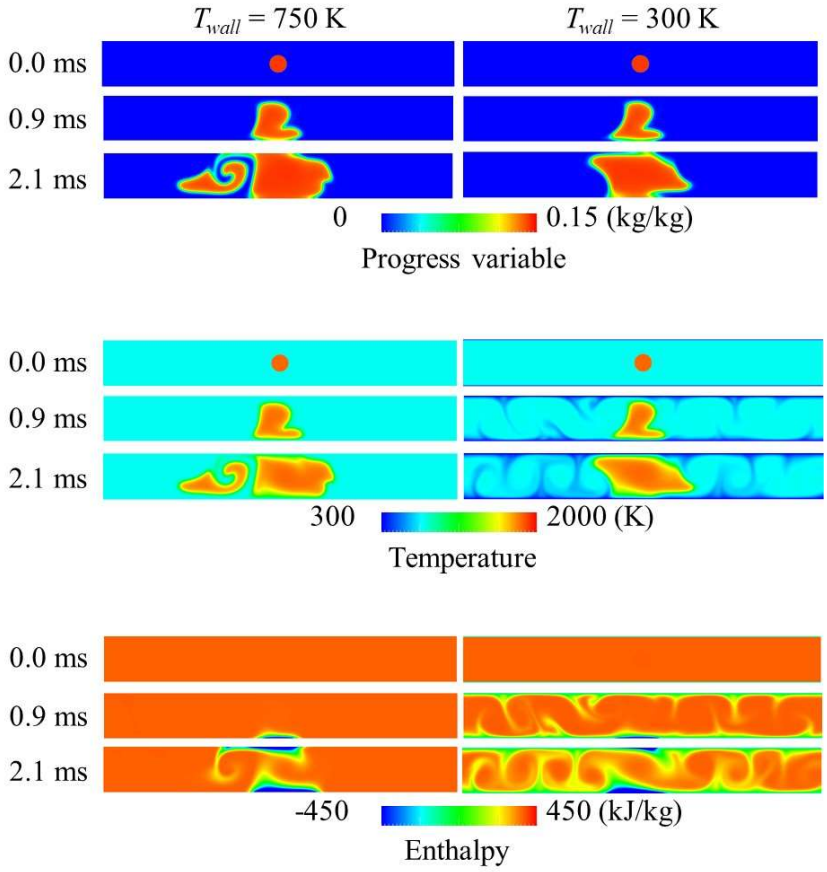

Figure 2.14 Comparisons of time series of distributions of progress variable, temperature and enthalpy for NA-FGM approach between the wall temperatures T_{wall} of 750 K (Case 2-1) and 300 K (Case 2-2).

2.3.2.3 Effect of wall temperature on CO emissions for non-adiabatic flamelet generated manifolds approach

Figure 2.15 shows the comparisons of time series of distributions of CO, OH and CO_2 mass fractions using the NA-FGM approach between the wall temperatures T_{wall} of 750 K (Case 2-1) and 300 K (Case 2-2). Output times are 0 ms, 0.9 ms, and 2.1 ms, respectively. Figure 2.16 shows the comparisons of time series of values of gas temperature, CO, OH and CO_2 mass fractions at the point (a) for the wall temperatures T_{wall} of 750 K (Case 2-1) between the detailed reaction mechanism approach and the NA-FGM approach. Figure 2.17 shows the same graphs as Figure 2.16, except at a wall temperature T_{wall} of 300 K (Case 2-2).

As shown in figure 2.15, CO is formed at the flame front surface and converted to CO_2 by oxidation reaction. It is known that CO oxidation occurs mainly by reaction with OH radicals. Therefore, a high OH mass fraction region is generated inside CO formation position and is reduced with CO to generate CO_2.

When the flame first attaches to the cooled wall, the results for the NA-FGM approach, except for the OH mass fraction, are in good agreement with the results for the detailed reaction mechanism approach. The OH mass fraction by the NA-FGM approach also follows the trend of the time series of the detailed reaction mechanism approach. However, there is the quantitative difference of the OH mass fraction. This is due to the flamelet modeling considering the flamelet library constructed by the equilibrium composition. For this reason, the prediction of an intermediate product, such as an OH radical, by the NA-FGM approach is not accurate. Conversely, the trend of CO formation/consumption in the vicinity of the wall for the NA-FGM approach is in good agreement with the detailed reaction mechanism approach. The CO mass fraction in the vicinity of the wall predicted using the NA-FGM approach tends to decrease due to the effect of heat loss through the cooled wall at each wall temperature. In addition, the calculation time for the NA-FGM approach was about 87% less than that for the detailed reaction mechanism approach. For the combustor development, it is useful to predict CO emissions by applying the NA-FGM approach.

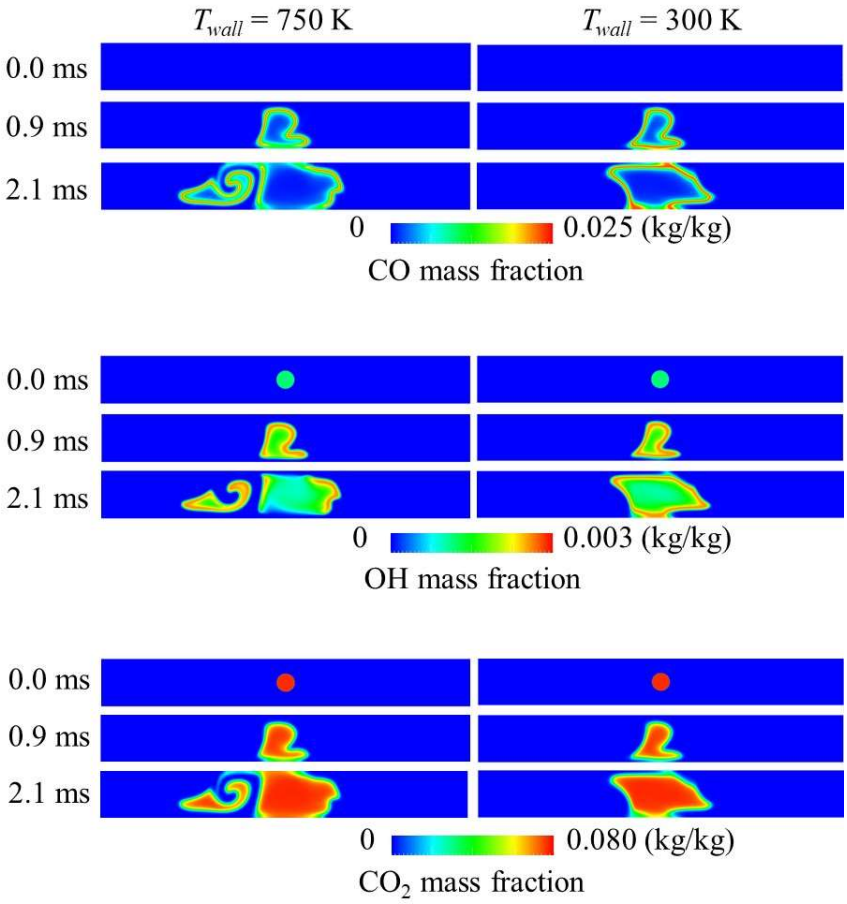

Figure 2.15 Comparisons of time series of distributions of CO mass fraction, OH mass fraction and CO_2 mass fraction for NA-FGM approach between the wall temperatures T_{wall} of 750 K (Case 2-1) and 300 K (Case 2-2).

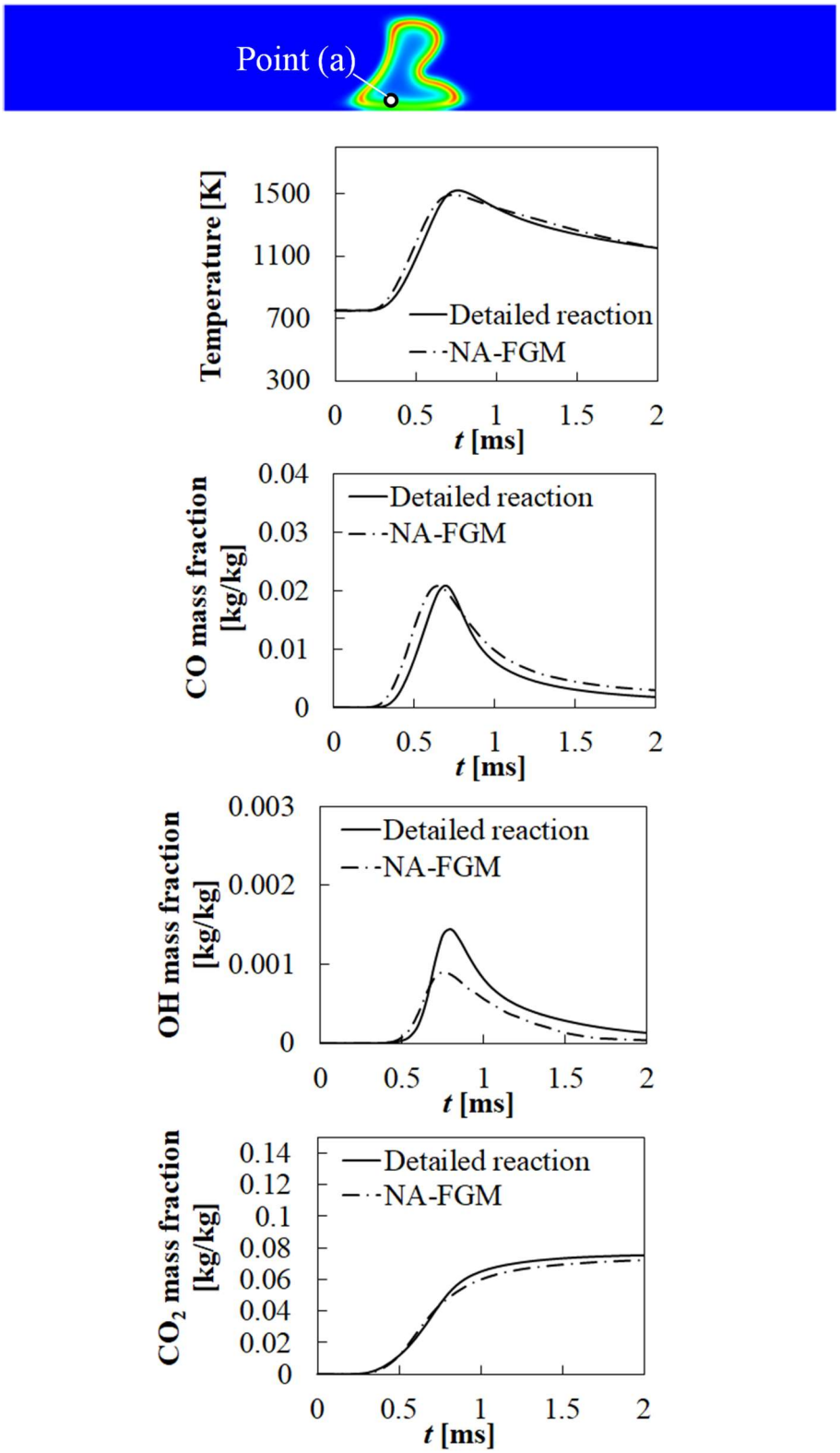

Figure 2.16 Comparisons of time series of values of gas temperature, CO, OH and CO_2 mass fractions at the point (a) for the wall temperatures T_{wall} of 750 K (Case 2-1) between the detailed reaction mechanism approach and NA-FGM approach.

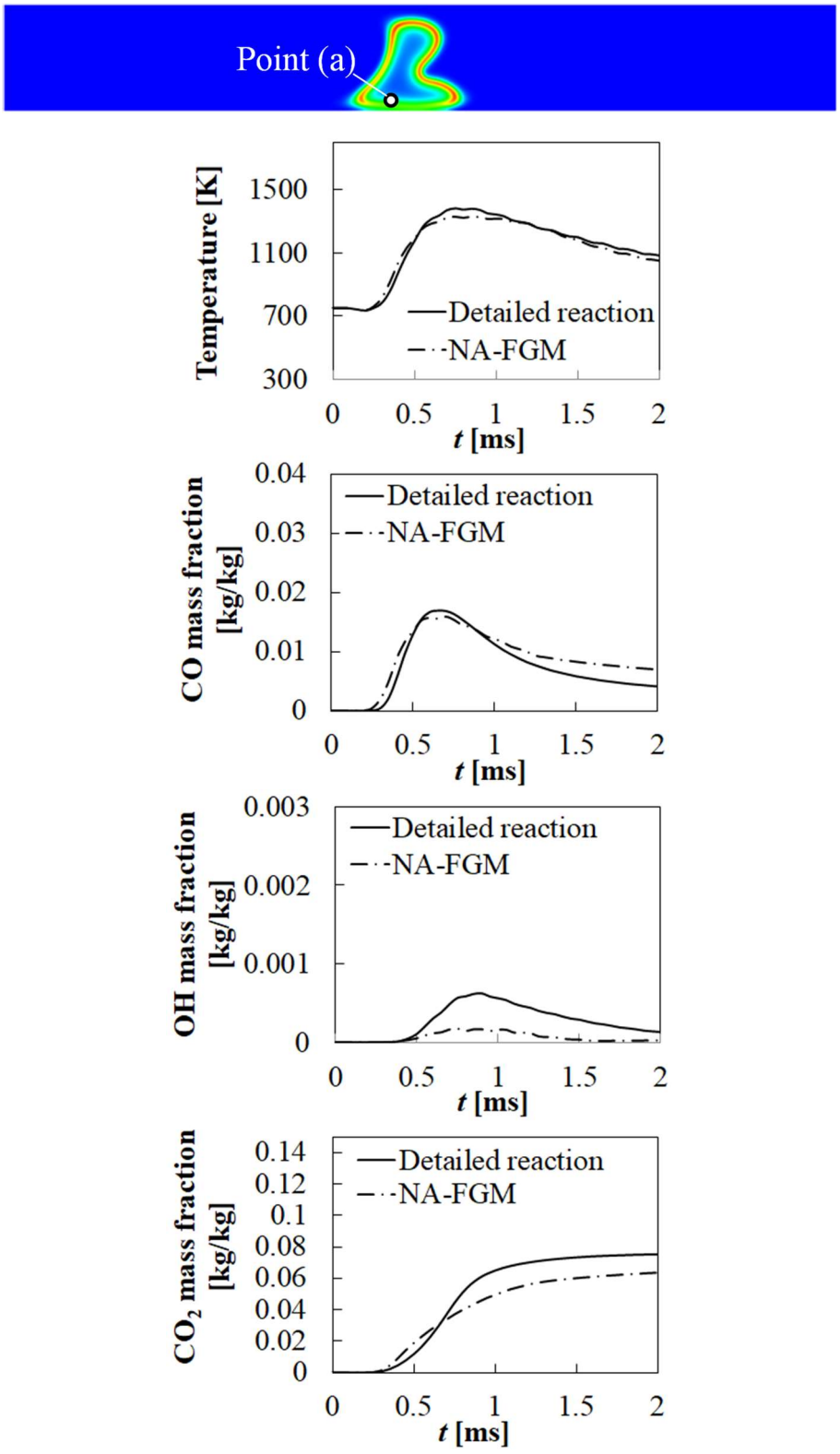

Figure 2.17 Comparisons of time series of values of gas temperature, CO, OH and CO_2 mass fractions at the point (a) for the wall temperatures T_{wall} of 300 K (Case 2-2) between the detailed reaction mechanism approach and NA-FGM approach.

2.4 Conclusions

In this study, 1D numerical simulations (employing a detailed reaction mechanism approach) and 2D numerical simulations (employing a detailed reaction mechanism approach and NA-FGM approach) were applied to CH_4–air premixed combustion fields near the cooled wall, and the effects of the equivalence ratios (0.5, 0.7 and 1.0), pressures (0.1 and 2.0 MPa) and wall temperatures (300 and 750 K) on the CO emissions were investigated in detail.

It was revealed by the 1D numerical simulations that the CO consumption rate in the vicinity of the cooled wall was reduced and consequently posed a risk of increasing the CO emissions at the combustor exit for lower equivalence ratio, higher pressure, or lower wall temperature. The CO consumption rate was most susceptible to the wall temperature. Similarly, these tendencies were observed in the 2D numerical simulations considering turbulent eddies. These results suggested that the heat loss control through the cooled walls could be an important key to effectively reduce CO emissions from combustors.

Furthermore, it was revealed that the NA-FGM approach can reproduce the results of the detailed reaction mechanism approach for flame characteristics at different wall temperatures. This is because the NA-FGM approach takes account of the heat loss near the cooled wall. Additionally, the NA-FGM approach was capable of capturing the reduction trend, observed by the detailed reaction mechanism approach, of the CO consumption rate by decreasing the wall temperature. Moreover, the computational cost of the NA-FGM approach was one-seventh that of the detailed reaction mechanism approach. However, the flamelet library is larger and more complicated.

In conclusion, these results suggest that the NA-FGM approach is effective for predicting CO emissions for turbulent lean premixed combustion in combustors.

References

[1] S., Fukuba, Y., Kimura, Y., Tanaka, M., Isono, S., Takiguchi, T., Saitoh, and K., Saitoh, “EXPERIMENTAL AND NUMERICAL INVESTIGATION OF DLN COMBUSTOR FOR A HEAVY-DUTY GAS TURBINE”, Proceedings of the 1st Global Power and Propulsion Forum GPPF-2017-165 (2017).

[2] K., Tada, K., Inoue, T., Kawakami, K., Saitoh, and S., Tanimura, “EXPANDING FUEL FLEXIBILITY IN MHPS’ DRY LOW NOX COMBUSTOR”, Proceedings of ASME Turbo Expo 2018, GT2018-77164 (2018).

[3] K., Fujimoto, Y., Fukunaga, S., Hada, T., Ai, M., Yuri, and J., Masada, “TECHNOLOGY APPLICATION TO MHPS LARGE FLAME F SERIES GAS TURBINE”, Proceedings of ASME Turbo Expo 2018, GT2018-77274 (2018).

[4] G., Cabot, D., Vauchelles, B., Taupin, and A., Boukhalfa, “Experimental study of lean premixed turbulent combustion in a scale gas turbine chamber,” Experimental Thermal and Fluid Science 28 683–690 (2004).

[5] M., Mann, C., Jainski, M., Euler, B., Bohm, and A., Dreizler, “Transient flame–wall interactions: Experimental analysis using spectroscopic temperature and CO concentration measurements”, Combustion and Flame 161 2371–2386 (2014).

[6] K., Yunoki, T., Murota, K., Miura, and T., Okazaki, “Numerical Simulation of Turbulent Combustion Flows for Coaxial Jet Cluster Burner”, Proceedings of the ASME 2013 Power Conference, POWER2013-98143 (2013).

[7] T., Koganezawa, K., Miura, T., Saitou, K., Abe, and H., Inoue, “Full Scale Testing of a Cluster Nozzle Burner for the Advanced Humid Air Turbine”, Proceedings of the ASME Turbo EXPO 2007, GT2007-27737 (2007).

[8] K., Yunoki and T., Murota, “Large Eddy Simulation to Predict Flame Front Position for Turbulent Lean Premixed Jet Flame at High Pressure”, Proceedings of the ASME Turbo EXPO 2018, GT2018-75601 (2018).

[9] K., Yunoki, T., Murota, T., Asai, and T., Okazaki, T., “Large Eddy Simulation of a Multiple-Injection Dry Low NOx Combustor for Hydrogen-Rich Syngas fuel at High Pressure”, Proceedings of the ASME Turbo EXPO 2016, GT2016-58119 (2016).

[10] S., Tachibana, K., Saito, T., Yamamoto, M., Makida, T., Kitano, and R., Kurose, “Experimental and numerical investigation of thermo-acoustic instability in a liquid-fuel aero-engine combustor at elevated pressure: Validity of large-eddy simulation of spray combustion”, Combustion and Flame 162 2621-2637 (2015).

[11] T., Nishiie, M., Makida, N., Nakamura, and R., Kurose, “Large-eddy simulation of turbulent spray combustion field of full annular combustor for aircraft engine”, Proceedings of International Gas Turbine Congress 2015 (2015).

[12] K., Hirano, Y., Nonaka, Y., Kinoshita, M., Muto, and R., Kurose, “Large-eddy simulation of turbulent combustion in multi combustors for l30a gas turbine engine”, Proceedings of the ASME Turbo EXPO 2015 (2015).

[13] H., Moriai, R., Kurose, H., Watanabe, Y., Yano, F., Akamatsu, and S., Komori, “Large-eddy simulation of turbulent spray combustion in a subscale aircraft jet engine combustor - predictions of no and soot concentrations”, Journal of Engineering for Gas Turbines and Power 135 (2013).

[14] M., Ihme, and H., Pitsch., “Modeling of radiation and nitric oxide formation in turbulent nonpremixed flames using a flamelet/progress variable formulation”, Physics of Fluids 20, 055110 (2008).

[15] F. A., Sethian, “Level Set Methods, Cambridge Mono-graphs on Applied and Computational Mathematics”, Cambridge University Press, Cambridge, U.K, (1996).

[16] F. A., Willams, “The Mathematics of Combustion”, SIAM, p.99-131 (1985).

[17] J. A. v., Oijen, and L. P. H. d., Goey., “Modeling of pre-mixed laminar flames using flamelet-generated manifolds”, Combustion Science and Technology 161, 113-137 (2000).

[18] B., Fiorina, R., Baron, O., Gicquel, D., Thevenin, S., Carpentier, and N., Darabiha, “Modelling non-adiabatic partially premixed flames using flame-prolongation of ILDM”, Combustion Theory and Modeling, Vol. 7, pp. 449-470 (2003).

[19] F., Proch, and A. M., Kempf., “Modeling heat loss effects in the large eddy simulation of a model gas turbine combustor with premixed flamelet generated manifolds”, Proceedings of the Combustion Institute 35, 3337-3345 (2015).

[20] B., Fiorina, R., Mercier, G., Kuenne, A., Ketelhen, A., Avdic, J., Janicka, D., Geyer, A., Dreizer, E., Alenius, C., Duwig, P., Trisjono, K., Kleinheinz, S., Kang, H., Oitsch, F., Proch, F. C., Morincola, and F., Kempf, “Challenging modeling strategies for LES of non-adiabatic turbulent stratified combustion”, Combustion and Flame, Vol. 162, pp. 4264-4282 (2015).

[21] P., Patangi, A., Sadiki, J., Janicka, M., Mann, and A., Dreizler, “LES of Premixed Methane Flame Impinging on the Wall Using Non-adiabatic Flamelet Generated Manifold (FGM) Approach”, Flow Turbulence Combust 92:805–836, DOI 10.1007/s10494-013-9526-0 (2014).

[22] T., Honzawa, R., Kai, A., Okada, J., Kawasaki, R., Tominaga, A., Valera-Medina, P. J., Bowen, and R., Kurose, “Large-eddy simulation of ammonia/methane/air combustion using non-adiabatic flamelet generated manifold approach”, Energy, 186, 115771 (2019).

[23] H., Pitsch, “Large-Eddy Simulation of Turbulent Combustion”, Annual Review of Fluid Mechanics, 38, 453-482 (2006).

[24] E., Knudsen, Shashank, H., Pitsch, “Modeling partially premixed combustion behavior in multiphase LES”, Combustion and Flame, 162, 159–180 (2015).

[25] R. J., Kee, F. M., Rupley, and J. A., Miller, Chemkin-II: A Fortran chemical kinetics package for the analysis of gas-phase chemical kinetics, Sandia National Laboratories, Report SAND89-8009 (1989).

[26] G. P., Smith, D. M., Golden, M., Frenklach, N. W., Moriarty, B., Eiteneer, M., Goldenberg, GRI-mech 3.0, Gas Research Institute, available at http://www.me.berkeley.edu/gri_mech/.

[27] H., Pitsch, Flamemaster: A c++ computer program for 0d combustion and 1d laminar flame calculations. (1998).

[28] A., Kishimoto, H., Moriai, K., Takenaka, T., Nishiie, M., Adachi, A., Ogawara, and R., Kurose, “Application of a non-adiabatic flamelet/progress-variable approach to Large Eddy Simulation of H2/O2 combustion under a pressurized condition”, Journal of Heat Transfer, 139 124501 (2017).

[29] R., Kai, K., Takenaka, and R., Kurose, “Validity of non-adiabatic FGM approach for numerical simulation of flame propagation in the vicinity of the wall”, Proceedings of International Gas Turbine Congress 2019 (2019).

[30] K., Yunoki, R., Kai, S., Inoue, and R., Kurose, “Numerical Simulation of CO Concentration on Flame Propagation in the Vicinity of the Wall -Validity of Non-Adiabatic FGM Approach-”, International Journal of Gas Turbine, Propulsion and Power Systems, 11 (2020).

[31] N., Peters, “The turbulent burning velocity for large scale and small scale turbulence”, Journal of Fluid Mech. 384 p.107-132 (1999).

[32] R. S., Rogallo, “Numerical experiments in homogeneous turbulence”, NASA Technical Memorandum, 81315 (1981).

[33] T., Hara, M., Muto, T., Kitano, R., Kurose, and S., Komori, “Direct numerical simulation of a pulverized coal jet flame employing a global volatile matter reaction scheme based on detailed reaction mechanism”, Combustion and Flame 162, 4391-4407 (2015).

[34] A. L., Pillai, and R., Kurose, “Combustion noise analysis of a turbulent spray flame using a hybrid DNS/APE-RF approach”, Combustion and Flame 200, 168-191 (2019).

[35] M., Muto, K., Yuasa, and R., Kurose, “Numerical simulation of soot formation in pulverized coal combustion with detailed chemical reaction mechanism”, Advanced Powder Technology 29, 1119-1127 (2018).

[36] T., Kitano, T., Tsuji, R., Kurose, and S., Komori, “Effect of pressure oscillations on flashback characteristics in a turbulent channel flow”. Energy and Fuels, 29, 6815–6822 (2015).

[37] R., Kurose, Kyoto university, available at http://www.tse.me.kyoto-u.ac.jp/members/kurose/link.php.

[38] V., Titarev, and E., Toro, “Weno schemes based on upwind and centred tvd fluxes”, Computers & Fluids 34, 705-720 (2005).

[39] S., Gottlieb, and S. V., Shu., “Total variation diminishing runge-kutta schemes”, Mathematics of computation of the American Mathematical Society 67, 73-85 (1998).

Nomenclature

C	Progress variable [-]
C_p	Isobaric specific heat [J/kg/K]
D_h	Thermal diffusivity [m^2/s]
D_γ	Diffusion coefficient $\left(D_\gamma = \lambda/\rho C_p\right)$ [m^2/s]
h_k	Enthalpy of chemical species k [J/kg]
j_k	Mass diffusion flux of species k [kg/m^2s]
$\dot{m}_k$	Mass production rate of species k [kg/m^3s]
P	Pressure [Pa]
$\dot{q}_{loss}$	Source term of heat loss [W/m^3]
R	Gas constant [J/K/mol]
S_L	Laminar burning velocity [m/s]
T	Temperature [K]
u	Velocity vector [m/s]
V_k	Diffusion velocity of chemical species k [m/s]
W_k	Molecular weight of chemical species k [kg/mol]
Y_k	Mass fraction of chemical species k [-]
Z	Mixture fraction [-]

Greeks

α	Adjustment parameter
δ_L	Laminar flame thickness [m]
λ	Thermal conductivity [W/m/K]
τ	Shear stress tensor [Pa]
φ	Equivalence ratio [-]
μ	Viscosity [Pa·s]
ρ	Density [kg/m^3]
$\dot{\omega}_C$	Generation rate of progress variable [1/s]
$\dot{\omega}_k$	Chemical reaction rate of chemical species k [1/s]

Subscripts

f	Fuel
k	Chemical species
st	Stoichiometric air-to-fuel ratio
$wall$	Wall

Chapter 3: Large eddy simulation of premixed combustion in a model type of combustor

3.1 Introduction

In the development of gas turbine combustors, to prevent air pollution, it is important to reduce nitrogen oxide (NOx) and carbon monoxide (CO) emissions generated by the combustion of hydrocarbon fuels. To control NOx emissions, it is effective to reduce the local flame temperature by decreasing the equivalence ratio. In contrast, if the equivalence ratio is decreased to achieve a lean premixed combustion, the flame combustibility decreases. Therefore, there is a possibility that CO is discharged in large quantities [e.g., 1, 2]. Additionally, owing to the recent increase in renewable energy power generation, it is necessary to utilize a gas turbine to supplement an unstable power supply. Therefore, it is important to develop combustors capable of low emissions and stable combustion at low loads, unlike in a conventional combustor, which should operate stably at the maximum load.

A low-emission combustor was developed based on combustion experiments conducted in a high-pressure test rig at Mitsubishi Heavy Industries, Ltd. The experimental results suggest that CO formation and consumption in a gas turbine combustor occurs near a cooled wall with heat loss. However, the effect, i.e., quenching due to heat loss through the cooled wall on the CO consumption rate, has not been examined sufficiently because it is difficult to understand the CO formation and consumption behavior near such a wall as there are few measuring devices that can be used in a high-pressure environment.

Computational fluid dynamics (CFD) employing turbulent combustion approaches and turbulence models is expected to be a powerful tool for understanding high-pressure combustion behavior, as measurements are difficult to obtain. Particularly, a large eddy simulation (LES), which models an eddy smaller than the cell size, has been used for various applications recently, because the application of an LES to complex

reacting flows has been realistic with advancements in supercomputing performance [e.g., 2-8]. As a turbulent combustion approach, the flamelet approach [9], which utilizes the flame characteristics in the database (i.e., the flamelet library), is effective in terms of computational costs and is widely used instead of directly solving the Arrhenius equations when considering the detailed chemical reaction mechanisms. Generally, the flamelet approach includes two types depending on the target flame characteristics: a non-premixed (diffusion) flame and a premixed flame. For instance, the flamelet progress variable (FPV) approach [10] and flamelet generated manifolds (FGM) approach [11] are the representative flamelet methods developed for non-premixed and premixed flames, respectively. Regarding CO prediction using LES with the flamelet approach, Vreman et al. [12] applied LESs of Sandia Flame D and Flame F using non-premixed and premixed flamelet approaches and investigated their validity by comparing the obtained calculation results with the experiment results. However, they did not consider the effects of heat loss on the walls. In contrast, Donini et al. [13] applied the FGM approach by considering the heat loss effect on a premixed flame and examined the heat loss effect on CO emissions. However, no comparisons were made with the experimental results. To take the heat loss effect into account in the flamelet approach, a non-adiabatic procedure [14] was introduced in previous studies for non-premixed and premixed flames [15-19]. However, to assess the validity of CO prediction, comparisons with the experimental results are essential because of procedural complications.

Therefore, the purpose of this study is to apply an LES by employing a non-adiabatic FGM approach (referred to as "NA-FGM approach", hereafter), which can consider the effect of heat loss on the composition of the chemical species [14-17], to CH_4–air super lean premixed flames for equivalence ratios of φ = 0.43, 0.45, and 0.50 under pressurized conditions with heat loss through a cooled wall and to examine the validity of applicably to predict CO emissions based on a comparison with the experiment results. Furthermore, the effects of heat loss and equivalence ratio on CO emissions were investigated in detail.

3.2 Numerical methods

3.2.1 Flamelet generated manifolds (FGM) approach

The governing equations for the FGM approach [11] can be written as follows:

$$\frac{\partial \rho}{\partial t} + \nabla \cdot (\rho u) = 0 \tag{1}$$

$$\frac{\partial \rho u}{\partial t} + \nabla \cdot (\rho u u) = -\nabla P + \nabla \cdot \tau \tag{2}$$

$$\frac{\partial \rho h}{\partial t} + \nabla \cdot (\rho h u) = \frac{DP}{Dt} + \nabla \cdot (\rho D_h \nabla h) + \tau : \nabla u \tag{3}$$

$$\frac{\partial \rho Z}{\partial t} + \nabla \cdot (\rho Z u) = \nabla \cdot (\rho D_Z \nabla Z) \tag{4}$$

$$\frac{\partial \rho C}{\partial t} + \nabla \cdot (\rho C u) = \nabla \cdot (\rho D_C \nabla C) + \rho \dot{\omega}_C \tag{5}$$

where ρ is the density, u is the velocity vector, P is the pressure, τ is the shear stress tensor, h is the enthalpy, D_h is the thermal diffusivity, $\dot{\omega}_C$ is the generation reaction rate of progress variable C, C is the progress variable defined as the mass fraction of burned gas (H_2O, H_2, CO_2 and CO), D_γ is the diffusion coefficient $\left(D_\gamma = \lambda / \rho C_p\right)$, λ is the thermal conductivity, and C_p is the specific isopiestic heat. This approach requires a database called a flamelet library, which is generated using calculations involving a one-dimensional laminar premixed flame under various conditions, using the following governing equations:

$$\frac{\partial (\rho u)}{\partial x} = 0 \tag{6}$$

$$\rho u \frac{\partial Y_k}{\partial x} = -\frac{\partial j_k}{\partial x} + \dot{m}_k \tag{7}$$

$$\rho u C_p \frac{\partial T}{\partial x} = \frac{\partial}{\partial x}\left(\lambda \frac{dT}{dx}\right) - \sum_k C_p j_k \frac{\partial T}{\partial x} - \sum_k h_k \dot{m}_k \tag{8}$$

Thus, this library is obtained through detailed elementary reaction calculations. This database provides all filtered scalar quantities as functions of the filtered mixture fraction Z and filtered progress variable C.

3.2.2 Non-adiabatic procedure

In general, a premixed flame is generated within the vicinity of the cooled wall in gas turbine combustors. Therefore, we apply the NA-FGM approach [14] to include the effect of heat loss. The flamelet library, using the effect of the considered heat loss [16], is calculated using equations (6), (7) and (9).

$$\rho u C_p \frac{\partial T}{\partial x} = \frac{\partial}{\partial x}\left(\lambda \frac{\partial T}{\partial x}\right) - \sum_k C_p j_k \frac{\partial T}{\partial x} - \sum_k h_k \dot{m}_k + \dot{q}_{loss} \tag{9}$$

$$\dot{q}_{loss} = \alpha \sum_k h_k \dot{m}_k \tag{10}$$

where $\dot{q}_{loss}$ is the source term of heat loss and α is adjustment parameter. In this study, adjustment parameters from 0.0 to 0.4 were calculated every 0.05. The adjustment parameter is based on the maximum value of predicted heat loss. The maximum value of predicted heat loss was calculated by enthalpy of burnt gas at wall temperature. Flamelet library for NA-FGM approach is defined three variables (mixture fraction Z, progress variable C and difference of enthalpy Δh) in order to output some physical quantity. Difference of enthalpy Δh can be written as:

$$\Delta h = h_0 - h \tag{11}$$

where h_0 is enthalpy without heat loss, h is enthalpy obtained by eq. (3).

3.2.3 Calculation setup

In this study, a turbulent lean premixed combustion in the thin reaction zones regime, which is a combustion configuration of a gas turbine combustor in a turbulent premixed flame diagram as designed by Peters [20], was adopted as the object of verification. A schematic diagram of the calculation domain for the Paul Scherrer Institute burner [21, 22] is shown in Figure 3.1. The feature of this combustion test rig can be applied between the atmospheric pressure and high pressure (2.0 MPa). Moreover, corrugated flamelets, the thin reaction zones regime, and the broken reaction zones regime in the diagram of a turbulent premixed flame can be set as the experimental conditions. This rig is composed of a cooling casing, turbulence grid, fuel header, combustion chamber and exhaust pipe. The combustion air was preheated to 823 K using an electrical heater. After mixing air and fuel in the mixing section, high-pressure air and fuel formed in the fuel header flow into the combustion chamber (inner diameter D = 75 mm) through the turbulence grid (inner diameter d = 25 mm, hole diameter dg = 3 mm and blockage ratio bg = 65 %). The fuel reacts with the combustion air and a premixed flame then forms in the combustion chamber. The flue gases flow into the exhaust pipe. The axial direction from the upstream to the downstream of the burner indicates x, the height direction from the center of the combustion chamber indicates y, and the depth direction of the combustion chamber indicates z. Here, x = 0 mm is the inlet position from the fuel header to the combustion chamber, and y = 0 mm and z = 0 mm are the center axis of the combustion chamber in the figure.

The velocity in the combustion chamber was measured indirectly using particle image velocimetry (PIV). CO emissions at x = 300 mm were measured using sampling probe. Full details of the tests are available in the literature [21, 22], the data of which were taken for validation. Figure 3.2 shows a schematic diagram of the computational grids. The computational region was divided into approximately 24 million cells. The

control volume size close to the burner and in the reaction zone was approximately 0.01 mm, which was considered sufficient for the LES. The combustion chamber inner wall was set to be isothermal (300 K). The inner wall temperature was validated by comparing the calculation results with the experimental results at the outlet of the combustion chamber. At the outlet boundary, the Neumann boundary condition is imposed for pressure, with free outflow conditions being imposed for the other variables.

Table 3.1 lists the calculation conditions. The bulk inlet velocity U0 was 40 m/s. The fuel temperature was 293 K (non-reacting flow) or 673 K (reacting flow). The pressure at the chamber outlet was 1 bar (non-reacting flow) or 5 bar (reacting flow). The equivalence ratios were 0.43-0.50. Here, CH4 was used as the fuel. Calculations (reacting flow) were carried out for Cases 2-4 (LES/NA-FGM approach) to confirm the sensitivity for CO emissions. The consideration of heat loss in the flamelet library was excluded for Cases 5-7 (LES/A-FGM approach) to confirm the sensitivity of the heat loss effect. The governing equations are solved using an unstructured LES solver, i.e., FrontFlow/Red (FFR) extended by some research institutes, including Kyoto University, and referred to as FFR-Comb [e.g. 5-8, 15, 17]. The combustion field is treated as incompressible in a low Mach number approximation. The NA-FGM approach was previously implemented in the LES solver. The flamelet library is obtained through detailed elementary reaction calculations using the FlameMaster code [23]. The detailed reaction mechanism was applied to GRI-Mech 3.0, considering 53 species and 325 reaction steps [24]. A dynamic sub-grid scale model is applied as the turbulence model [25]. A first-order Euler implicit method was used for time advancement, and the time step was set to 1×10^{-6} s, which is based on a Courant-Friendrichs-Lewy (CFL) number of less than 1. The spatial derivative of the convective term in the momentum equation is approximated using a second-order central difference scheme of 95 % and a first-order upwind of 5 %. The turbulent Schmidt number and turbulent Prandtl number are set to 0.4. The statistics were collected for each case over three flow-through times, and all simulations were calculated for 10 ms using a CRAY: XE6 at the ACCMS, Kyoto University, with 544 cores and 40 h of wall clock time.

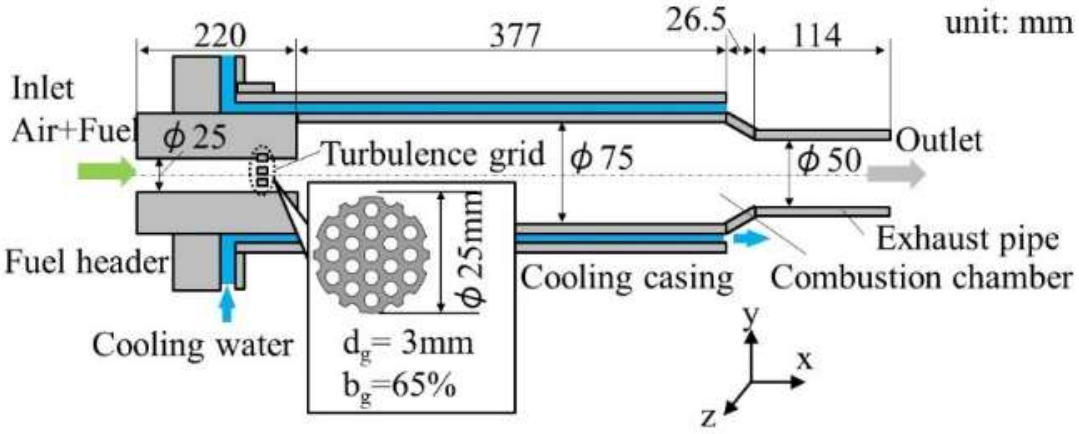

Figure 3.1 Schematic diagram of combustion test rig [21, 22].

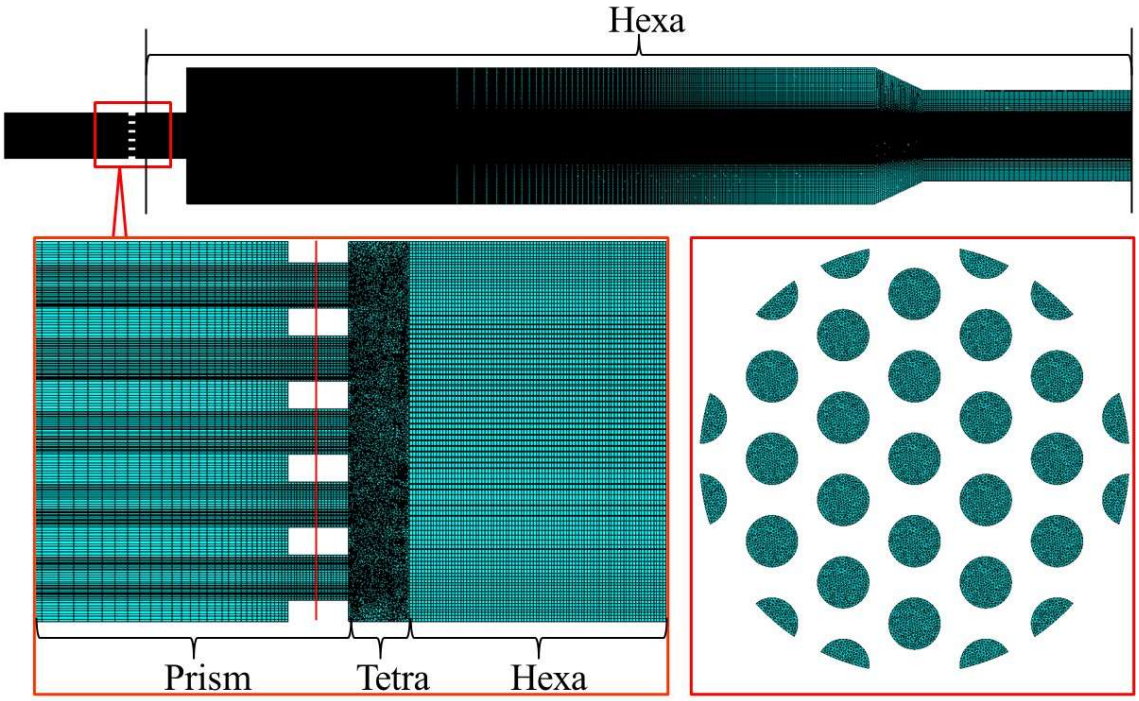

Figure 3.2 Schematic diagrams of computational grids.

Table 3.1 Calculation conditions.

Case	P (bar)	φ (-)	T_f (K)	T_{wall} (K)	$U0$ (m/s)	Reaction	Consideration of heat loss
1	1.0	-	293	293	40	Off	Off
2	5.0	0.43	673	300	40	On	On
3	5.0	0.45	673	300	40	On	On
4	5.0	0.50	673	300	40	On	On
5	5.0	0.43	673	300	40	On	Off
6	5.0	0.45	673	300	40	On	Off
7	5.0	0.50	673	300	40	On	Off

3.3 Results and discussions

3.3.1 Non-reacting flow

To assess the prediction accuracy of the velocity, a non-reacting flow (Case 1) was first applied using the calculation conditions given in Table 3.1. Figure 3.3 shows the distributions of the instantaneous, time-averaged and RMS streamwise velocities on the *x*-*y* plane for Case 1. It accelerates within the vicinity of the turbulence grid, which becomes a turbulent flow generator, and the variation value near the burner inlet (x = 0 mm) is high in region (A). The premixed fuel jet is gradually damped from the upstream of the φ25 mm burner to the φ75 mm combustion chamber, and the potential core disappeared at approximately x = 100 mm. The recirculation zone near the wall in region (B) was generated owing to the sudden expansion of the diameter from φ25 to φ75 mm. The velocity variation becomes large in shear layers where the velocity gradient is caused by the sudden expansion of the end of the potential core at point (C) or the inner diameter of the combustor is large at point (D).

Figures 3.4 and 3.5 show comparisons of the centerline profiles of the time-averaged and RMS streamwise velocities, and comparisons of the radial direction profiles of the time-averaged streamwise velocity at x = 25 mm and 175 mm between the LES (Case 1) and experiment [26], respectively. The values of the time-averaged and RMS streamwise velocities are normalized by an inlet bulk velocity of 40 m/s. The jet accelerated by the turbulence grid flows into the combustion chamber at above 40 m/s.

After that, the potential core of the flow gradually decays from approximately x = 100 to 300 mm. The calculation results overestimate the RMS values at approximately x = 0 mm. There is a possibility of underestimating the damping of turbulence fluctuations owing to the low-order difference scheme or the problem of a lattice resolution near the turbulence grid. However, good agreement with the experimental results is confirmed x = 50 mm downstream of the velocity field, which is important for a flame formation. The calculation results reproduce the tendency of the experimental results from the viewpoint of predicting the flame behavior.

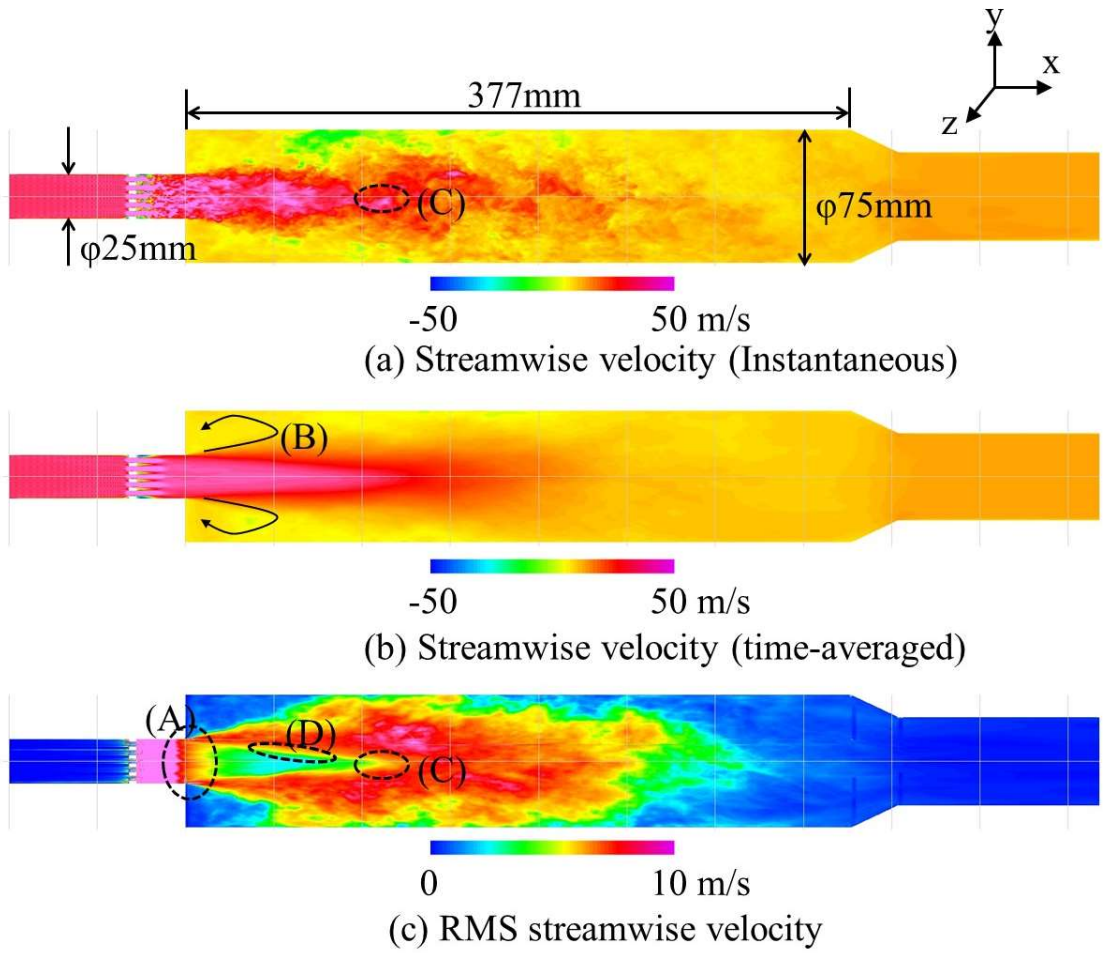

Figure 3.3 Distributions of instantaneous, time-averaged and RMS streamwise velocity on the x-y plane for Case 1.

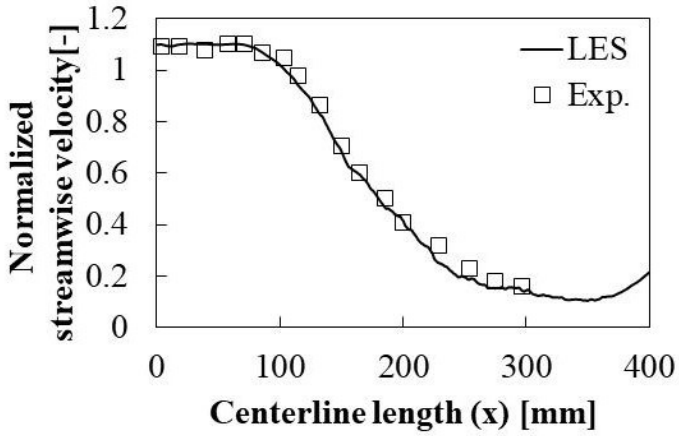

(a) Normalized streamwise velocity (time-averaged)

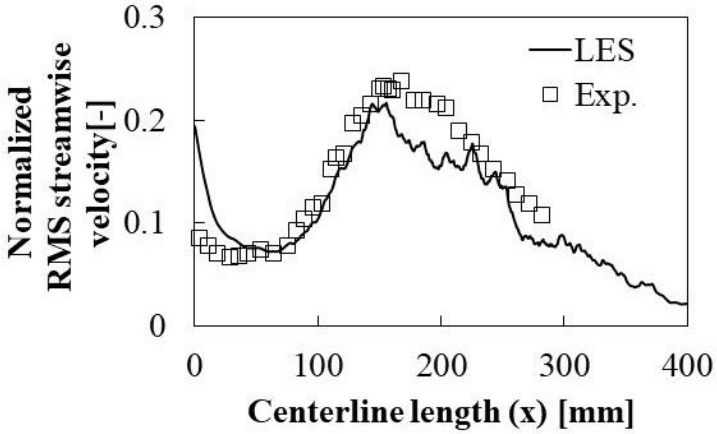

(b) Normalized RMS streamwise velocity

Figure 3.4 Comparisons of centerline profiles of time-averaged and RMS streamwise velocity between LES (Case 1) and experiment [26].

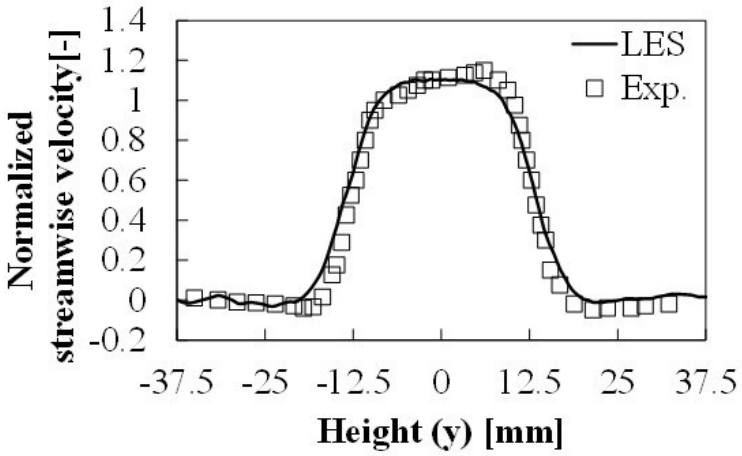

(a) x = 25 mm

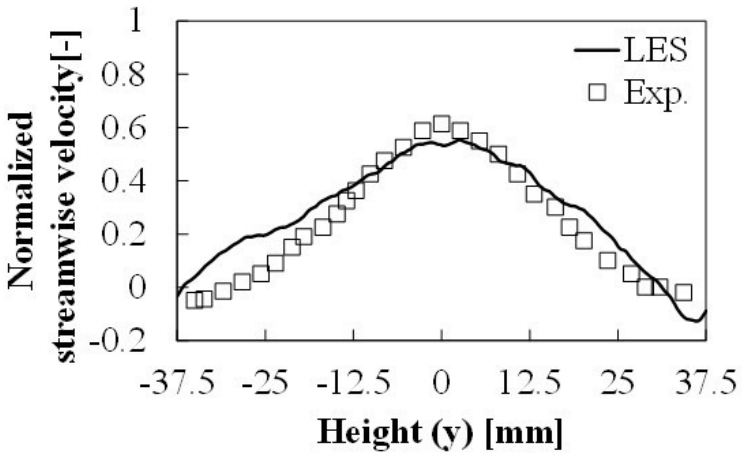

(b) x = 175 mm

Figure 3.5 Comparisons of radial direction profiles of time-averaged streamwise velocity at x = 25 mm and 175 mm between LES (Case 1) and experiment [26].

3.3.1 Reacting flow

3.3.1.1 Effect of equivalence ratios on flame length

Figures 3.6 shows the instantaneous iso-surfaces of progress variable $C = 0.1$, indicating flame fronts with the generation reaction rate of progress variable $\dot{\omega}_C$. Figures 3.7 the instantaneous distributions of temperature (top), enthalpy (middle), and progress variable (bottom) on the x-y plane for equivalence ratios of φ = 0.43, 0.45, and 0.50 predicted by LES/NA-FGM (Cases 2, 3 and 4, respectively). According to Figures 3.6 and 3.7, the flame front structure is complicated by the effect of the turbulence eddy, and the flame is stably maintained in the outer recirculation zone. The burnt high-temperature gas is returned to the combustion chamber inlet by the outer recirculation flow (marked as (E) in Figure 3.7) as shown in Figure 3.3 (B), thereby maintaining the flame. The outer recirculation zone has much higher temperatures than the central zone in the core flow (marked as (F) in Figure 3.7). However, the temperature in this zone (E) is lower than the downstream, which is due to the lost heat of the burnt gas through the cooled wall at point (G) in Figure 3.7. Moreover, the value of heat loss increases with an increase in the equivalence ratio. Despite the occurrence of heat loss through the wall, the progress variable near region (H) did not greatly decrease. In this burner, there is a high possibility that the flame length does not change even if the effect of heat loss on the chemical reaction is ignored. Hence, the flame length was evaluated by comparing the centerline profiles of the progression variables. Figure 3.8 shows comparisons of the centerline profiles of the time-averaged normalized progress variable for equivalence ratios of φ = 0.43, 0.45 and 0.50, as predicted by LES/NA-FGM (Cases 2, 3 and 4) and LES/A-FGM (Cases 5, 6 and 7). The time-averaged progress variable is normalized by the maximum value of each case. The flame length during super lean combustion is an important factor of the prediction of CO emissions and the blow-off limit. Here, the flame length is defined as from x = 0 mm to the position at the normalized progress variable of 0.5. The flame lengths of LES/NA-FGM were 163.43 mm for φ = 0.43, 155.11 mm for φ = 0.45, and 133.68 mm for φ = 0.50. The flame lengths of LES/A-FGM were 169.65 mm for φ = 0.43, 159.07 mm for φ = 0.45, and 125.85 mm for φ = 0.50. The unburnt zones, where the progress variable is defined as equal to zero, expands in the streamwise direction as the equivalence ratio decreases, as shown in Figure 8. As a result, the flame length is validated

to increase with a decrease in the equivalence ratio. This is because the lower the equivalence ratio is, the lower the flame propagation rate. In this study, the effect of the equivalence ratio on the flame length was larger than that of the heat loss. Moreover, the difference in flame length between the flamelet library with heat loss and that without heat loss is significantly small.

Although the flame length of LES/NA-FGM for $\varphi = 0.50$ (133.68 mm) is in good agreement with the experimental results (140 mm), the effect of the decrease in the equivalence ratio on the extension of the flame length is small for lower equivalence ratio conditions, and the difference in the flame length between $\varphi = 0.45$ and $\varphi = 0.43$ is significantly small. Therefore, it is necessary to improve the prediction accuracy of the flame length under the condition of $\varphi = 0.43$, which is near the blow-off limit. To improve the prediction accuracy of the flame length, a flame stretch effect can be introduced into the NA-FGM approach. The thin reaction zones regime targeted in this study has three effects: the flame stretch effect, the diffusion enhancement effect of the preheated regime owing to the turbulent flow vortex, and the increasing rate of the flame surface area. The decrease in the flame propagation rate is caused by the flame stretch effect. Previous studies [3] have suggested that introducing a flame stretch effect [27] into the combustion approach improves the prediction accuracy of the flame length, particularly under lower equivalence ratio conditions. Further consideration is needed to yield any findings regarding the introduction of the flame stretch effect into the NA-FGM approach to improve the prediction accuracy of the flame length.

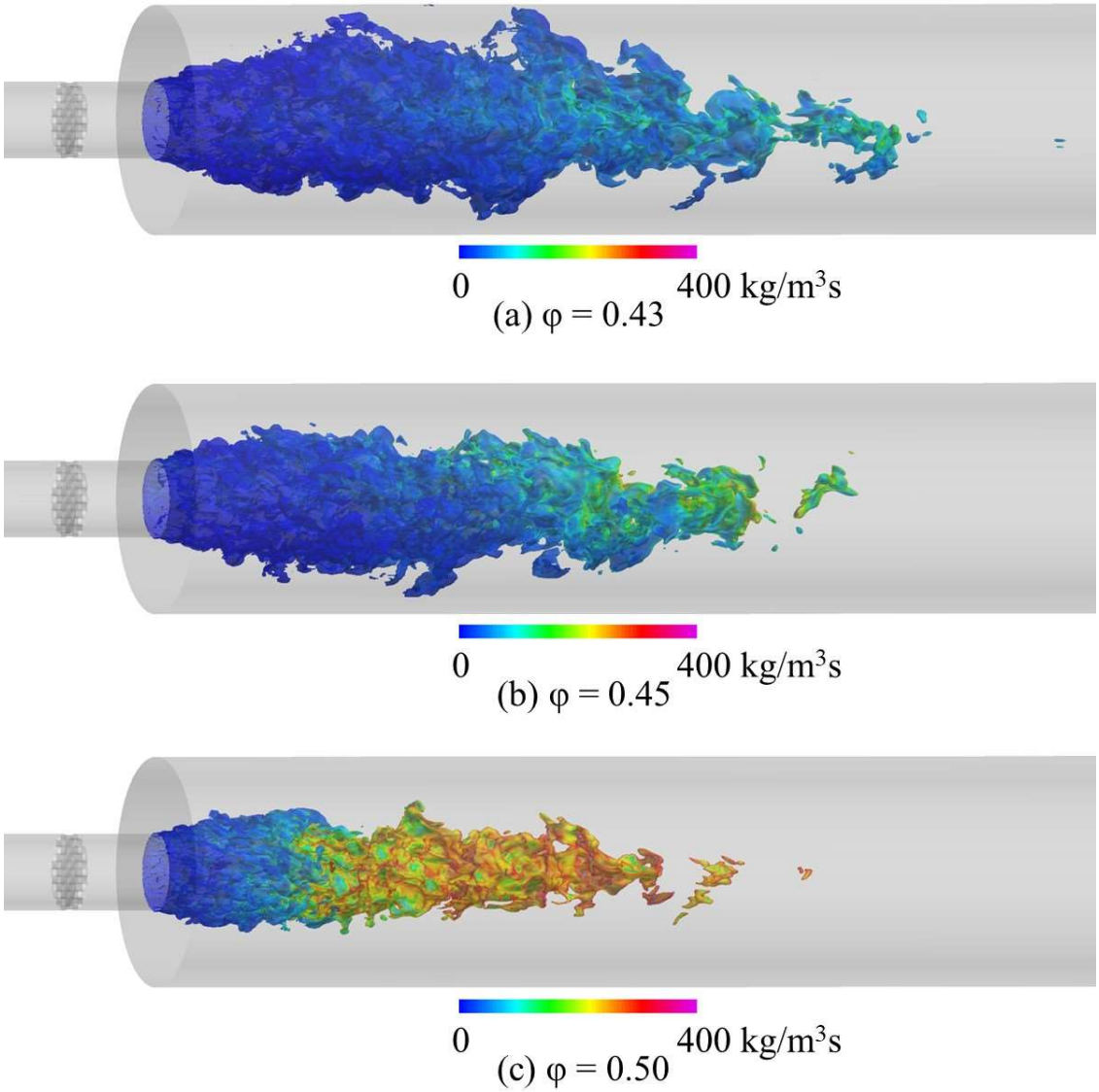

Figure 3.6 Instantaneous iso-surfaces of progress variable with the generation reaction rate of progress variable $\dot{\omega}_C$ for equivalence ratios of φ = 0.43, 0.45 and 0.50 predicted using LES/NA-FGM (Cases 2, 3 and 4, respectively).

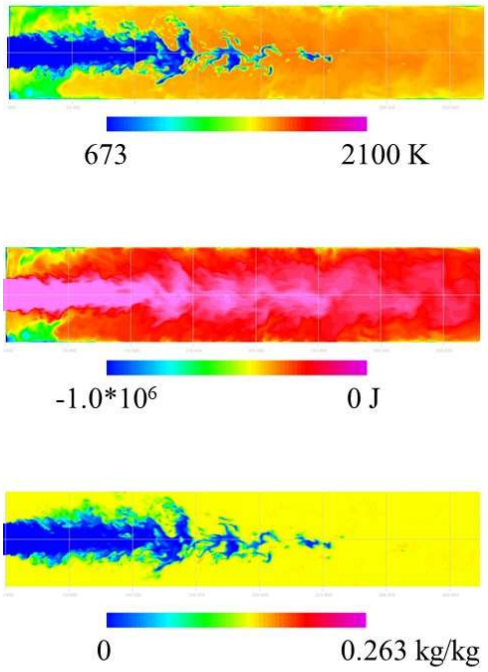

(a) φ = 0.43

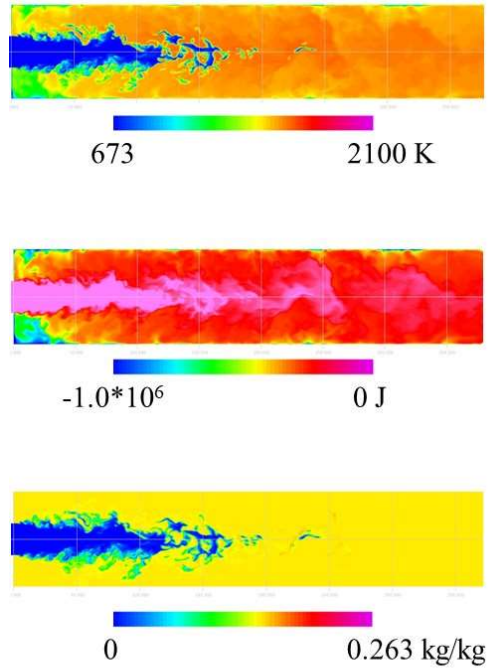

(b) φ = 0.45

Figure 3.7 Instantaneous distributions of temperature (top), enthalpy (middle), and progress variable (bottom) on the *x*-*y* plane for equivalence ratios of φ = 0.43, 0.45 and 0.50, predicted using LES/NA-FGM (Cases 2, 3 and 4, respectively) (Continues).

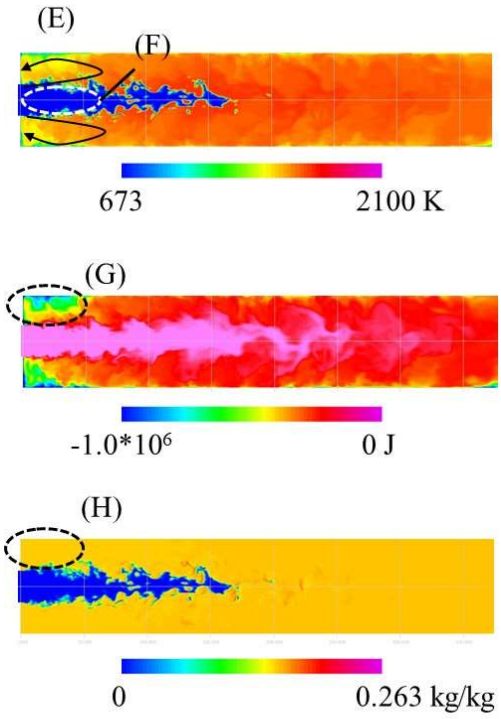

(c) φ = 0.50

Figure 3.7 Instantaneous distributions of temperature (top), enthalpy (middle), and progress variable (bottom) on the *x*-*y* plane for equivalence ratios of φ = 0.43, 0.45 and 0.50, predicted using LES/NA-FGM (Cases 2, 3 and 4, respectively) (Continued).

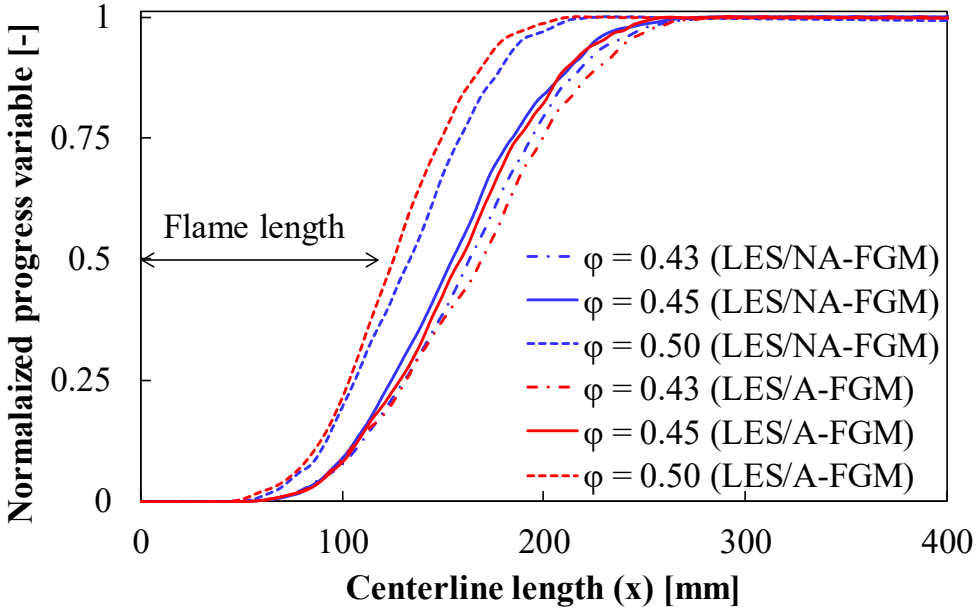

Figure 3.8 Comparisons of centerline profiles of time-averaged normalized progress variable for equivalence ratios of φ = 0.43, 0.45 and 0.50, predicted using LES/NA-FGM (Cases 2, 3 and 4) and LES/A-FGM (Cases 5, 6 and 7).

3.3.1.2 Effect of heat loss through the cooled wall on CO emissions

Figures 3.9 and 3.10 show a comparison of the time-averaged CO and NO emissions on the centerline at x = 300 mm among LES/NA-FGM (Cases 2, 3 and 4), LES/A-FGM (Cases 5, 6 and 7) and experiment [21], respectively. The experimental results show that the CO emissions increase, and the NO emissions decrease for leaner equivalence ratio conditions. The CO emissions of the experiments are approximately 28.0 ppm for φ = 0.43, 5.8 ppm for φ = 0.45, and 1.1 ppm for φ = 0.50. The NO emissions of experiments are approximately 0.5 ppm for φ = 0.43, 0.7 ppm for φ = 0.45, and 1.2 ppm for φ = 0.50. The trends of the CO and NO emissions obtained by LES/NA-FGM show good agreement with the experimental results. By contrast, in the case of LES/A-FGM, although the NO emissions are in good agreement with the experimental results, CO emissions for richer equivalence ratio is overestimated and CO emissions for leaner equivalence ratio is underestimated. Furthermore, we evaluated the factors leading to the high prediction accuracy of CO by LES/NA-FGM. Figures 3.11-13 show a comparison of the centerline profiles of the time-averaged CO volume fraction between LES/NA-FGM (Cases 2, 3 and 4) and LES/A-FGM (Cases 5, 6 and 7) for φ = 0.43, 0.45 and 0.50. The CO volume fraction between the LES/A-FGM and LES/NA-FGM peaks at approximately x = 100 mm in the streamwise direction. It was found that the CO formation rate was almost the same regardless of the heat loss. By contrast, the CO consumption rate for LES/NA-FGM is slower than that for LES/A-FGM according to the distribution of the CO volume fraction at x = 100mm downstream in the streamwise direction. Moreover, the CO emissions of LES/A-FGM under richer equivalence ratio conditions are high because the CO of the equilibrium composition without a heat loss is extracted from the flamelet library at x = 300 mm, as shown in Figure 11. The CO volume fraction at x = 220 mm downstream in the case of LES/A-FGM was found to be maintained for Case 5. By contrast, the CO volume fraction at x = 300 mm of the leaner equivalence ratios (φ = 0.43 and 0.45) did not reach equilibrium even in the LES/A-FGM. This tendency is considered to cause an underestimation of the CO emissions owing to the faster CO consumption rate of the LES/A-FGM. These findings suggest that the difference in CO emissions downstream is caused by the CO consumption rate. Figure 3.14 shows a comparison of the CO formation and consumption rates for each equivalence ratio. The peak of the CO formation and consumption rates under richer

conditions is higher than that under leaner conditions. Therefore, the calculation results confirmed that the high CO concentration region for the leaner conditions tends to be maintained until x = 300 mm because the CO consumption rate is lower.

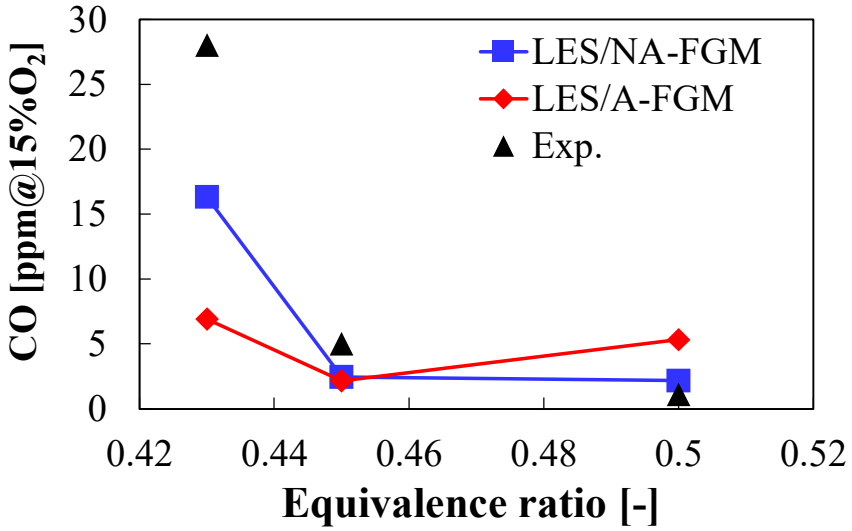

Figure 3.9 Comparison of time-averaged CO emissions on the centerline at x = 300mm among LES/NA-FGM (Cases 2, 3 and 4), LES/A-FGM (Cases 5, 6 and 7) and experiment [21].

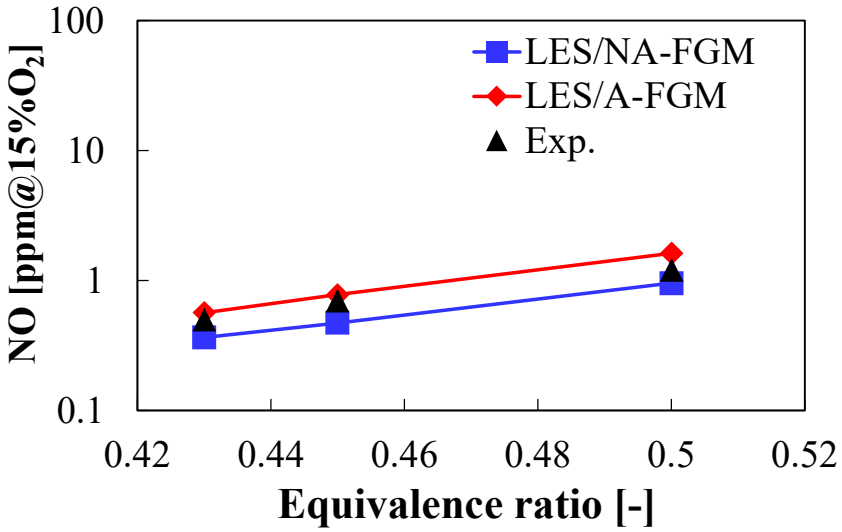

Figure 3.10 Comparison of time-averaged NO emissions on the centerline at x = 300mm among LES/NA-FGM (Cases 2, 3 and 4), LES/A-FGM (Cases 5, 6 and 7) and experiment [21].

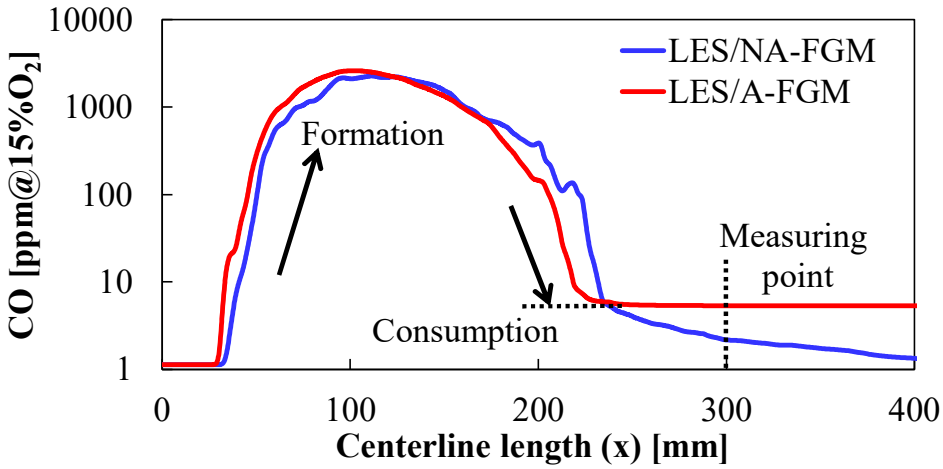

Figure 3.11 Comparison of centerline profiles of time-averaged CO volume fraction for φ = 0.50 between LES/NA-FGM (Case 2) and LES/A-FGM (Cases 5).

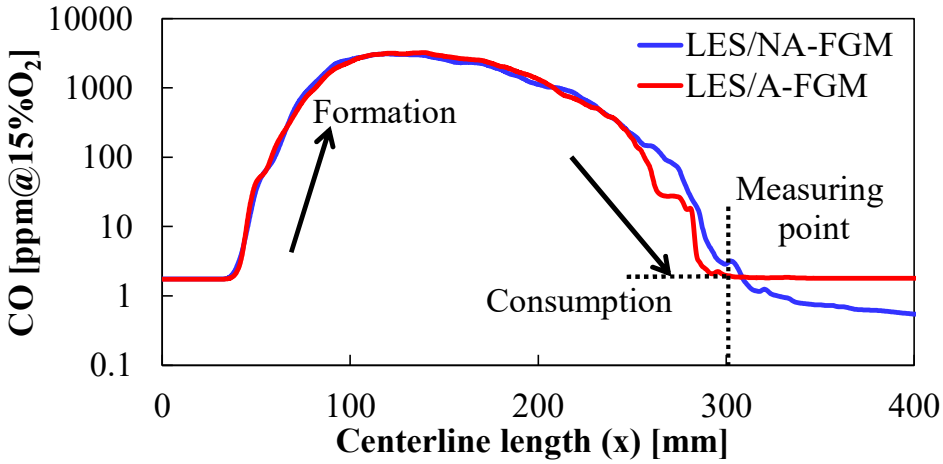

Figure 3.12 Comparison of centerline profiles of time-averaged CO volume fraction for φ = 0.45 between LES/NA-FGM (Case 3) and LES/A-FGM (Cases 6).

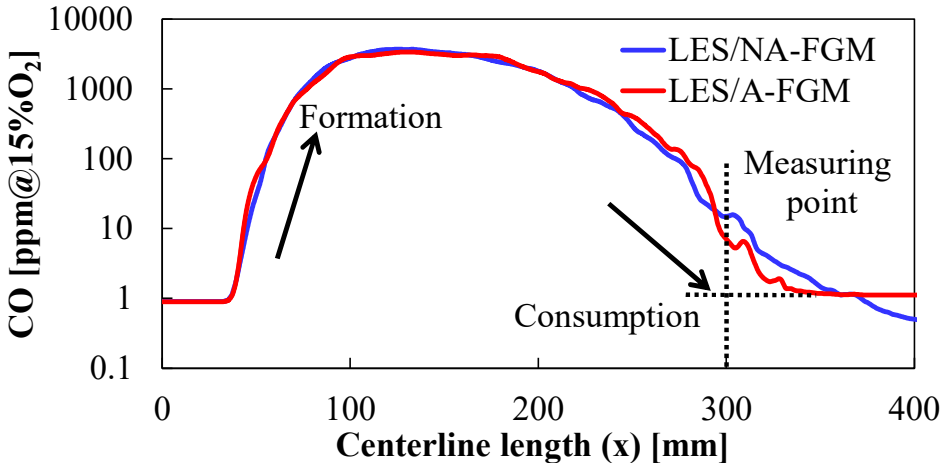

Figure 3.13 Comparison of centerline profiles of time-averaged CO volume fraction for φ = 0.43 between LES/NA-FGM (Case 4) and LES/A-FGM (Cases 7).

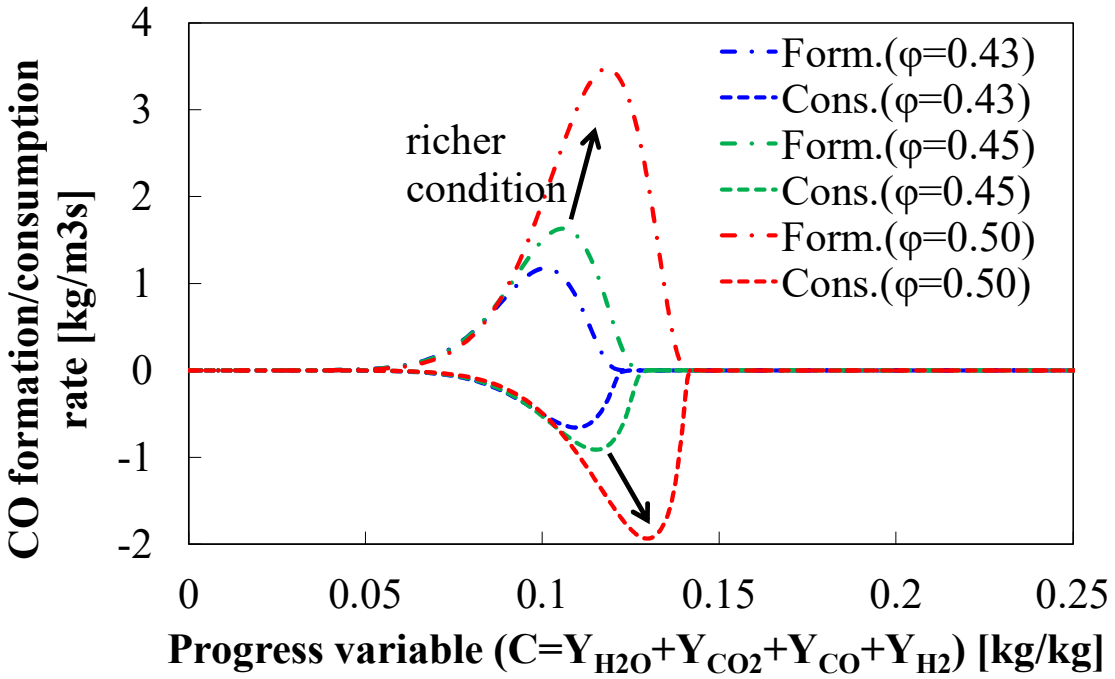

Figure 3.14 Comparison of CO formation/consumption rates in the flamelet library for Δh = 1021181.

Figures 3.15-17 show comparisons of the time-averaged distributions of the source term of the progress variable (top), CO mass fraction (middle) and OH mass fraction (bottom) on the *x*-*y* plane for each equivalence ratio between LES/NA-FGM (Cases 2, 3 and 4) and LES/A-FGM (Cases 5, 6 and 7). First, the effect of heat loss on the total reaction is evaluated according to the distribution of the production rate of the progress variable. The reaction of LES/NA-FGM is activated downstream of the burner (marked as (I), (J), and (K) in Figures 3.15-17, respectively). By contrast, the reaction by LES/A-FGM occurs rapidly near the burner (marked as (L), (M), and (N) in Figures 15-17, respectively). Under the condition of an equivalence ratio of 0.43, the reaction is activated 50 mm downstream of the burner. In particular, this tendency is more apparent under leaner premixed combustion conditions. It is considered that the slow reaction made it easier for CO to remain downstream. The CO formation position is then evaluated. The thickness of the high CO mass fraction layer expands by decreasing the equivalence ratio (marked as (O), (P), and (Q) in Figures 15-17, respectively). These results imply that this is one of the factors of large CO emissions at lower equivalence ratios. In addition, it is considered that the CO consumption rate is a more important factor for increasing the

CO emissions. Here, the prediction accuracy of OH radicals is important because the OH radical is dominant for the CO consumption reaction as shown in equation (12).

$$CO + OH \rightarrow CO_2 + H_2O \quad (12)$$

There is a difference in the OH radical distribution between LES/A-FGM and LES/NA-FGM. When the heat loss through the cooled wall is not considered (LES/A-FGM), the OH mass fraction is asymptotic to the equilibrium value. By contrast, the OH radical by LES/NA-FGM is consumed downstream, and the OH mass fraction gradually decreases (marked as (R), (S), and (T) in Figures 3.15-17, respectively). This difference greatly affects the CO consumption rate. In addition, Figure 18 shows a comparison of the production rates of the CO mass fraction in the flamelet library for $\varphi = 0.43$. As the reaction proceeds, the order of CO formation and consumption does not change owing to the effect of heat loss. Although the CO formation rate becomes lower owing to the effect of heat loss, it was less susceptible to the effect of heat loss through the cooled wall because CO was generated on the unburnt fuel side (the center side of the combustion chamber) as shown in Figures 3.15-17. By contrast, the CO consumed near the cooled wall was strongly affected by heat loss, and the CO consumption rate decreased with increasing heat loss, as shown in Figure 18. Hence, the difference in the CO consumption rate between LES/A-FGM and LES/NA-FGM is caused by heat loss through the cooled wall. As described in previous section, the flame length does not change between LES/A-FGM and LES/NA-FGM for the same equivalence ratio. Therefore, the change in CO emissions is caused by the decrease in the CO consumption rate owing to heat loss.

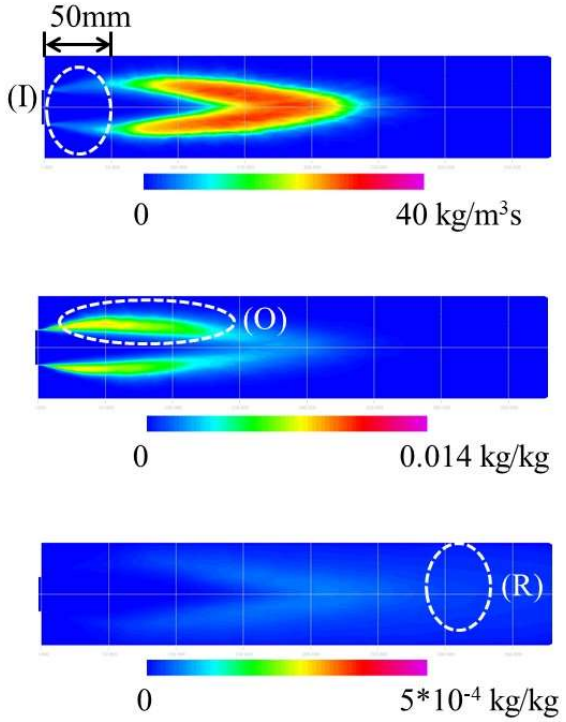

(a) LES/NA-FGM

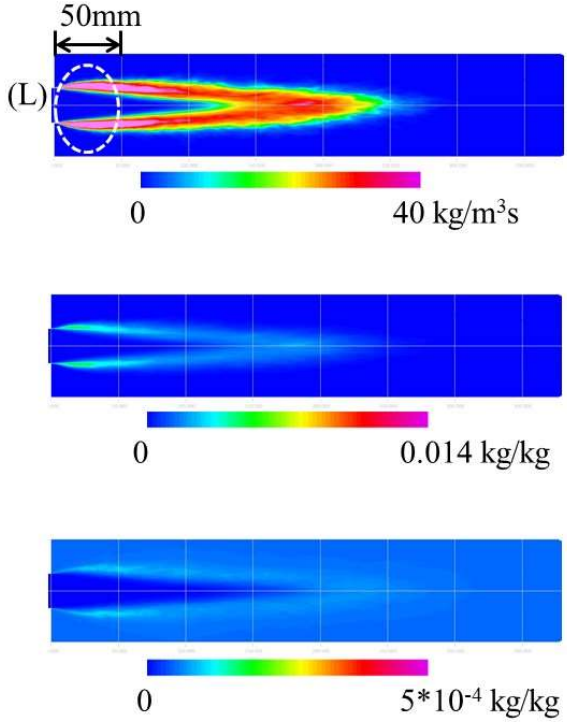

(b) LES/A-FGM

Figure 15 Comparison of the time-averaged distributions of source term of progress variable (top), CO mass fraction (middle) and OH mass fraction (bottom) on the *x*-*y* plane for φ = 0.43 between LES/NA-FGM (Case 2) and LES/A-FGM (Case 5).

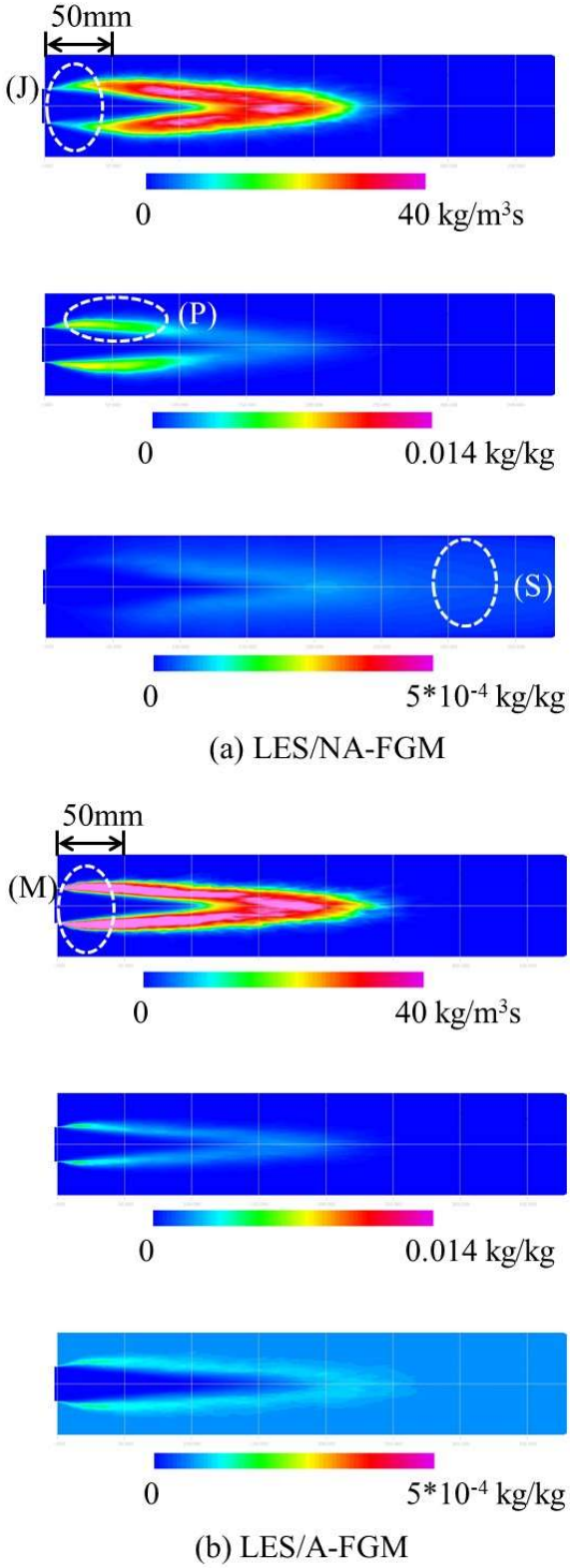

Figure 16 Comparison of the time-averaged distributions of source term of progress variable (top), CO mass fraction (middle) and OH mass fraction (bottom) on the *x*-*y* plane for φ = 0.45 between LES/NA-FGM (Case 3) and LES/A-FGM (Case 6).

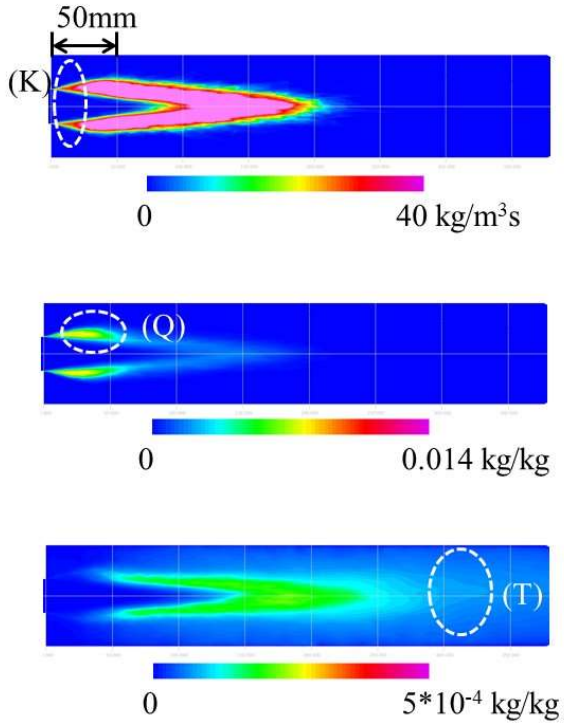

(a) LES/NA-FGM

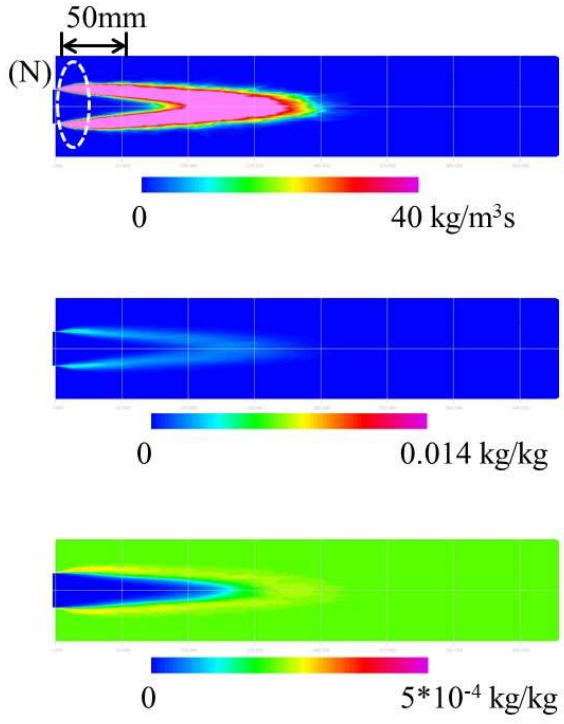

(b) LES/A-FGM

Figure 17 Comparison of the time-averaged distributions of source term of progress variable (top), CO mass fraction (middle) and OH mass fraction (bottom) on the *x*-*y* plane for φ = 0.50 between LES/NA-FGM (Case 4) and LES/A-FGM (Case 7).

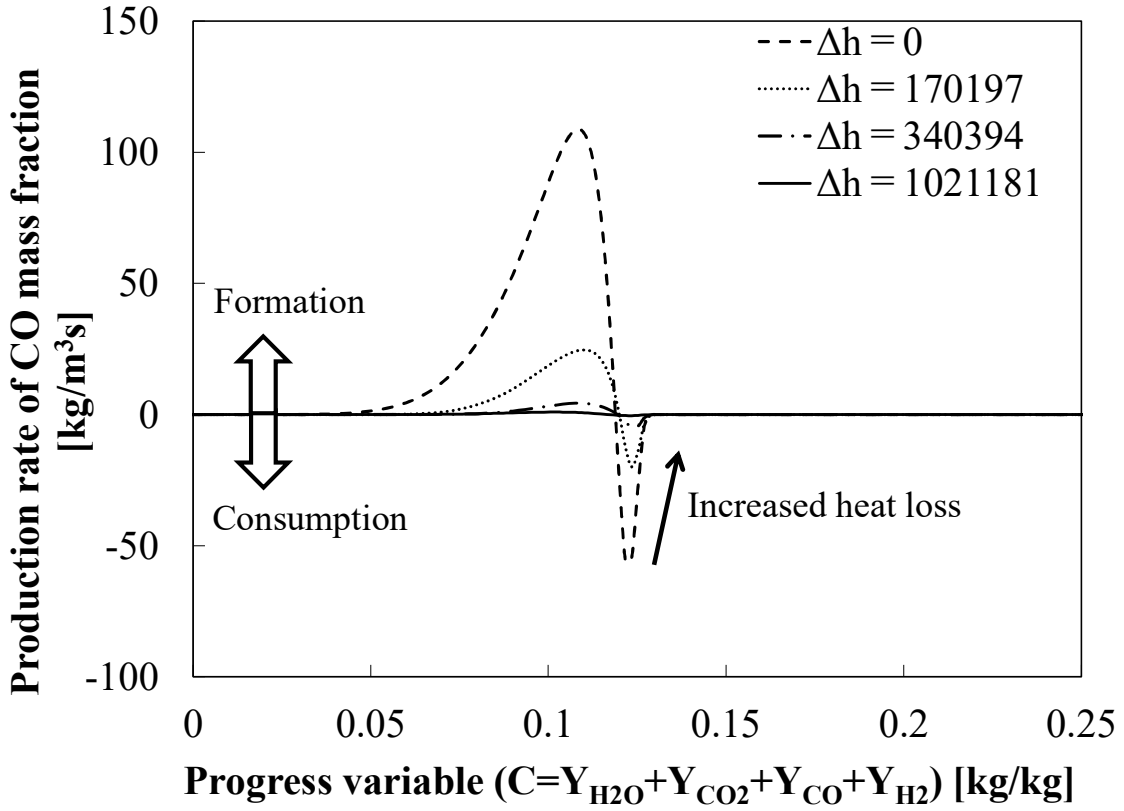

Figure 18 Comparison of production rates of CO mass fraction in the flamelet library for φ = 0.43 between each heat loss $\Delta h(= h_0 - h)$.

3.4 Conclusions

In this study, LES employing an NA-FGM approach, which can consider the effects of heat loss, was applied to the CH_4–air super lean premixed combustion fields generated by an axisymmetric jet burner with a cooled wall under pressurized conditions. The validity of accuracy to predict the CO emissions was examined based on a comparison with the results using the conventional FGM approach and experiments. Moreover, the effects of heat loss and equivalence ratio (φ = 0.43–0.5) on CO emissions were investigated in detail.

It was found that the NA-FGM approach improved the prediction accuracies of not only the flame behavior but also the CO emissions compared to the conventional FGM approach, which inherently neglects the heat loss effect. The tendency of the flame length for the lowest equivalence ratio of φ = 0.43, which corresponds to the blow-off limit, was

well produced despite the difficulty in predicting a minor reaction at the flame holding point near the combustor inlet. The NA-FGM approach captured the trend of CO emissions during the experiments in which the CO emissions increased with a decrease in the equivalence ratio. This success could be achieved by considering the effects of heat loss on chemical reactions involving CO and OH radicals. It was also suggested that the cause of the increase in the CO emissions for low equivalence ratios was not due to the increase in CO production, but because of the slow consumption rate of CO, which kept the CO concentration high downstream.

In conclusion, these results suggested that capturing such a sensitive consumption in the CO consumption rate by heat loss is vital for an accurate prediction of the total CO emissions in developing a cutting-edge low emissions gas turbine combustor at low loads. For the design tool of gas turbine combustors, the LES employing the NA-FGM approach is strongly recommended.

References

[1] T., Koganezawa, K., Miura, T., Saitou, K., Abe, and H., Inoue, “Full scale testing of a cluster nozzle burner for the advanced humid air turbine”, Proceedings of ASME Turbo EXPO 2007, GT2007-27737 (2007).

[2] K., Yunoki, T., Murota, K., Miura, and T., Okazaki, “Numerical simulation of turbulent combustion flows for coaxial jet cluster burner”, Proceedings of ASME Power Conference 2013; POWER2013-98143 (2013).

[3] K., Yunoki, and T., Murota, “Large eddy simulation to predict flame front position for turbulent lean premixed jet flame at high pressure”, Proceedings of ASME Turbo EXPO 2018 GT2018-75601 (2018).

[4] K., Yunoki, T., Murota, T., Asai, and T., Okazaki, “Large eddy simulation of a multiple-injection dry low NOx combustor for hydrogen-rich syngas fuel at high pressure”, Proceedings of ASME Turbo EXPO 2016, GT2016-58119 (2016).

[5] S., Tachibana, K., Saito, T., Yamamoto, M., Makida, T., Kitano and R., Kurose, “Experimental and numerical investigation of thermo-acoustic instability in a liquid-fuel aero-engine combustor at elevated pressure: Validity of large-eddy simulation of spray combustion”, Combustion and Flame; 162: 2621-2637 (2015).

[6] Nishiie T, Makida M, Nakamura N, Kurose R. Large-eddy simulation of turbulent spray combustion field of full annular combustor for aircraft engine, Proc. Int. Gas Turbine Congress 2015 ;785-791 (2015).

[7] K., Hirano, Y., Nonaka, Y., Kinoshita, M., Muto and R., Kurose, "Large-eddy simulation of turbulent combustion in multi combustors for l30a gas turbine engine", Proceedings of ASME Turbo EXPO 2015, GT2015-42545 (2015).

[8] H., Moriai, R., Kurose, H., Watanabe, Y., Yano, F., Akamatsu and S., Komori, "Large-eddy simulation of turbulent spray combustion in a subscale aircraft jet engine combustor - predictions of no and soot concentrations", Journal of Engineering Gas Turbines Power 2013;135: 091503 (2013).

[9] N., Peters, "Laminar flamelet concept in turbulent combustion", Proceedings of Combustion Institute, 21; 21:1231-1250 (1986).

[10] C. D., Pierce, and P., Moin, "Progress-variable approach for large-eddy simulation of non-premixed turbulent combustion", Journal of Fluid Mech.; 504:73-97 (2004).

[11] van Oijen JA, and de Goey LPH., "Modeling of pre-mixed laminar flames using flamelet-generated manifolds", Combustion Science and Technology, 161:113-137 (2000).

[12] A. M., Vreman, B. A., Albrecht, van Oijen JA, de Goey LPH, and RJM., Bastiaans, "Premixed and nonpremixed generated manifolds in large-eddy simulation of Sandia Flame D and F", Combustion and Flame; 153:394-416 (2008).

[13] A., Donini, RJM., Bastiaans, van Oijen JA, and de Goey LPH., "Numerical simulations of a turbulent high-pressure premixed cooled jet flame with the flamelet generated manifolds technique", Journal of Engineering Gas Turbines Power, 137:071501 (2015).

[14] F., Proch, A. M., Kempf, "Modeling heat loss effects in the large eddy simulation of a model gas turbine combustor with premixed flamelet generated manifolds", Proceedings of Combustion Institute, 35;35: 3337-3345 (2015).

[15] A., Kishimoto, H., Moriai, K., Takenaka, T., Nishiie, M., Adachi, A., Ogawara, and R., Kurose, "Application of a non-adiabatic flamelet/progress-variable approach to large eddy simulation of H2/O2 combustion under a pressurized condition", Journal of Heat Transfer, 139:124501 (2017).

[16] K., Yunoki, R., Kai, S., Inoue, and R., Kurose, “Numerical simulation of CO concentration on flame propagation in the vicinity of the wall -Validity of non-adiabatic FGM approach”, International Journal Gas Turbine, Propulsion Power Systems, 11:8-15 (2020).

[17] T., Honzawa, T, R., Kai, A., Okada, A., Valera-Medina, PJ., Bowen, and R., Kurose, “Predictions of NO and CO emissions in ammonia/methane/air combustion by LES using a non-adiabatic flamelet generated manifold”, Energy;186:115771 (2019).

[18] P., Wollny, B., Rogg, A., Kempf, “Modelling heat loss effects in high temperature oxy-fuel flames with an efficient and robust non-premixed flamelet approach”, Fuel, 216:44-52 (2018).

[19] X., Wen, K., Luo, Y., Luo, HI., Kassem, H., Jin, and J., Fan, “Large eddy simulation of a semi-industrial scale coal furnace using non-adiabatic three-stream flamelet/progress variable model”, Applied Energy;183:1086-1097 (2016).

[20] N., Peters, “The turbulent burning velocity for large scale and small scale turbulence”, Journal of Fluid Mech., 384:107-132 (1999).

[21] P., Griebel, E., Boschek, P., Jansohn, “Lean blowout limits and NOx emissions of turbulent, lean premixed, hydrogen-enriched methane/air flames at high pressure”, Proceedings of ASME Turbo Expo 2006, GT2006-90490 (2006).

[22] P., Siewert, P., Griebel, R., Schären, R., Bombach, A., Inauen A, Kreutner W, Schenker S. Turbulence and flame characteristics of premixed methane/air flames at gas turbine relevant conditions; VDI report No. 1750:303-308 (2003).

[23] H., Pitsch, Flamemaster: A c++ computer program for 0d combustion and 1d laminar flame calculations (1998).

[24] B., Serauskas, available at <http://combustion.berkeley.edu/gri-mech/version30/text30.html>.

[25] D. K., Lilly, “A proposed modification of the Germano subgridscale closure method”, Physics and Fluids A; 4: 633-635 (1992).

[26] S. E., Jella, J. M., Bergthorson, P. Q., Gauthier, G., Bourque, “CFD modeling of equivalence ratio effects on a pressurized turbulent premixed flame”, Proceedings of ASME Turbo EXPO 2016, GT2016-58074 (2016).

[27] S., Know, L. K., Tseng, G. M., Faeth, “Laminar burning velocities and transition to

unstable flames in H2/O2/N2 and C3H8/O2/N2 mixtures", Combustion and Flame, 90:230-246(1992).

Nomenclature

C	Progress variable [-]
C_p	Isobaric specific heat [J/kg/K]
D_h	Thermal diffusivity [m^2/s]
D_γ	Diffusion coefficient $\left(D_\gamma = \lambda/\rho C_p\right)$ [m^2/s]
h_k	Enthalpy of species k [J/kg]
j_k	Mass diffusion flux of species k [kg/m^2s]
$\dot{m}_k$	Mass production rate of species k [kg/m^3s]
P	Pressure [Pa]
$\dot{q}_{loss}$	Source term of heat loss [W/m^3]
T	Temperature [K]
u	Velocity vector [m/s]
Y_k	Mass fraction of chemical species k [-]
Z	Mixture fraction [-]

Greeks

α	Adjustment parameter
λ	Thermal conductivity
φ	Equivalence ratio [-]
μ	Viscosity [Pa·s]
ρ	Density [kg/m^3]
τ	Shear stress tensor
$\dot{\omega}_C$	Generation rate of progress variable+
$\dot{\omega}_k$	Chemical reaction rate of chemical species k

Subscripts

f	Fuel
k	Chemical species
st	Stoichiometric air-to-fuel ratio
$wall$	Wall

Chapter 4: Large eddy simulation of partially premixed combustion in an actual gas turbine combustor

4.1 Introduction

Gas turbine power plants are composed of a compressor, combustor, turbine, and generator. A low nitrogen oxide (NOx) combustor is needed to reduce air polluting emissions from industrial gas turbine power plants, and a low NOx combustor named as the “coaxial jet cluster burner” [1-2] was developed for this purpose (as shown in Figure 4.1). This burner has a gas turbine combustor in which multiple fuel nozzles and holes are arranged coaxially. Air and fuel are rapidly mixed in these holes. This rapid mixing within a short distance can reduce NOx emissions by achieving homogeneous lean premixed combustion [2].

For the development of gas turbine combustors, computational fluid dynamics (CFD) is a powerful tool for investigating the detailed distributions of various emissions and temperature [3-7]. Recently, a large eddy simulation (LES) model is used for combustion analysis to analyze the unsteady combustion state in the combustor. LES models an eddy smaller than the cell size and can reproduce a flow with precision if the cell size is sufficiently small. Generally, a long calculation time is required to calculate the unsteady turbulence flow because LES requires unsteady simulation with many cells. However remarkable progress in computer technology has made it possible to simulate actual combustors. LES with the dynamic sub grid scale (SGS) model [8-9] is often used as a numerical analysis method for turbulent flow, including combustion flow [3-7].

Furthermore, carbon monoxide (CO) emissions are an important index for evaluating combustors. If CO is formed, there is a lot of unburned carbon at combustor outlet. Thus, the thermal efficiency decreases. Additionally, the reduction in CO emissions is necessary from the viewpoint of environmental pollution. In a lean premixed combustion, CO is often generated in a combustion chamber at partial loads [10] and when a flame is in contact with air [11]. A turbulent combustion approach that can

reproduce the CO formation is required. Conventionally, the *G*-equation approach [12-13] is used to calculate premixed combustion. However, this approach does not calculate the CO concentration accurately because it calculates the unburned and burned gas compositions in the equilibrium condition.

The purpose of this study is: 1) to validate the hybrid turbulent combustion (HTC) approach by comparing the obtained calculation results with the measured gas temperature and gas concentration distributions obtained using a coaxial jet cluster burner test rig under atmospheric pressure; and 2) to analyze the CO formation mechanism which is an important performance factor for gas turbine combustors.

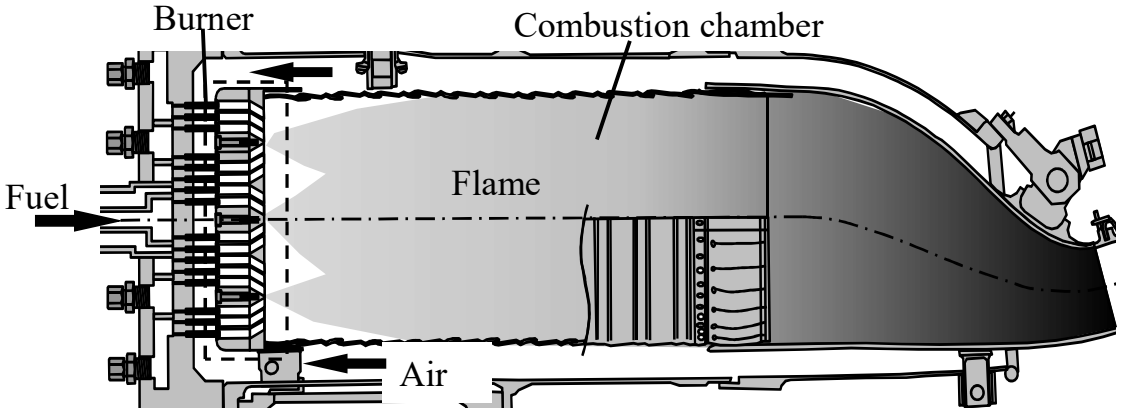

Figure 4.1 Schematic of combustor with cluster burner.

4.2 Numerical methods

In this study, we used the HTC approach [7], which is a combination of a flamelet/progress variable (FPV) approach [7,14-16] and a flame propagation approach [7]. This combined approach can calculate the combustion style or form that the non-premixed combustion coexists with in premixed combustion. In the following, we describe the FPV approach (section 4.2.1), the flame propagation approach (section 4.2.2), and the HTC approach (section 4.2.3).

4.2.1 Flamelet/progress variable (FPV) approach

The FPV approach is generally applied in the case of a non-premixed flame. It needs a database, called a flamelet library, which is obtained by calculation of laminar

flow flame under various conditions. This database provides the filtered quantities of all scalar values as a function of the filtered mixture fraction $\widetilde{Z}$, the mixture fraction sub-filter variance $\widetilde{Z}''^2$, the filtered reaction progress variable $\widetilde{C}$, and the filtered scalar dissipation rate $\widetilde{\chi}$. The governing equation for the mixture fraction and the progress variable can be written as:

$$\frac{\partial \bar{\rho}\tilde{Z}}{\partial t} + \frac{\partial \bar{\rho}\widetilde{u_i}\tilde{Z}}{\partial x_i} = \frac{\partial}{\partial x_i}\bar{\rho}D_{sgs}\left(\frac{\partial \tilde{Z}}{\partial x_i}\right) \tag{1}$$

$$\frac{\partial \bar{\rho}\tilde{C}}{\partial t} + \frac{\partial \bar{\rho}\widetilde{u_j}\tilde{C}}{\partial x_j} = \frac{\partial}{\partial x_j}\bar{\rho}\left(D + D_{sgs}\right)\frac{\partial \tilde{C}}{\partial x_j} + \overline{w_d} \tag{2}$$

where $\bar{\rho}$ s density, $\widetilde{u_i}$ is velocity, D is dissipation rate and D_{sgs} is dissipation rate of sub grid scale. Using the provided $\widetilde{Z}$ and $\widetilde{C}$, we calculated the mass fraction of the chemical species $\widetilde{Y_l}$ in Eq.(3).

$$\widetilde{Y_l} = \int_0^1 Y_l\left(Z,\tilde{C}\right)P\left(Z,\tilde{Z},\widetilde{Z''^2}\right)dZ \tag{3}$$

where $P(Z,\widetilde{Z},\widetilde{Z''^2})$ is a probability density function (PDF). The source term of the progress variable $\overline{w_d}$ can be written as

$$\overline{w_d} = \int_0^1 w_d\left(Z,\tilde{C}\right)P\left(Z,\tilde{Z},\widetilde{Z''^2}\right)dZ \tag{4}$$

4.2.2 Flame propagation approach

A flame propagation approach is applied in the case of premixed flame. This approach considers the flame stretch effect [17], the diffusion enhancement effect [18], and the increasing rate of the flame surface area. Here this approach can be applied to a thin reaction zone regime, a corrugated flamelet regime, and a wrinkled flamelet regime [19] in the flame forms of the turbulence premixed flame. The governing equation for the mass fraction of burned gas $\widetilde{G}$ can be written as:

$$\frac{\partial \bar{\rho}\tilde{G}}{\partial t} + \frac{\partial \bar{\rho}\widetilde{u_j}\tilde{G}}{\partial x_j} = \frac{\partial}{\partial x_j}\bar{\rho}\left(D + D_{sgs}\right)\frac{\partial \tilde{G}}{\partial x_j} + \overline{w_G} \tag{5}$$

The source term of the mass fraction of burned gas $\overline{w_G}$ can be written as:

$$\overline{w_G} = \rho_u I J \Xi \bar{\Sigma} S_L^0 \tag{6}$$

where S_L^0 is laminar burning velocity. These are given by the following equations

$$J = \left(1 + \frac{Pr}{Pr_t}\left(\frac{C_s c_\delta \delta_L^0}{\eta_i}\right)^{4/3} J^{4/3}\right)^{1/2} \tag{7}$$

$$I = \frac{1}{1 + Ma^* Ka^*} \tag{8}$$

$$\Xi = \left(\frac{\Delta}{l_{ic}}\right)^{D_F - 2} \tag{9}$$

$$\bar{\Sigma} = \frac{\bar{A}}{V} \tag{10}$$

where J is the diffusion enhancement effect of the preheated regime due to the turbulence flow vortex, I is the flame stretch effect [17], Ξ is the increasing rate of the flame surface area, $\overline{\Sigma}$ is the flame area density in the calculation cell. Ma^* is the Markstein number, and Ka^* is the Kalrovitz number.

4.2.3 Hybrid turbulent combustion (HTC) approach

The HTC approach uses both a FPV approach and a flame propagation approach. Eq. (11) relates the progress variable $\widetilde{C}$ and the mass fraction of burned gas $\widetilde{G}$.

$$\tilde{G} = \frac{\tilde{C} - \widetilde{C_u}}{\widetilde{C_b} - \widetilde{C_u}} \tag{11}$$

Substituting Eq. (11) into Eq. (5) gives us

$$\frac{\partial \bar{\rho}\tilde{C}}{\partial t} + \frac{\partial \bar{\rho}\widetilde{u_j}\tilde{C}}{\partial x_j} = \frac{\partial}{\partial x_j}\bar{\rho}\left(D + D_{sgs}\right)\frac{\partial \tilde{C}}{\partial x_j} + \overline{w_p} \tag{12}$$

$$\overline{w_p} = \left(\widetilde{C_b} - \widetilde{C_u}\right)\overline{w_G} \tag{13}$$

Eq. (12) is the governing equation for premixed combustion based on the progress variable $\widetilde{C}$. The only difference between Eqs. (2) and (12) is the source term of the progress variable. Therefore, the governing equation for the progress variable in the HTC approach can be written as:

$$\frac{\partial \bar{\rho}\tilde{C}}{\partial t} + \frac{\partial \bar{\rho}\widetilde{u_j}\tilde{C}}{\partial x_j} = \frac{\partial}{\partial x_j}\bar{\rho}\left(D + D_{sgs}\right)\frac{\partial \tilde{C}}{\partial x_j} + \left[f\overline{w_p} + (1-f)\overline{w_d}\right] \tag{14}$$

The source term of the HTC approach $\overline{w}_C$ is calculated by a linear combination of the source term of the progress variable $\overline{w}_d$ and the mass fraction of burned gas $\overline{w}_p$ by the weighting factor f for the source term:

$$f = max\left(0, min\left(1, \frac{1}{2}\frac{\lceil\nabla\tilde{G}\rceil}{\lceil\nabla\tilde{Z}+\varepsilon\rceil} - 1\right)\right) \tag{15}$$

4.2.4 CO transport approach

In this study, the method which directly calculated from flamelet library as shown Eq. (3) is defined as "database approach". On the other hand, "transport approach" is calculated by CO transport equation. The transport approach is considered to be effective for an object in which reactions of minor components (CO, NO, etc.) are quenched and transported like a gas turbine combustor, to transport and calculate chemical species composition individually. In this study, a method to solve the transport equation of CO mass fraction expressed by Eq. (16) [15] was adopted. Eq. (17) shows the generation term of the transport equation of the CO mass fraction.

$$\frac{\partial\bar{\rho}\widetilde{Y}_\iota}{\partial t} + \frac{\partial\bar{\rho}\widetilde{u}_j\widetilde{Y}_\iota}{\partial x_j} = \frac{\partial}{\partial x_j}\left(\frac{\mu}{Pr} + \frac{\mu_{sgs}}{Pr_{sgs}}\right)\frac{\partial\widetilde{Y}_\iota}{\partial x_j} + \bar{\rho}\widetilde{w_\iota} \tag{16}$$

$$\widetilde{w_\iota} = \widetilde{w_\iota}^{+} + \frac{\widetilde{Y}_\iota}{\widetilde{Y}_\iota^{FPV}}\widetilde{w_\iota}^{-} \tag{17}$$

where subscript i indicates the chemical species, which in this study represents CO. $\widetilde{w}_i$ [kg/m^3/s] is the source term of mass fraction of the chemical species i, $\widetilde{w}_i^{+}$ [kg/m^3/s] is the generation rate of the chemical species i, $\widetilde{w}_i^{-}$ [kg/m^3/s] is the reverse rate of the chemical species i, $\widetilde{Y}_i$ [kg/kg] is the mass fraction of the chemical species i, $\widetilde{Y}_i^{FPV}$ [kg/kg] is the mass fraction of the chemical species i based on FPV approach, μ_{sgs} [Pa・s] is viscosity of SGS model. Pr_{sgs} [-] is Prandtl number of SGS model, which is set set to the internally validated constant value of 0.42.

The calculation procedure of the CO transport approach is explained. By the one-dimensional elementary reaction calculation of laminar diffusion flame, the generation rate and the reverse rate of CO are calculated beforehand and added to the flamelet library. Next, the mixture fraction and the progress variable are calculated by three- dimensional numerical simulation. Finally, the source term of CO is extracted from flamelet library using the mixture fraction and the progress variable calculated by the transport equation. The CO mass fraction is obtained using the transport equation with Eqs. (16) and (17).

4.2.5 Calculation setup

4.2.5.1 Structure of coaxial jet cluster burner

The coaxial jet cluster burner consists of a perforated plate with multiple air holes and multiple fuel nozzles arranged coaxially. Figure 4.2 shows a perforated plate of a multi-cluster combustor with multiple cluster burners developed for an actual gas turbine combustor. Figure 4.3 shows a schematic view of a perforated plate and a fuel nozzle. The air holes are arranged in three circles: six holes are arranged on the first circle (with the smallest diameter), 12 holes on the second circle (with the middle diameter), and 18 holes on the third circle (with the largest diameter). The region within the first circle on the perforated plate is called the “inner region” and the region without the first circle is called the “outer region.”

Fuel emanates from the fuel nozzles through the air holes into the combustion chamber. The fuel through the six air holes on the first circle is referred to as “inner fuel” and the fuel injected through the 30 air holes on the second and third circles is referred to as “outer fuel.” The distributions of the inner fuel and the outer fuel affect the combustion efficiency of the burner. The air holes are inclined for the purpose of forming a swirling flow by the combustion air. The central axis of each hole is inclined in the direction of a tangent to each of the circles.

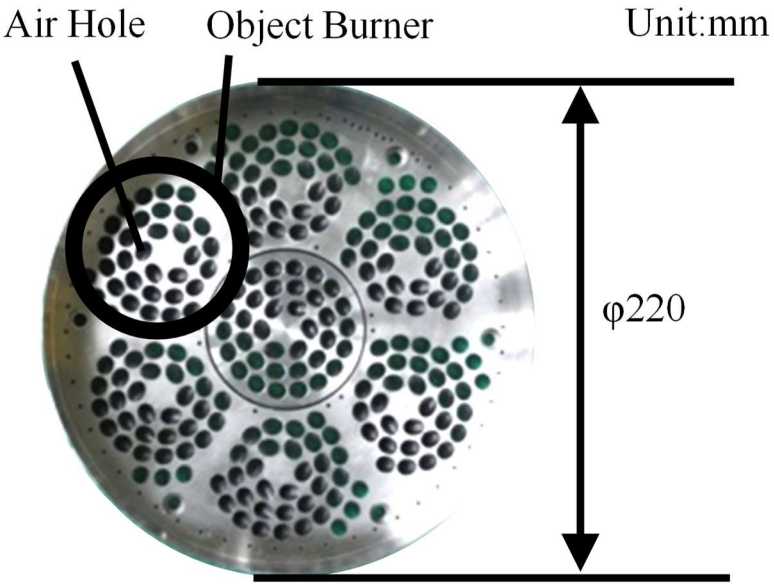

Figure 4.2 Schematic of perforated plate for multi cluster combustor.

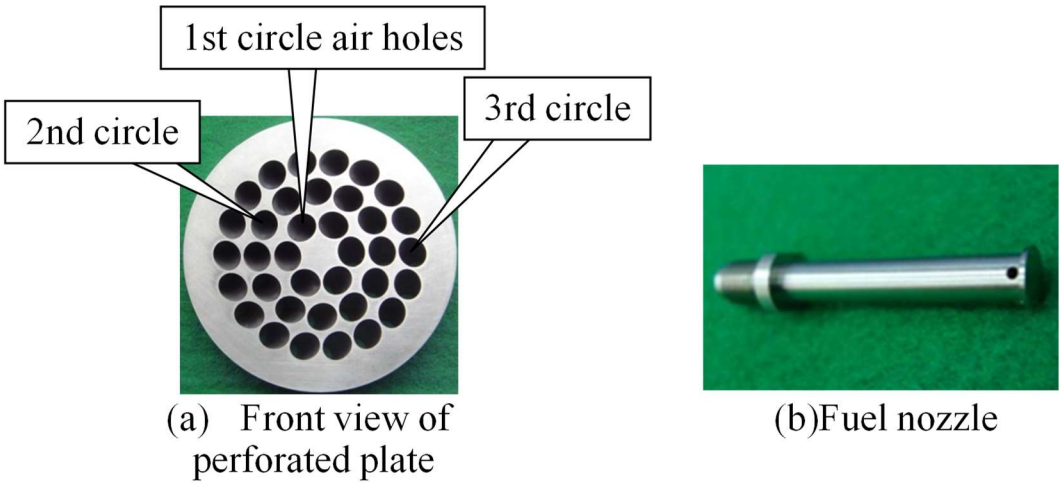

Figure 4.3 Schematic of a perforated plate and a fuel nozzle for the main burner.

4.2.5.2 Structure of combustion test rig

The experiments were conducted at atmospheric pressure in a combustion test rig of a model gas turbine combustor [1]. Figure 4.4 shows a schematic diagram of the combustion test rig. The main components of the rig are a combustor, air and fuel supply systems, and measurement equipment.

The combustor consisted of a combustion liner and the coaxial jet cluster burner. The combustion liner was equipped with film cooling air holes and liner lips on the

surface and it included a cylindrical combustion chamber inside. The diameter of the combustion chamber was 120mm. The fuel reacted with the combustion air, and then a flame was formed in the combustion chamber. The burned gas was discharged into the atmosphere after its temperature had been lowered in the temperature reducer.

Figure 4.5 shows the burner cooling position assembly. The air supply system supplied combustion air and cooling air separately to the combustor from a compressor through a heater. The combustion air was used as an oxidant in the combustion. The cooling air entered the combustion chamber through the liner. The cooling air cooled the liner by impinging on its outer surface and flowed along its inner surface. A large cooling air flow was used for the purpose of protecting the combustion chamber.

The fuel supply system supplied CH_4. The fuel supply was separated as the inner fuel and the outer fuel. The inner fuel was supplied to the six fuel nozzles on the first circle of the perforated plate and the outer fuel was supplied to the 30 fuel nozzles on the second and third circles.

The measurement equipment consisted of a sampling probe, gas analyzer (Horiba, Ltd., Model VIA-510), and thermocouple. The gas analyzer measured the concentrations of CO, O_2, CO_2, and total hydrocarbons (THCs) contained in the combustion gas. The measurements were carried out at various distances from the burner: from 30 mm to 200 mm in the axial direction and from 0mm to 40mm in the radial direction.

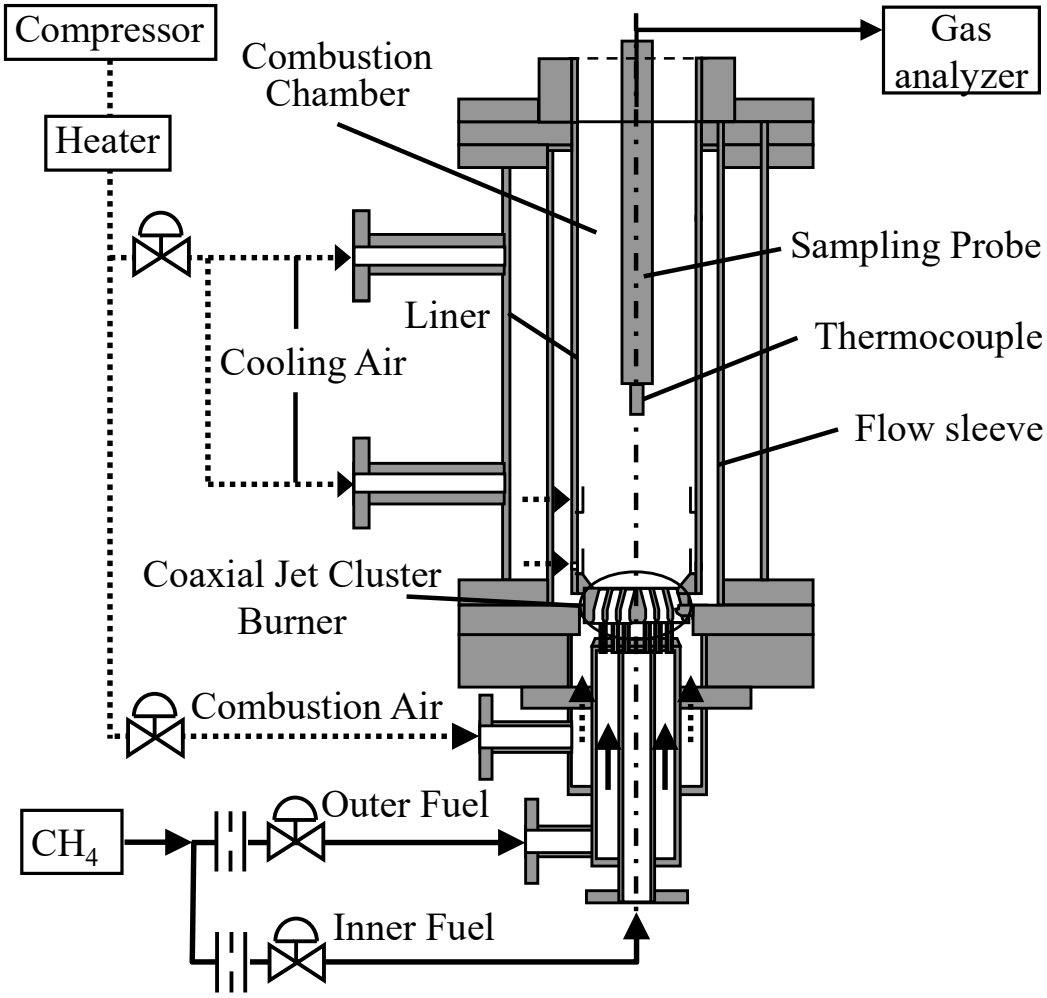

Figure 4.4 Schematic diagram of combustion test rig.

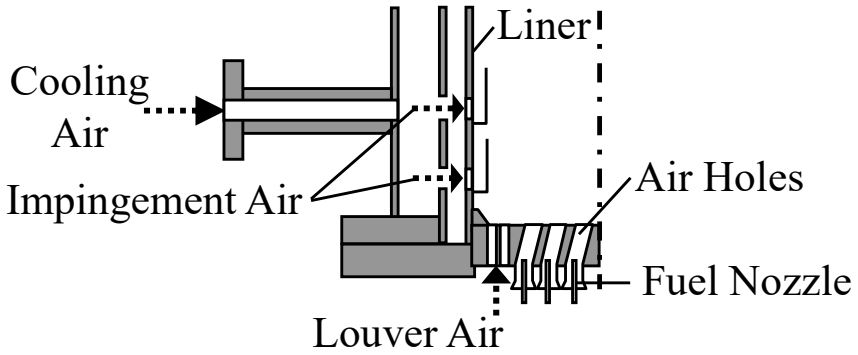

Figure 4.5 Schematic of burner cooling position assembly.

4.2.5.3 Experimental conditions

The experiments were conducted under the test conditions listed in Table 1. The combustion air flow rate was 190m^3N/h. Normal temperature and pressure were 273.15K and 0.1013MPa, respectively. The combustion air temperature was 623K. The pressure in the chamber was atmospheric pressure. The fuel/air ratio (F/A) of the burner was 0.0314. F/A is a ratio of mass flow rate of fuel and combustion air as oxidizer.

Table 4.1 Test conditions

	Unit	Comb. air	Cooling air	Fuel(CH_4)
Temperature	[K]	623	623	298
Flow Rate	[kg/s]	0.0682	0.0212	0.00215
Outlet Pressure	[MPa]		0.101	
Burner F/A	[-]		0.0314	

4.2.5.3 Calculation conditions

Figure 4.6 shows a schematic diagram of the computational domain. The computational region was divided into about 4.8 million cells. In order to secure the calculation accuracy, the minimum size of 1 side of the grid size was made to be about 0.1 mm near the fuel nozzle and about 0.2 mm inside the air hole, and the continuous structure hexamesh was adopted. It took about 128 CPU × 336 hours to calculate combustion behavior for 0.10s using a PC cluster (AMD Opteron 6140). This is about three times of the time (0.03 seconds) until the fuel spouted from the fuel nozzle hole and passed through the outlet. By this degree of calculation, the effect of the initial value is eliminated, and the time average field can be calculated. Time averaging was done for the last 0.03s after the influence of the initial conditions disappeared.

Turbulent flow was simulated using the LES with a dynamic SGS model (LISEA4) [8]. These models were programmed on OpenFOAM [20].

The FPV approach needed a flamelet library. It was generated by the calculation of a one-dimensional laminar counterflow non-premixed flame. The flame propagation approach needed laminar burning velocity data. These data were calculated by the

detailed elementary reaction calculation with the FlameMaster code [21]. The detailed reaction mechanism adopted GRI-mech 3.0[22].

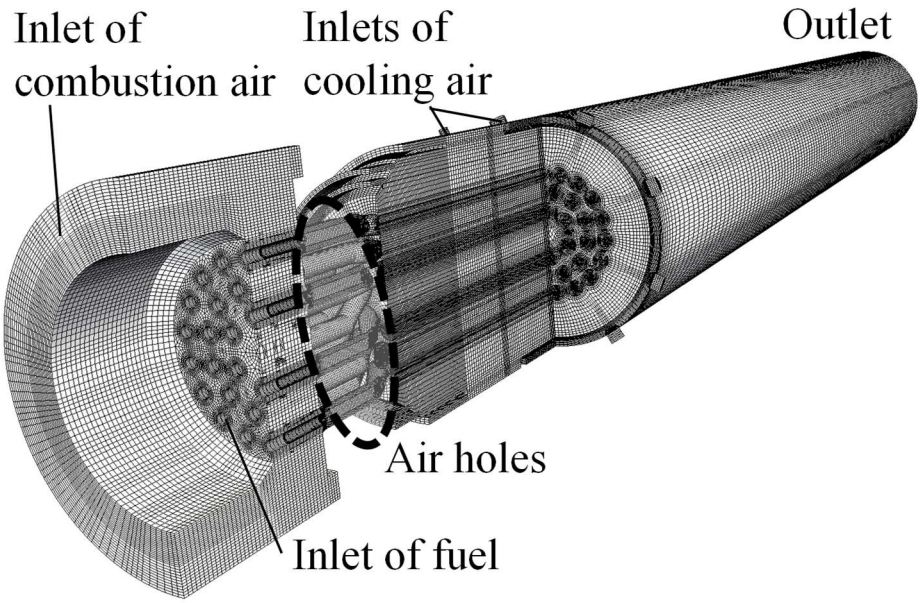

Figure 4.6 Schematic diagram of computational domain.

4.3 Results and discussions

We describe the analysis results show the combustion stability of the coaxial jet cluster burner (Section 4.3.1), the validation results on the predictive precision of the HTC approach by comparison between experimental and calculation results (Section 4.3.2), the flame configuration of the coaxial jet cluster burner(Section 4.3.3), the validation results of the distribution of CO for the coaxial jet cluster burner (Section 4.3.4), the CO formation factors in coaxial jet cluster burner(Section 4.3.5).

4.3.1 Combustion stability of coaxial jet cluster burner

Figures 4.7 to 4.9 show the instantaneous contours of the axial velocity distribution in the combustion chamber, the instantaneous contours of the temperature distribution and the time averaged, and the instantaneous contours of the fuel mass fraction. A line in figure 4.7 indicates a position where the axial velocity becomes zero. The temperature was normalized by equation (18). The line in figure 4.8 is a position

where the normalized temperature $T_{dimensionless}$ = 0.9. In the following, the range over normalized temperature $T_{dimensionless}$ = 0.9 is called a high temperature field.

$$T_{dimensionless} = \frac{T - T_{min}}{T_{max} - T_{min}} \tag{18}$$

As shown in figures 4.7 (a) and 4.7 (b), a recirculation flow of about 70 mm in the axial direction was formed in the center of the combustion chamber and a recirculation flow of about 40 mm in the outer of the combustion chamber. The recirculation flow shown in figure 4.7 (a) is included in the high temperature field in the center of the combustion chamber shown in figure 4.8 (c). According to the time-averaged temperature distribution, the center of the combustion chamber forms a uniform high-temperature field as shown in figure 4.8 (d). This means that fuel and combustion air are mixed at uniform F/A. In addition, as shown in figure 4.8 (e), a sharp temperature gradient is generated at the outer of the combustion chamber and forming a conical high-temperature field.

According to the fuel mass fraction distribution as shown in figure 4.9 (f), the fuel mass fraction is high at the outer periphery of the conical high-temperature field, and unburnt fuel components exist near the burner. However, the fuel mass fraction decreases downstream of the combustion chamber shown in figure 4.9 (g). This is because unburned fuel is supplied to the center of the combustion chamber together with high temperature burned gas by the recirculation flow region shown in figure 4.7 (a). As the results, it was proven that coaxial jet cluster burner maintains the flame stability due to return the unburned fuel and high temperature heat source by the recirculation flow in the combustion chamber center. Therefore, we thought the burner had high flame stability.

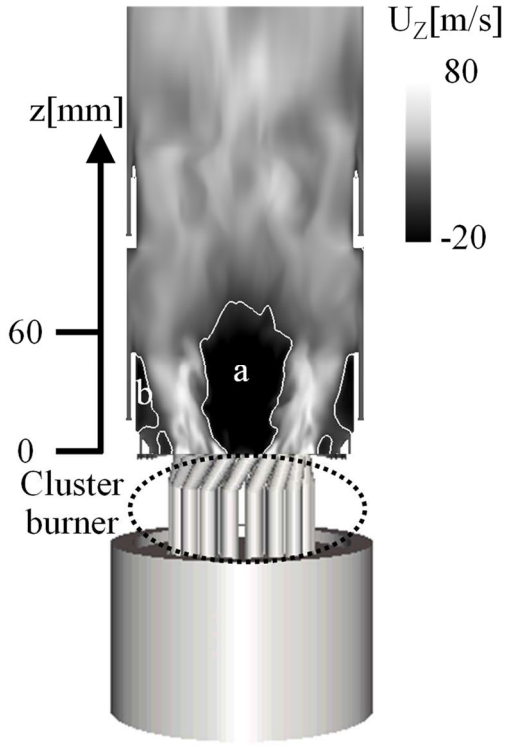

Figure 4.7 Calculation result for axial velocity (instantaneous).

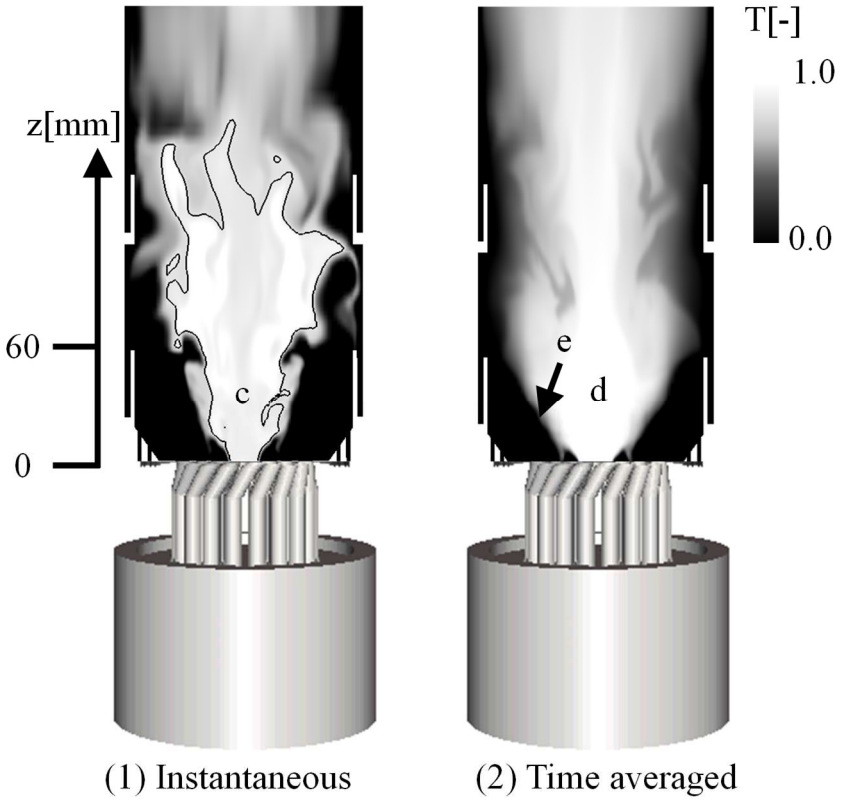

Figure 4.8 Calculation results for temperature distributions.

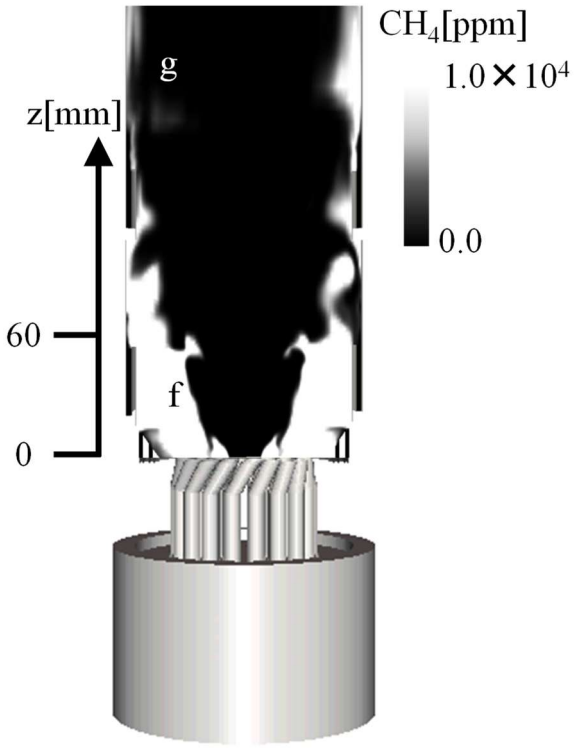

Figure 4.9 Calculation result for CH_4 concentration (instantaneous).

4.3.2 Validation of HTC approach

In this section, the calculation results are compared with the experimental results in order to validate the HTC approach. Figures 4.10, 4.11 and 4.12 respectively show the validation results of gas temperature and O_2 and CH_4 volume fractions along the radial line (z=60mm). These results were time-averaged quantities to compare with experimental results.

The calculated gas temperatures showed good agreement with experimental data. The simulation tool was able to predict the tendency that temperature decreased from the internal side to the outer side of the combustion chamber. Also, it predicted the tendency that temperature was uniform from the central position to the radius position 20mm. The calculated O_2 and CH_4 volume fractions also showed good agreement with experimental data. The HTC approach predicted the position of the oxidation reaction in fuel (r=20mm). The flame shape of this burner could be reproduced by our simulation tool. This is because the LES predicted the recirculation flow in the center of the combustion chamber and the HTC approach predicted the oxidation reaction rate of the fuel with good accuracy.

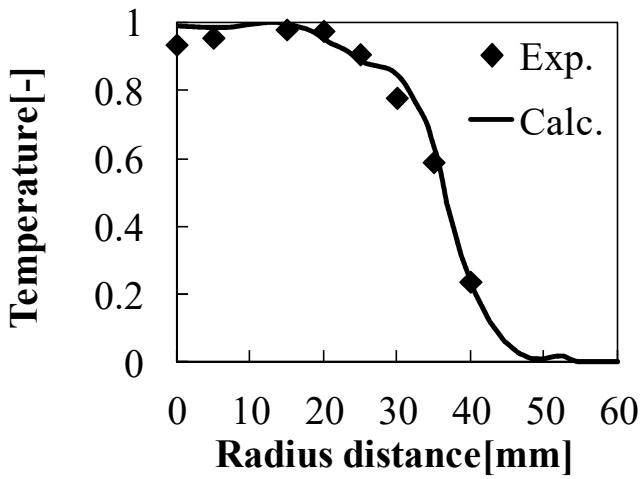

Figure 4.10 Validation results for temperature along z=60mm (time average).

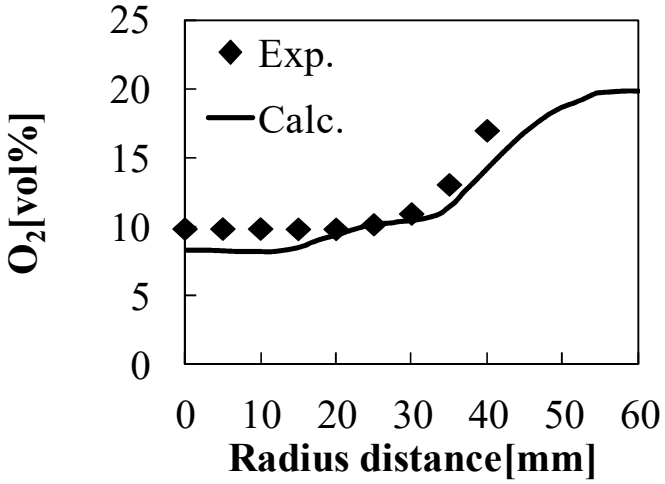

Figure 4.11 Validation results for O_2 volume fraction along z=60mm (time average).

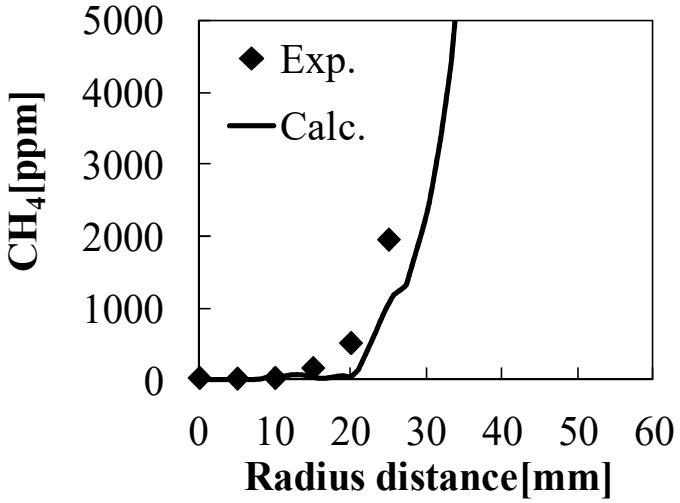

Figure 4.12 Validation results for CH_4 volume fraction along z=60mm (time average).

4.3.3 Prediction of flame configuration

In this section, the flame configuration of the coaxial jet cluster burner is clarified by the weighting factor f used in the HTC approach to discriminate non-premixed combustion from premixed combustion.

Figures 4.13 to 4.15 show the instantaneous distributions of the progress variable, the source term of premixed combustion $f\overline{w_p}$, and the source term of non-premixed combustion $(1-f)\overline{w_d}$. These source terms are synonymous with the reaction rate in the combustion chamber. In the combustor, when the source term of premixed combustion $f\overline{w_p}$ is obtained, the flame configuration is premixed combustion, and when the source term of non-premixed combustion $(1-f)\overline{w_d}$ is obtained, the flame configuration is non-premixed combustion.

As shown in figure 4.13 (h), the boundary between unburned and burned fuel can be distinguished by the distribution of the progress variable. According to figure 4.14 (i), the reaction is actively occurring as premixed combustion near this boundary. On the other hand, as shown in figure 4.15 (j), hardly any reaction as non-premixed combustion occurs at this position.

The weighting factor parameter was judged to be premixed combustion inside the contour of the production rate. The HTC approach verified that the type of combustion of the coaxial jet cluster burner was premixed combustion in spite of the short mixing

distance. The HTC approach was able to reproduce the flame configuration in the combustion chamber. This was because the LES had high predictive precision for the recirculation flow, so the HTC approach had high predictive precision for the reaction rate.

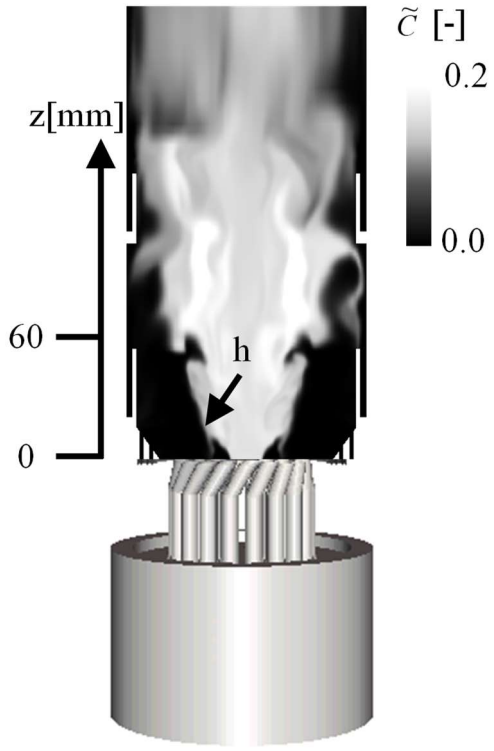

Figure 4.13 Calculation result for the progress variable (instantaneous).

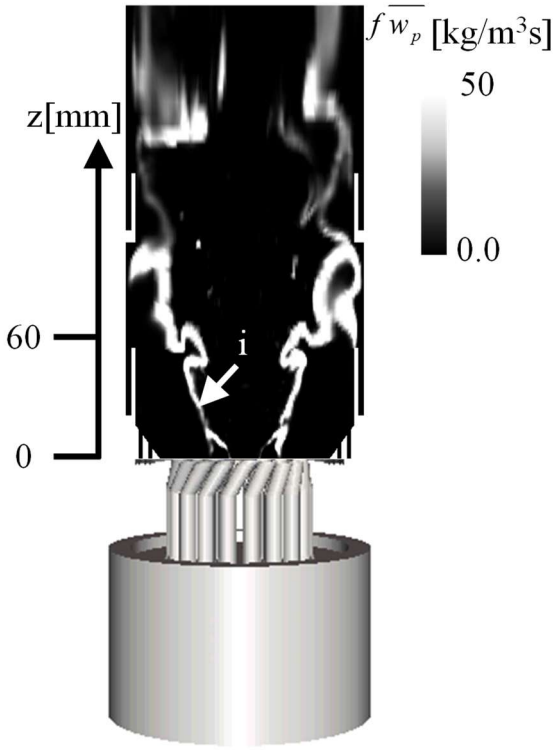

Figure 4.14 Calculation result for the source term of premixed combustion (instantaneous).

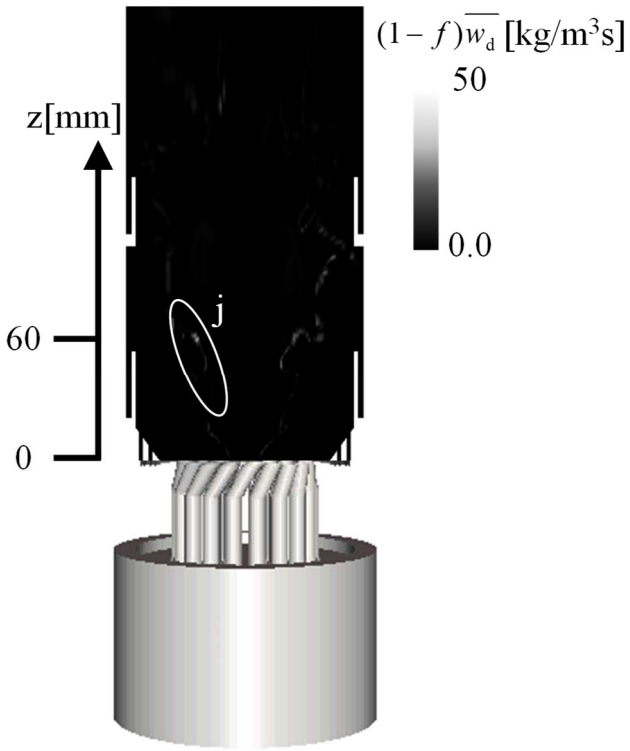

Figure 4.15 Calculation result for the source term of diffusion combustion (instantaneous).

4.3.4 Validation of CO transport approach

In this section, the distribution of the CO volume fraction is compared between experimental and calculation results to validate the transport approach. Figures 4.16 and 4.17 show the validation results for CO volume fraction along z=60mm and 90mm. These results were time-averaged quantities to compare with experimental results. Experimental results are shown by dots, the calculation results using a transport approach are shown by solid lines, and the calculation results using a database approach for obtaining CO volume fraction directly from flamelet library are shown by dotted lines. The radial position r = 0 mm in the figure represents the center of the combustion chamber. In this study, the unstable solution used in the FPV approach incorporated in the HTC approach enables the prediction of the phenomenon in which CO is generated in the middle of the oxidation reaction of fuel.

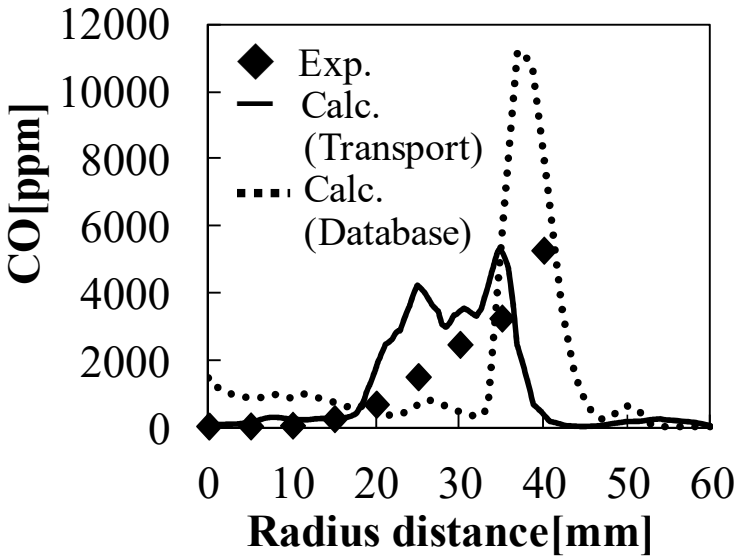

Figure 4.16 Validation results for CO concentration along z=60mm (Time average).

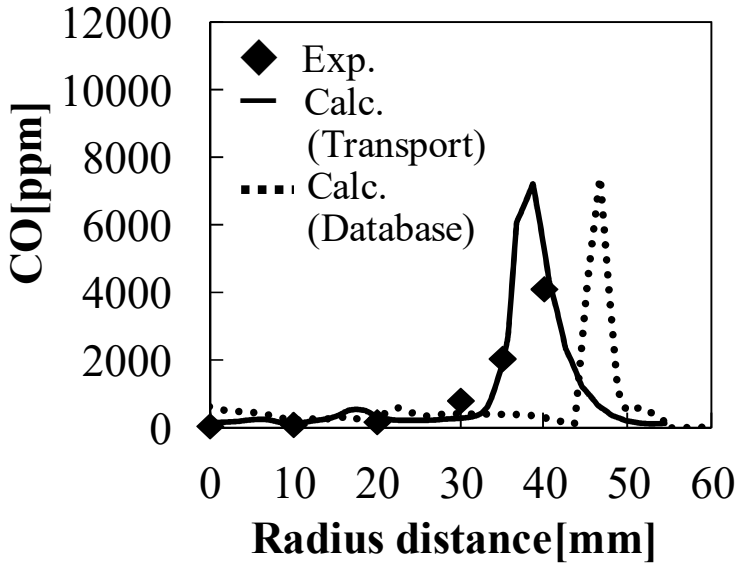

Figure 4.17 Validation results for CO concentration
along z=90mm (Time average).

At 60 mm from the burner edge, the database approach is more than 1000 ppm at the radial position r = 0 mm to 15 mm, which is higher than the result calculated by the transport approach (about 100 ppm). Experimental results are about 24 ppm, and prediction accuracy is higher in the transport approach than in the database approach. In the radial direction from the center of combustion chamber to the wall surface, the position where the CO volume fraction becomes high over 500 ppm is compared. In the experimental result, CO volume fraction increases at r = 20 mm. In contrast, CO volume fraction increased at r = 18 mm for the transport approach and at r = 32 mm for the database approach. The transport approach well reproduced the experimental results. At 90 mm from the burner edge, there are no difference between the experimental and calculation results both approaches from r = 0 to 30 mm. However, the position of high concentration (over 500 ppm) in the radial direction from the center of the combustion chamber to the wall surface was r = 33 mm in the transport approach and r = 43 mm in the database approach for r = 20 mm in the experimental results. In the downstream, the calculation result using the transport approach well reproduced the CO formation position. This is because, as described in section 4.3.2 and 4.3.3, the flame shape can be accurately predicted by the LES and HTC approaches, and the reaction rate of CO used in the transport approach can be accurately predicted by extracting from the flamelet library. From the above fact, the transport approach can predict the CO formation position.

4.3.5 CO formation factors in coaxial jet cluster burner

Figure 4.18 shows the instantaneous contours of CO volume fraction. The center of combustion in figure 4.18 (k), CO is not generated due to the complete combustion of fuel. CO was mainly generated around the outer periphery of the combustion chamber as shown in figures 4.18 (l), (m) and (n). In the inner periphery of the combustion chamber shown in figure 4.18(l) near the burner, the oxidation reaction of fuel was active, and CO, an intermediate product, was generated, resulting in a high concentration. This is the formation factor of CO in the combustion chamber upstream. This can be analyzed by reproducing CO generated in the upstream flame zone by the transport approach.

At the outer periphery of the combustion chamber shown in figure 4.18 (m) near the burner, CO flowed from the downstream of the combustion chamber to the position shown in figure 4.18 (m) by the recirculation flow as shown in figure 4.7 (b), resulting in a high concentration field of about 5000 ppm. In addition, in the vicinity of the wall downstream of the combustion chamber shown in figure 4.18 (n), a high concentration field of more than 5000 ppm was obtained. In this combustion test equipment, a large amount of cooling air is charged from the vicinity of wall surface in comparison with an actual combustor in order to protect the equipment main body for the convenience of safety. Here, the point downstream of the combustion chamber shown in figure 4.18 (o) where the temperature is low (993 K) due to the influence of the cooling air is focused on. At this point, the time scale of the reaction rate calculated from the equation of CO oxidation reaction rate [23] is 0.0428 seconds. This time is longer than the residence time (about 0.03 seconds) in the actual gas turbine combustor. Therefore, CO was not oxidized and discharged to the downstream of the combustion chamber in spite of the high oxygen concentration over 20% at this area. This decrease in temperature by the cooling air is a generating factor of CO in the downstream of the combustion chamber. The reason why such analysis was possible was that the phenomenon in which the oxidation reaction of CO quenched when low temperature air and combustion gas in the middle of reaction were mixed was able to be reproduced by using the transport approach. From the above fact, it was possible to evaluate the formation mechanism of CO in upstream and downstream of combustion chamber by using HTC approach and the transport approach jointly.

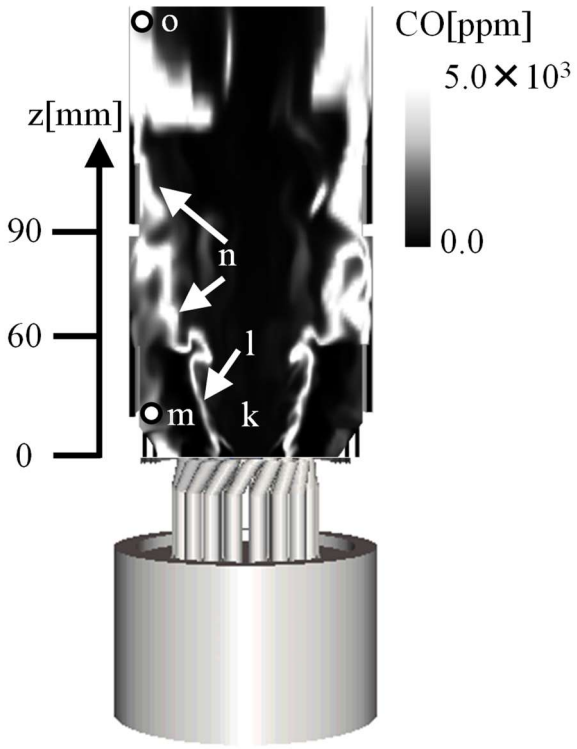

Figure 4.18 Calculation result for CO concentration (instantaneous).

4.4 Conclusions

In this study, numerical simulations of coaxial jet cluster burners for gas turbine combustors were performed, the prediction accuracy of the CO formation position was verified, and the CO formation mechanism was clarified. LES was adopted for the turbulence model, and the HTC approach, which can seamlessly analyze from non-premixed combustion to premixed combustion, developed was adopted for the turbulent combustion approach.

It was confirmed that the HTC approach can predict the CO volume fraction distribution in a lean premixed combustion field. It was clarified that the formation factor of CO was the oxidation reaction of fuel in the upstream of the combustion chamber and the quenching of the CO oxidation reaction by the temperature reduction caused by the effect of cooling air in the downstream of the combustion chamber. The high-temperature field in the center of the combustion chamber and the steep position of the temperature gradient obtained in the combustion experiments were reproduced by numerical

simulations. It was clarified that the mixing performance of the coaxial jet cluster burner was good despite the short mixing distance of fuel and combustion air, and the flame configuration of this burner was a lean premixed combustion by the weighting factor in the HTC approach.

References

[1] T., Asai, S., Dodo, H., Koizumi, H., Takahashi, S., Yoshida, and H., Inoue, “Effects of Multiple-injection-burner Configurations on Combustion Characteristics for Dry Low-NOx Combustion of Hydrogen-rich Fuels” Proceedings of ASME Turbo Expo 2011, GT2011-45295 (2011).

[2] K., Miura, S., Dodo, K., Koyama, and S., Yoshida, “Development of Elemental Technologies of Gas Turbine Combustor for LNG” Proceedings of GTSJ, GTSJ A-18 (2009).

[3] T., Murota, and M., Ohtsuka, “Large-Eddy Simulations of Combustion Oscillation in Premixed Combustor”, Proceedings of ASME Turbo EXPO 1999, ASME 99-GT-274 (1999).

[4] S., Menon, and W.-H., Jou, “Large-Eddy Simulations of Combustion Instability in an Axisymmetric Ramjet Combustor”, Combustion, Science and Technology, 75, pp.53-72 (1991).

[5] S., Menon, and S., Pannala, “Subgrid Two-Phase Mixing and Combustion Modeling”, Proceedings of ASME Turbo EXPO 1998 (1998).

[6] R., Rydén, L.-E., Eriksson, and S., Olovsson, “Large Eddy Simulation of Bluff Body Stabilized Turbulent Premixed Flames”, Proceedings of ASME Turbo EXPO 1993 (1993).

[7] T., Murota, and K., Yamamoto, “Hybrid Turbulent Combustion Model for All of Diffusion, Premixed and Partially Premixed Flames”, 47th Symposium (Japanese) on Combustion. (2009).

[8] T., Murota, “A Dynamic Subgrid Scale Model of Eddy Viscosity Type Deduced from a Local Inter-Scale Equilibrium Assumption of Energy Transfer”, Third International Symposium on Turbulence and Shear Flow Phenomena (2003).

[9] M., Germano, U., Piomelli, P., Moin, and W. H., Cabot, “A Dynamic Subgrid-scale

Eddy Viscosity Model", Physics and Fluids A 3, pp. 1760-1765 (1991).

[10] T., Koganezawa, K., Miura, T., Saitou, K., Abe, and H., Inoue, "Full Scale Testing of a Cluster Nozzle Burner for the Advanced Humid Air Turbine" Proceedings of ASME Turbo Expo 2007, GT2007-27737 (2007).

[11] G., Cabot, D., Vauchelles, B., Taupin, and A., Boukhalfa, "Experimental study of lean premixed turbulent combustion in a scale gas turbine chamber" Experimental Thermal and Fluid Science, 28 pp.683–690 (2004).

[12] F. A., Willams, *The Mathematics of Combustion*, SIAM, pp.99-131 (1985).

[13] F. A., Sethian, "Level Set Methods, Cambridge Monographs on Applied and Computational Mathematics", Cambridge University Press, Cambridge, U.K. (1996).

[14] H., Pitsch, and M., Ihme, "An Unsteady /Flamelet Progress Variable method for LES of Nonpremixed Turbulent Combustion", AIAA Paper 2004-557 (2004).

[15] M., Ihme, and H., Pitsch, "Numerical Prediction of Nitrogen Oxide Emission Using Flamelet/Progress Variable Model", ASP-DFD 2005 (2005).

[16] C., Pierce and P., Moin, "Progress-variable approach for large eddy simulation of turbulent combustion", Report No. TF-80, Stanford University.

[17] S., Know, L. K., Tseng, and G. M., Faeth, "Laminar Burning Velocities and Transition to Unstable Flames in H2/O2/N2 and C3H8/O2/N2 Mixtures", Combustion and Flame, 90, pp.230-246 (1992).

[18] W. L., Kim, and S., Menon, "Large-Eddy Simulation of Turbulent Premixed Flames in the Thin Reaction Zone Regime", AIAA Paper 99-2816 (1999).

[19] N., Peters, "Laminar Flamelet Concepts in Turbulent Combustion", Twenty-first Symposium (International) on Combustion, pp.1231-1250 (1986).

[20] OpenCFD Ltd., available at http://www.opencfd.co.uk/openfoam/.

[21] H., Pitsch, R., Seiser, and B., Varatharajan, "A Guide to FlameMaster".

[22] GRI-Mech Home Page available at http://www.me.berkeley.edu/gri-mech/

[23] F. L., Dryer, and I. Glassman, "High-temperature Oxidation of CO and CH_4", Proceedings of the 14th International Symposium on Combustion, The Combustion Institute, Pittsburg, p. 987 (1973).

Nomenclature

A	Calculated cell area [m^2]
C	Progress variable [-]
C_s	Smagorinsky model parameter [-]
D	Thermal diffusivity [m^2/s]
D_F	Fractal dimension [-]
f	Weighting factor parameter of flame configuration [-]
G	Progress variable [-]
I	Flame stretch effect [-]
J	Diffusion enhancement effect [-]
Ka*	Kalrovitz number [-]
Ma*	Markstein number [-]
Pr	Prandtl number [-]
Prt	Turbulent Prandtl number [-]
$S_L{}^0$	Laminar burning velocity [m/s]
T	Temperature [K]
u	Velocity vector [m/s]
V	Volume of control volume [m^3]
Z	Mixture fraction [-]
c_δ	Model parameter of flame thickness [-]
l_{ic}	Inner cutoff scale [m]
w_d	Production rate of non-premixed combustion [$kg/m^3/s$]
w_G	Production rate of progress variable [$kg/m^3/s$]
w_i	Production rate of premixed combustion [$kg/m^3/s$]
Y_i	Mass fraction [kg/kg]

Greeks

Δ	Grid scale [m]
Σ	Fractal parameter[1/m]
$\delta_L{}^0$	Flame thickness [m]
Ξ	Increasing rate of flame surface area [-]
η	Kolmogorov scale [m]
μ	Viscosity [Pa·s]
ρ	Density [kg/m^3]

Subscripts

b	Burned
sgs	Subgrid scale
ul	Unburned

Chapter 5: Conclusions

5.1 Summary and conclusions

The purpose of this study was to construct numerical simulation methods that can predict the performance of combustors and carbon monoxide (CO) emissions. Hence, three elementary combustion fields with cooled walls or cooling air were investigated. The first case was the one- and two-dimensional (1D and 2D) CH_4-air premixed combustion fields with flame propagation close to the cooled walls, which were solved by direct numerical simulation (DNS) with a detailed reaction mechanism approach or a non-adiabatic flamelet generated manifolds (NA-FGM) approach (Chapter 2). The second case involved the CH_4–air super lean premixed combustion fields generated by an axisymmetric jet burner with cooled walls under pressurized conditions, which was solved by using a large eddy simulation (LES) employing an NA-FGM approach, accounting for the effects of heat loss (Chapter 3). The third case involved the combustion fields where non-premixed and premixed combustion fields coexist in an actual combustor with a coaxial jet cluster burner, which was solved by using an LES employing the hybrid turbulent combustion (HTC) approach combining the flamelet progress variable (FPV) approach, flame propagation approach, and CO transport approach. This burner generated combustion fields between premixed and non-premixed by controlling the mixing process (Chapter 4).

In Chapter 2, the CH_4–air premixed combustion fields near a cooled wall were discussed. In this chapter, the purpose was to perform 1D numerical simulations by employing a detailed reaction mechanism approach, and 2D numerical simulations by employing a detailed reaction mechanism approach or NA-FGM approach, and to investigate the effects of the equivalence ratio, pressure, and wall temperature on CO emissions in detail. It was revealed by 1D numerical simulations that the CO consumption rate in the vicinity of the cooled wall was reduced and consequently posed a risk of increasing the CO emissions at the combustor exit for lower equivalence ratio, higher pressure, or lower wall temperature. Moreover, the CO consumption rate was most susceptible to the wall temperature. Additionally, similar tendencies were observed in 2D

numerical simulations considering turbulent eddies. These calculation results suggested that the control of heat loss through the wall could be an important key to the effective consumption of CO emissions from combustors. Furthermore, it was revealed that the NA-FGM approach can reproduce the results of the detailed reaction mechanism approach for flame characteristics at different wall temperatures. This is because the NA-FGM approach takes account of the heat loss near the cooled wall. In conclusion, these results suggested that the NA-FGM approach is effective for predicting CO emissions for turbulent lean premixed combustion in combustors.

In Chapter 3, the CH_4–air super lean premixed combustion fields generated by an axisymmetric jet burner with cooled walls under pressurized conditions were discussed. In this chapter, the purpose was to predict the CO emissions by applying the NA-FGM approach, which can account for the effects of heat loss. It was found that the NA-FGM approach improved the prediction accuracies of not only the flame behavior but also the CO emissions compared to the conventional FGM approach, which inherently neglects the heat loss effect. The NA-FGM approach captured the trends of CO emissions properly during the experiments, in which the CO emissions increased with a decreasing equivalence ratio. This success could be achieved by considering the effects of heat loss in chemical reactions involving CO and OH radicals It was also suggested that the cause of the increase in CO emissions for low equivalence ratios was not because of the increase in CO production, but owing to the slow CO consumption rate, which kept the CO concentration high downstream. In conclusion, these results suggested that capturing such a sensitive reduction in CO consumption rate by heat loss is important for accurately predicting the CO emissions in developing a low-emission gas turbine combustor at low loads.

In Chapter 4, the complicated combustion fields (coexistence of the non-premixed and premixed flames) generated by a coaxial jet cluster burner for actual gas turbine combustors was discussed. This burner can change the combustion form between premixed and non-premixed combustion by controlling the mixing process. Therefore, the HTC approach was developed to calculate the form in which a non-premixed flame coexists with a premixed flame was developed. The HTC approach consists of the FPV approach, flame propagation approach, which includes a flame stretch effect, diffusion

enhancement effect, and the increasing rate of the flame surface area; and a CO transport approach using a transport equation with a flamelet library. In this chapter, the purpose was to understand the phenomena that occurs in the combustion fields and to clarify the CO formation mechanism in order to develop gas turbine combustors. In this study, the HTC approach was validated by comparing the results of the HTC approach with the measured gas temperature and gas concentration distributions obtained from a coaxial jet cluster burner test rig under atmospheric pressure. Thus, it was clarified that the formation factor of CO was the oxidation reaction of fuel in the upstream of the combustion chamber and the quenching of the CO oxidation reaction by the temperature reduction caused by the effect of cooling air in the downstream of the combustion chamber.

Therefore, it was found that the formation and consumption rate of CO were strongly affected by heat loss, and the increase in CO emissions in the partial loads of the gas turbine combustor was caused by the decrease in the CO consumption rate. Since various factors reduce the CO consumption rate, it was found to be a "slow chemistry" compared to the main reaction product. The calculation method used in this study reproduced a “slow chemistry" by considering the effects of heat loss on the chemical reaction.

5.2 Suggestions for future research

We will conduct the research in the following themes to expand the progress of this study.

(1) As described in Chapter 4, it is assumed that a complicated combustion configuration is formed in an actual gas turbine combustor. In Chapters 2 and 3, we evaluated the validity of the NA-FGM approach for premixed combustion for taking into account the effect of heat loss in CO emissions. In the future, the optimal combination of turbulent combustion models, i.e., non-premixed combustion and premixed combustion approaches will be important for numerical simulations of combustion fields in actual gas turbine combustors. In Chapter 4, we tried this approach, but the effect of heat loss was not considered, and the delay in the CO reaction rate was simulated by introducing a transport equation. However, as described in Chapter 2,

because the effect of heat loss from the cooled walls and cooling air near the wall on the reaction cannot be ignored, a combination of the NA-FPV and NA-FGM approaches, which are the models for non-premixed and premixed combustion, respectively, is desirable. Switching parameters are also important for combining turbulent combustion models. When the turbulent combustion model is switched incorrectly, there is an uncertainty in the prediction accuracy of both emissions and the flame position. In Chapter 4, we used an equation based on the difference in the gradient between the mixture fraction and the progress variable as a switching parameter. Alternatively, the Flame Index, which uses the difference in the concentration gradient between fuel and oxidant, could be used. In any case, to predict the performance of an actual gas turbine combustor with low calculation cost and high accuracy, it is necessary to develop a new method of combining turbulent combustion models.

(2) From the viewpoint of CO_2 reduction, the conversion of hydrocarbon fuels to carbon-neutral fuels such as hydrogen (H_2) and ammonia (NH_3) will be promoted. Fuel flexibility is important in numerical combustion simulation technologies. As hydrogen is more combustible than liquified natural gas (LNG), the risk of "flashback" which is a transient upstream propagation of a flame, must be assessed. First, it is necessary to accurately reproduce the flame position in order to predict the flashback. Here, a phenomenon peculiar to hydrogen is the “preferential diffusion effect”. The turbulent combustion approach can be expanded to the hydrogen fuel correspondence by introducing this effect into the NA-FGM approach examined in this study. On the other hand, for the ammonia, the risk of extinction must be assessed because it is less combustible than LNG. In gas turbine combustors, swirlers are often used to improve flame stability. It is considered that the flame stretch effect, which is caused by the velocity gradient generated by the swirl component, reduces the flame propagation speed. Therefore, by considering the “flame stretch effect”, the turbulent combustion approach can be expanded to the ammonia fuel correspondence. Thus, in addition to the effects of the heat loss studied in this study, the “preferential diffusion effect” and the “flame stretch effect” can be taken into account to cope with various

fuels and contribute to the design of gas turbine combustors.